Dynamics of an air bubble rising in constant and varying viscosity media

A Thesis Submitted to
Indian Institute of Technology Hyderabad
In Partial Fulfillment of the Requirements for
The Degree of

Doctor of Philosophy

by

Premlata Amarnath Ram
Reg. No. CH13M15P000003

भारतीय प्रौद्योगिकी संस्थान हैदराबाद
Indian Institute of Technology Hyderabad

Department of Chemical Engineering
Indian Institute of Technology Hyderabad
Sangareddy, Hyderabad – 502 285
July 2017

DECLARATION

I hereby declare that this written submission represents my ideas in my own words, and where ideas or words of others have been included, I have adequately cited and referenced the original sources. I also declare that I have adhered to all principles of academic honesty and integrity and have not misrepresented or fabricated or falsified any idea/data/fact/source in my submission. I understand that any violation of the above will be a cause for disciplinary action by the Institute and can also evoke penal action from the sources that have thus not been properly cited, or from whom proper permission has not been taken when needed.

Premlata Amarnath Ram
Roll No: CH13M1009

Approval Sheet

This thesis entitled "Dynamics of an air bubble rising in constant and varying viscosity media" by Premlata Amarnath Ram (Reg. No. CH13M15P000003) is approved for the degree of Doctor of Philosophy from IIT Hyderabad.

Prof. R. P. Chhabra (IIT Kanpur)
Examiner 1

Amit Agrawal
Prof. Amit Agrawal (IIT Bombay)
Examiner 2

Prof. Narasimha M.
Internal Examiner

Prof. Kirti Chandra Sahu
Adviser/Guide

K. Badarinath
Prof. Karri Badarinath
Co-Adviser

Prof. Raja Banerjee
Chairman

Acknowledgements

Firstly, I would like to express my sincere gratitude to my advisor Prof. Kirti Chandra Sahu and co-supervisor Prof. Karri Badarinath for their continuous support for my PhD study and related research. Their guidance helped me a lot in all the time of research and writing of this thesis.

I am grateful to my Parents and Siblings, who have provided me moral and emotional support in my life. I am also grateful to my other family members and friends who have supported me along the way.

I thank my fellow lab-mates Mounika, Sweta, Vivek, Prakash, Vamshidhar, Kannan and research co-workers Dilin, Meenu, Veera Prasad and Ashish for their help and support and for all the fun we had during my PhD.

Special Thanks to Susree Di, and Sumohana Sir, for helping me in my research work. I am thankful to our Director and IIT Hyderabad for providing me infrastructure and lab facility. Finally I am thankful to MHRD for the financial support throughout my PhD.

Synopsis

The dynamics of a gas bubble rising in a liquid is observed in many natural phenomena, and also in industrial applications. Due to its practical relevance, this has been studied from many centuries and it continues to be a problem of great interest even today. The main objectives of the thesis are to investigate some novel problems on bubble rising in viscosity varying systems. In several situations one could observed viscosity stratified media. Two of them are considered in this work. (a) When viscosity stratification is inherently present in the surrounding medium (say, viscosity of the outer fluid is increasing linearly with height). (b) When the outer fluid is a non-Newtonian fluid, wherein the surrounding fluid viscosity varies due to the shear caused by the motion of the bubble. Three-dimensional numerical simulations and experiments are performed to study these flows. The flow dynamics is governed by mass, momentum and energy conservation equations. A volume-of-fluid (VoF) approach is used to track the interface separating the fluids. The computational and experimental approaches used in this study are discussed in Chapter 2. The validations of the present numerical solver are also performed in the same chapter. In order to compare the bubble behaviour in a medium with varying viscosity with that observed in a constant viscosity medium (standard system), the dynamics of a rising bubble in a standard air-water system is also investigated.

First a standard system (air-water system) is considered. The dynamics of an air bubble rising in a Newtonian quiescent liquid is experimentally investigated in Chapter 3. A phase plot in the Galilei and Eötvös numbers plane, which separates distinct regimes in terms of bubble behaviour is generated. This is similar to the one numerically obtained by Tripathi *et al.* (2015*a*). Direct numerical simulations are also conducted and the behaviour of the bubble in these regimes is studied. The similarities and differences between the experimental and numerical results are discussed. The present work reveals that apart from Reynolds and Eötvös numbers, which were thought to be the only important governing parameters for rising bubbles in air-liquid systems, our results show that the actual density and viscosity ratios are also required to describe the bubble dynamics, especially in the parameter space close to the region boundaries in the phase-plot. To the best of our knowledge, none of the previous studies have shown an experimentally obtained phase plot for such a large range of Galilei and Eötvös numbers.

In chapter 4, the above study is extended to considered the interaction of two bubbles while rising side-by-side in a Newtonian fluid. Two spherical objects rising through a heavier fluid in the Stokes flow regime would maintain their spacing. In particular, if the two objects are initially in the same horizontal plane, they would rise in straight vertical paths and the line separating them would be horizontal and of constant length. In this chapter, we ask a fundamental question, i.e. how two identical inertial bubbles rising under gravity would respond to each other. Three-dimensional numerical simulations are conducted to study this problem. This study reveals the destabilizing nature of the interaction between the wakes of the bubbles, which causes them to rise in an oscillatory path. Such three dimensionality sets in earlier in time than for a single bubble and also at a lower inertia. The interaction leads to a mirror symmetry in the trajectories of the two bubbles, which persists for some time even in the high inertia regime where each path is chaotic. The effect of the inertia and initial separation on the mirror symmetry of the path, the vortex shedding pattern and the attraction/repulsion between the bubbles are examined. The bubble rise has been interestingly observed to be symmetrical about the plane perpendicular to the separation vector for all separation distances considered in the present study.

Next in Chapter 5, the rise dynamics of an air bubble in viscosity varying media is considered. As discussed in Chapter 1, in spite of the large volume of work carried out on bubbles and drops, very few studies have examined the influence of viscosity stratification on bubble rise dynamics. In Section 5.1, first an inherently viscosity-stratified surrounding fluid is considered. By conducting time-dependent axisymmetric simulations, a library of bubble shapes in the Galilei and the Eötvös numbers plane is presented, which demonstrates some counter-intuitive phenomena for certain range of parameters due to the presence of viscosity stratification in the surrounding fluid. It is found that in a linearly increasing viscosity medium, for certain values of parameters, bubble undergoes large deformation by forming an elongated skirt, while the skirt tends to physically separate the wake region from the rest of the surrounding fluid. This peculiar dynamics is attributed to the migration of less viscous fluid that is carried in the wake of the bubble as it rises, and thereby creating an increasingly larger viscosity contrast between the fluid occupied in the wake region and the surrounding fluid, unlike that observed in a constant viscosity medium. We also found that for lower values of Eo and Ga, although the bubble moves slowly in case of the linearly increasing viscosity medium, the shapes look very similar to those observed in a constant viscosity medium. In future, it will be interesting to investigate this phenomenon in three-dimensions and by conducting experiments.

Then the dynamics of an air bubble inside a shear thinning/thickening fluid is studied in both axisymmetric and three-dimensional regimes. The non-Newtonian fluid is modelled using the Carreau-Yasuda model (Zhang *et al.*, 2010). In the axisymmetric regime (see Section 5.2), we focus on a bubble in the low Ga and low Eo region. A parametric study is conducted by varying the shear-thinning/thickening tendency of the surrounding fluid for different Galilei and Eötvös numbers. As compared to a Newtonian fluid, it is found that increasing the shear thinning tendency increases the rise velocity, and reduces the deformations of the bubble. The deformation of the bubble is enhanced for higher Ga and low Eo. This work also reveals the importance of studying the rising bubble in the other regimes, i.e high Ga and moderate to high Eo, where the dynamics could be three-dimensional. This constitute the subject of discussion in the next section.

The dynamics of a rising bubble in a Carreau-Yasuda shear-thinning fluid is studied in Section 5.3 via three-dimensional simulations and experiments using CMC (carboxymethyl cellulose) solutions. For the parameter values considered, an air bubble exhibits three-dimensional behaviour, i.e. path instabilities (zigzagging/spiralling motion) and topological changes while rising in shear-thinning fluids (CMC solutions). For the same set of parameters, a bubble maintains azimuthal symmetry and rises in a straight path while rising in a Newtonian surrounding fluid. The mechanism of this three-dimensional behaviour is investigated by plotting the vorticity and viscosity contours. For $Ga = 30$ and $Eo = 1$ (first set), it is observed that at early times the air bubble rises in a straight path and later undergoes a spiralling path. Asymmetrical shape deformation and vortex shedding are observed during the wobbling (zigzagging/spiralling) motion. The mechanism of this three-dimensional behaviour is investigated by inspecting the vertical vorticity component and viscosity. It is found that vortex shedding in the wake region, asymmetrical shape deformation and path instability are interconnected. For $Ga = 30$ and $Eo = 25$ (second set), an air bubble rising in a shear-thinning fluid undergoes peripheral break-up. In contrast, the bubble forms skirt while rising in a Newtonian fluid. We verify that the three-dimensional behaviours observed in this study are the consequence of shear-thinning nature of the surrounding medium, and not just due to the reduction of viscosity of the Newtonian fluid. The effects of the variation of flow index (n) and inelastic time constant (λ) are also investigated. It is found that increasing the shear-thinning tendency (decreasing the value of n) and increasing λ promote the three-dimensional behaviour. In our experiments, the shapes of an air bubble rising in deionised water and CMC solutions are recorded using a high-speed camera. The shapes and trajectories of the bubbles obtained from the experiments are qualitatively in good agreement with those obtained from the numerical simulations.

The present study arises further questions and new areas to be investigated in future. This includes

- What happens in case of drops falling in an gaseous medium or in another liquid media?
- What happens when we change the initial condition by changing the initial shape of bubbles/drops from spherical to complex shapes, such as oblate, prolate and even more complex shapes which are observed in experiments?
- How the presence of temperature gradient (Marangoni convection) influences the dynamics of bubbles?
- What happens when the bubble rises in fluids with other rheologies, such as viscoelastic, viscopleastic, thixotropic nature?

A blob of fluid of density ρ_i moving in a surrounding medium of density ρ_o is called a bubble if $\rho_r(\equiv \rho_i/\rho_o) < 1$ or a drop if $\rho_r > 1$. In gas-liquid systems, bubbles in general behave differently from drops and the mechanism behind the differences were investigated by Tripathi *et al.* (2014). It is well known that as a result of path instability, an initially spherical air bubble rising in a liquid ($\rho_r << 1$) can either zigzag or spiral for high inertia and high surface tension (Cano-Lozano *et al.*, 2016*a*; Saffman, 1956; Tripathi *et al.*, 2015*a*). It undergoes an unsteady shape deformation resulting in vortex shedding behind the bubble during this wobbling motion. In contrast, a solid sphere or an initially spherical liquid drop in air ($\rho_r >> 1$) falls in a straight path (Vries, 2001). For a falling leaf or flat/cylindrical solid objects (i.e. non-spherical) in gas/liquid, oscillatory motion is observed due to the associated aerodynamics/hydrodynamics. A question that arises then is, can we observe path and/or shape instabilities by making the initial drop shape nonspherical in an air-liquid system. It would be interesting to study if a similar phenomenon occurs for a nonspherical liquid drop falling in air.

In liquid-liquid systems (with $\rho_r \leq 2.2$), by releasing spherical drops of organic liquids, Edge & Grant (1971) experimentally found that a small liquid drop falls in a straight path, but a bigger drop falls in a zig-zag path (i.e., wobbling motion) in water under the action of gravity. They observed a thread-like wake for small drops, but vortex sheet for large drops falling in zigzag paths. They also observed shape oscillations (oblate-prolate deformation) in case of zigzagging drops. Later, considering liquid-liquid systems (for $\rho_r \approx 1$), Koh & Leal (1989, 1990) investigated the dynamics of an initially nonspherical bubble rising in a quiescent liquid of slightly higher density by conducting numerical simulations and experiments at low Reynolds numbers ($Re < 0.01$). They found that a bubble with a small degree of nonsphericity, comes back to a spherical shape, whereas for a bubble with a large degree of nonsphericity, the deformation continues to increase with time.

Another PhD student Meenu Agrawal is extending the present work to investigate the effect of nonspherical shape liquid droplets falling in air or another lighter liquid. She is also planning to conduct Particle Image Velocimetry (PIV) to understand the flow dynamics experimentally. I have recently collaborated with Meenu Agrawal in one of her PhD work. We have attempted to answer the following questions: (i) Can one observe oscillatory motion in case of a falling liquid drop in air ($\rho_r >> 1$) by changing its initial shape to a nonspherical one? (ii) For situation (i), where inertia becomes important, what effect does it have on the droplet dynamics? (iii) The presence of inertia may result in vortex shedding. What is the role of vortex shedding in this case and how different is it from that observed in case of a rising bubble? To answer these questions, three-dimensional numerical simulations are conducted to investigate the hydrodynamics of an initially nonspherical liquid droplet falling in air ($\rho_r \approx 1000$), and the effects of initial deformation (degree of obliquity) and inertia are investigated. See our article Agrawal *et al.*, PRE, 2017 for more detail.

The knowledge of the present study is also very useful in investigating raindrops. However, one has to incorporate other complex phenomena, such as phase change, coalescence and break-up. These phenomena affect the shape and size distributions of raindrops, which in turn influence the modelling of rainfall. As these phenomena depend on local conditions, in order to make an accurate prediction, one has to study raindrops and associated dynamics for a given atmospheric condition.

In all the situations discussed above, the presence of temperature provides another dimension to the study. Marangoni stresses due to the variation in surface tension by virtue of the presence of temperature and concentration gradients at the interface separating two immiscible fluids play a vital role in many technological applications. A characteristic problem of this nature is the thermocapillary migration of drops and bubbles. The current work can be extended to include the Marangoni convection due to temperature/surfactant gradients.

Another PhD student in our group, Mounika Balla is working on these aspects.

A variety of situations can also be considered by varying the rheological properties of the surrounding medium. In the present thesis, only a shear-thinning fluid is considered. It will be interesting to investigate the dynamics of an air bubble rising in other class of non-Newtonian fluids, such as viscoplastic, viscoelastic and thixotropic fluids.

Refereed Publications

Journal Papers

1. "Shapes and paths of an air bubble rising in quiescent liquids", D. M. Sharaf, A. R. Premlata, M. K. Tripathi, Badarinath Karri and K. C. Sahu, *Physics of Fluids* (in press).
2. "Two initially spherical bubbles rising in quiescent liquid", M. K. Tripathi, A. R. Premlata, K. C. Sahu and R. Govindarajan, *Physical Review Fluids*, **2**, 2017, 073601.
3. "Numerical and experimental investigations of an air bubble rising in a Carreau-Yasuda shear-thinning liquid", A. R. Premlata, M. K. Tripathi, B. Karri and K. C. Sahu, *Physics of Fluids*, **29**, 2017, 033103.
4. "Nonspherical liquid droplet falling in air", M. Agrawal, A. R. Premlata, M. K. Tripathi, B. Karri and K. C. Sahu, *Physical Review E.*, **95**, 2017, 033111.
5. "Dynamics of an air bubble rising in a non-Newtonian liquid in the axisymmetric regime", A. R. Premlata, M. K. Tripathi, B. Karri and K. C. Sahu, *Journal Non-Newtonian Fluid Mechanics*, **239**, 2017, 53-61.
6. "Dynamics of rising bubble inside a viscosity-stratified medium", A. R. Premlata, M. K. Tripathi and K. C. Sahu, *Physics of Fluids*, **27**, 2015, 072105.

Conference Papers

1. "Shapes and paths of an air bubble rising in quiescent liquids", A. R. Premlata, Dilin Sharaf, Manoj Tripathi, Karri Badarinath and K. C. Sahu, 70^{th} *Annual Meeting, American Physical Society Division of Fluid Dynamics*, November 19-21, 2017, Denver, Colorado.
2. "Dynamics of an air bubble rising in a shear-thinning liquid", A. R. Premlata, M. K. Tripathi, B. Karri and K. C. Sahu, *Proceedings of the* 24^{th} *National and 2nd International ISHMT-ASTFE Heat and Mass Transfer Conference (IHMTC-2017)*, December 27-30, 2017, BITS-Pilani, Hyderabad, India.

List of Figures

List of Tables

Contents

CHAPTER 1

Introduction

Multiphase flows are the flows involving several phases simultaneously. The study of multiphase flows is not only relevant in many natural and industrial applications, but also fundamentally very interesting. A few examples of multiphase flow applications are generation of water waves by wind, pipeline lubrication, air-water flow in nuclear reactor, primary atomization of jets, extrusion, etc. The study of multiphase flows is a vast topic and can be broadly classified into two categories: (i) miscible (ii) immiscible flows. In miscible flows, diffusion plays a vital role, whereas, in immiscible flows, surface tension dominates the flow dynamics. In case of miscible flows, the fluids are separated by a mixed layer of finite thickness. In this case, if the diffusion time scale is very large as compared to the flow time scale, the thickness of the mixed layer will grow very slowly making the fluids distinguishable for a long time. On the other hand, in immiscible flows, the fluids are separated by a sharp interface forever. Due to the diversity a general description of these flows is almost impossible, making the fundamental research necessary. The dynamics of a gas bubble rising in a surrounding liquid medium comes under the class of immiscible flows, which is the subject of the present thesis.

In order to understand the present subject, it is important to distinguish a bubble from a drop. These definitions will be used through out the thesis. If a blob of fluid is lighter than the surrounding fluid, we call it a bubble and if it is heavier than the surrounding fluid, it is called as drop. In other words, for a bubble, the density ratio, ρ_r ($\equiv \rho_i/\rho_o$) < 1, and for a drop, $\rho_r > 1$. Here, ρ_o and ρ_i are the density of the outer or surrounding fluid (i.e. continuous phase) and inner fluid (i.e. dispersed phase), respectively. Thus, based on our definition, a bubble rises up under the action of buoyancy, while a drop falls down under the action of gravity (g). The motion of a bubble or drop is commonly influenced by gravitational, surface tension, and viscous forces. Excluding the surface tension force, which acts at the interface separating the fluids (dispersed and continuous phases), the various forces acting on a rising bubble and a falling drop are shown in Fig. 1.1. Since the drop falls under the action of gravity, the drag force F_d acts in the upward direction, whereas, the bubble rises due to the buoyancy force and thus the drag acts in the downward direction. For both bubbles and drops, weight W acts in the downward direction and buoyancy force F_b acts in the upward direction. As the forces acting on bubbles and drops are the same, one can expect that a drop will behave like a bubble if we invert the gravity in one case. However in general, they do not. The mechanism because of which a bubble behaves differently than a drop is explained by Tripathi *et al.* (2014). It should also be noted here that the motion of a drop in a surrounding fluid ($\rho_r > 1$) is different from that of a solid particle ($\rho_r \gg 1$) in the same surrounding fluid. An important property of bubbles/drops is the internal circulation, which enhances mixing, and heat and mass transfer. The internal circulation inside bubbles/drops is responsible for the reduction of drag which causes them to move faster than solids. Furthermore, this circulation affects the flow field in the wake which differentiates a fluid bubble/drop from a solid.

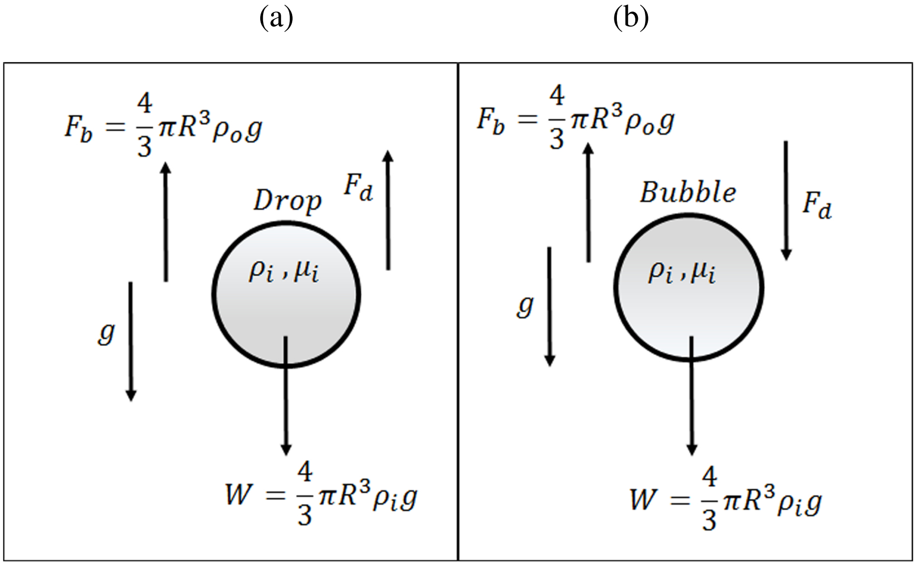

Figure 1.1: Forces acting on (a) a falling drop, and (b) a rising bubble. Here F_b is the buoyancy force, F_d is drag force, g acceleration due to gravity, W is weight. ρ_i, μ_i and ρ_o, μ_o are the density and viscosity of dispersed phase (inner fluid) and continuous phase (outer fluid), respectively.

We now focus on the specific type of flow involving the motion of a rising bubble in a surrounding fluid. The dynamics of gas bubble rising in a liquid is observed in many natural phenomena, such as aerosol transfer from sea, carbon sequestration (Gal-Or *et al.*, 1969), etc., and also in industrial applications, such as bubble column reactors, cavitation, food processing, oil extraction, to name a few. Due to its practical relevance, the dynamics of bubbles has been studied from many centuries and it continues to be a problem of great interest even now. The first documented study of a rising bubble goes back to Leonardo Da Vinci in the 1500s (Prosperetti, 2004). Most of the fundamental understanding of such flows; however, started in the early 1900s and focused on terminal velocity and flow field inside tiny bubbles. An empirical formula for the terminal velocity of a small sphere in a viscous liquid was derived by Allen (1900). Later, Hadamard (1911) and Rybzynski (1911) independently came up with the solution of terminal velocity and flow field inside and outside of a slowly rising spherical bubble (in the creeping flow regime) in another fluid of different viscosity and density. Several corrections were made to this analytical solution in order to include inertia and small deformation from the spherical shape (Leal, 1992). In the last few decades, due to the development of powerful super computers and advanced experimental techniques, researchers have been able to study big bubbles and large deformations. The asymmetrical shape deformation in bubbles, which leads to zig-zagging/spiralling motion (commonly known as path instability), was also investigated by several researchers (see e.g. Bhaga & Weber (1981); Duineveld (1995)). In spite of being an active area of research for several decades, there are many unsolved problems, a few of which have been explored in the present thesis.

In the dimensionless formulation, the dynamics of a rising bubble can be described using four dimensionless numbers: Galilei number ($Ga \equiv \rho_o g^{1/2} R^{3/2}/\mu_o$): which is the ratio of the gravitational force to the viscous force, Eötvös number ($Eo \equiv \rho_o g R^2/\sigma$): it measures the importance of the surface tension forces as compared to the body forces, density ratio $\rho_r (\equiv \rho_i/\rho_o)$ and viscosity ratios $\mu_r (\equiv \mu_i/\mu_o)$. Here, R is the equivalent radius of the bubble, σ is the interracial tension, while μ_o and μ_i are the viscosity of the surrounding (continuous phase) and inner (dispersed phase) fluids, respectively. An additional dimensionless parameter, Morton number (Mo) can also be defined as $Eo^3/Ga^4 (\equiv g{\mu_o}^4/\rho_o\sigma)$, which is unique for a particular set of fluids as it depends on fluid properties alone. A rising bubble may never attain a terminal velocity, and even if does, the terminal velocity is unknown beforehand, therefore Galilei and Eötvös number are very useful to describe the dynamics of rising bubble rather than Reynolds number ($\equiv \rho_o R U/\mu_o$) and Weber number ($\equiv \rho_o R U^2/\sigma$) which contain the terminal velocity, U.

1.1 Literature review

The main focus of this thesis is on the change in the dynamics of an air bubble while rising in liquid media with varying viscosity. Three-dimensional numerical simulations and experiments are performed to study these flows. Two different approaches have been adopted to achieve the viscosity variation: (a) viscosity stratification by considering a fluid whose viscosity increases linearly with height, and (b) considering shear-thinning fluid in which viscosity of fluid varies due to the shear caused by the motion of the bubble. In order to compare the bubble behaviour in a medium with varying viscosity with that observed in a constant viscosity medium (standard system), the dynamics of a rising bubble in a standard air-water system is also investigated experimentally. In the following paragraphs, a review of the previous studies in the literature related to behaviour of a bubble in constant viscosity as well as varying viscosity media is presented to better appreciate the scope and contributions of the present thesis.

1.1.1 An air bubble rising in a Newtonian fluid

The hydrodynamics of single bubble in quiescent liquid have been studied by previous researchers both computationally (see e.g. Baltussen *et al.* (2014); Dijkhuizen *et al.* (2010); Sussman & Puckett (2000)) and experimentally (see e.g. Bhaga & Weber (1981); Clift *et al.* (1978); Haberman & Morton (1953)). The experimental investigation on this subject provides a library of bubble shapes, including skirted, spherical cap, and oscillatory and non-oscillatory oblate ellipsoidal. Recently, Tripathi *et al.* (2015*a*) (see Fig.1.2) conducted three-dimensional numerical simulations by varying Ga and Eo numbers for an air bubble rising in a liquid for $\rho_r = 10^{-3}$ and $\mu_r = 10^{-2}$. They identified five different regions of distinct bubble behaviours (namely, axisymmetric, skirted, zigzagging/spiralling, peripheral break-up and central breakup). They showed that an air bubble maintains its azimuthal symmetry (region I) for low Ga - low Eo, and is either spherical, oblate or dimpled. For low Ga, and high Eo (region II), skirted bubbles are observed, whereas for high Ga, and low Eo (region III), a bubble follows a spiral or zigzag path (wobbling motion). An air bubble with high Ga and high Eo breaks to form satellite bubbles (region IV) or undergoes topological changes to form a toroidal shape (region V).

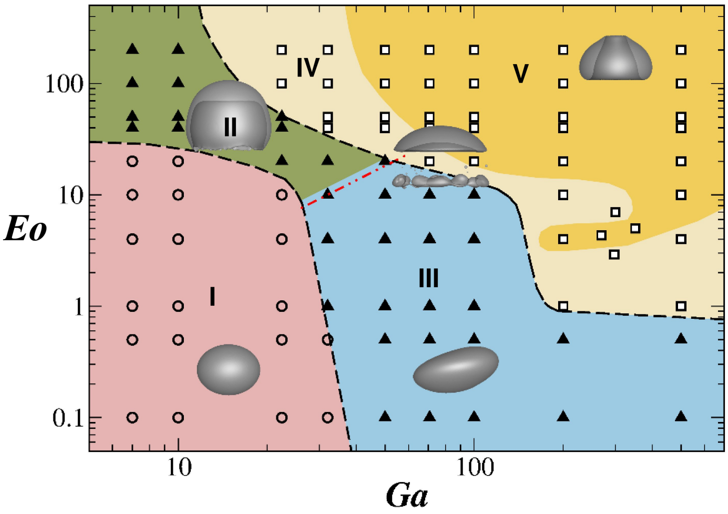

Figure 1.2: Different regimes of bubble shape and behaviour. (Taken from Tripathi *et al.* (2015*a*)).

In this context, it is important to discuss the classical region map provided by Bhaga & Weber (1981) (see Fig.1.3; also see Clift *et al.* (1978)) which has been used by several researchers in the past. Bhaga & Weber (1981) and Clift *et al.* (1978) conducted experiments on an air bubble rising in aqueous sugar solutions of differing concentrations. They identified regimes of spherical, oblate, wobbling and skirted bubbles in the Reynolds and Eötvös numbers plane based on the bubble shapes and motion. A few points regarding this classical regime map are note worthy. The use of Reynolds and Eötvös numbers for the phase plot may provide a multivalued nature to the phase-plot. For example Landel *et al.* (2008) showed that for the same volume of air (i.e constant Galilei and Eötvös numbers) spherical cap bubbles with a range of rise velocities (multiple Reynolds numbers) and volume of satellite bubbles can be produced. Therefore, another consequence of this multivalued behaviour can be observed in the fact that Clift *et al.* (1978) provided only approximate boundaries for unbroken bubbles (i.e, for regions I, II and III).

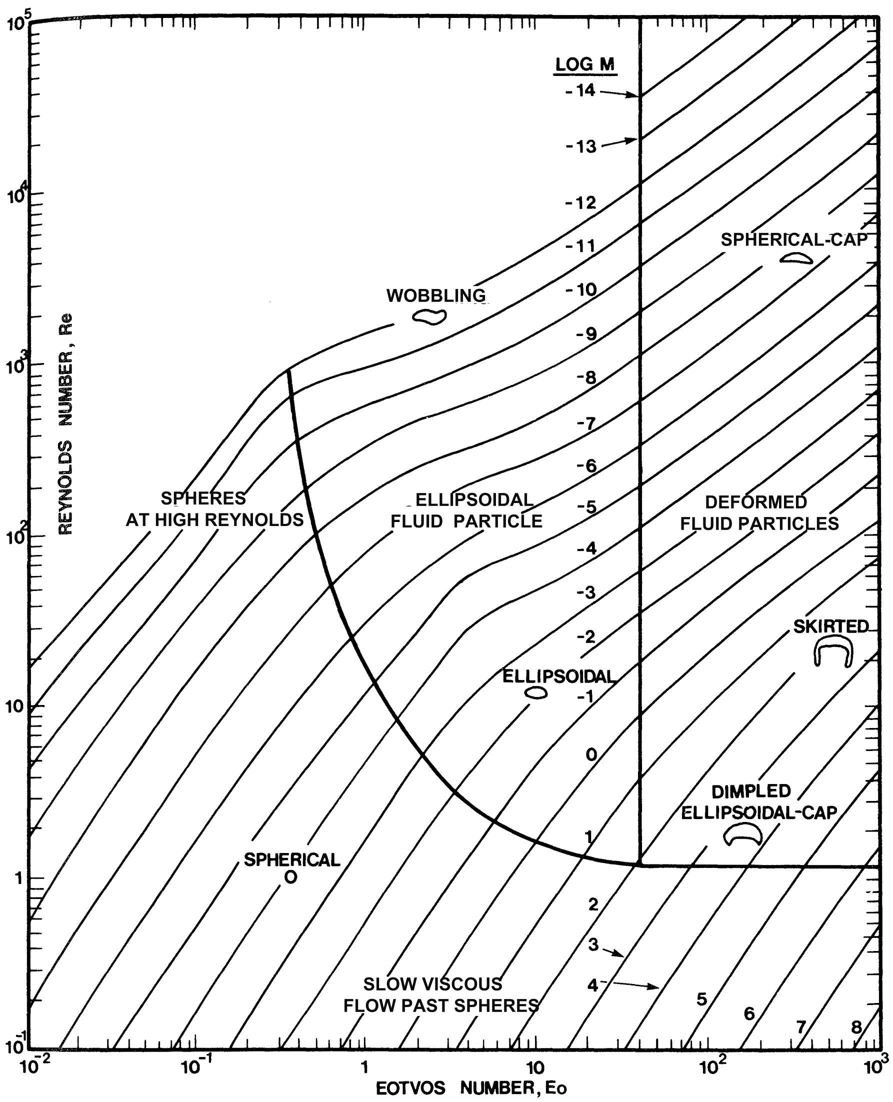

Figure 1.3: Shape regimes for bubbles and drops in unhindered gravitational motion through liquids. (Taken from Clift *et al.* (1978)).

Computational researchers (e.g. Hua *et al.* (2008); Ohta *et al.* (2005*a*); Tsamopoulos *et al.* (2008*a*)), who used the previous experimental results (Bhaga & Weber (1981); Clift *et al.* (1978)) to validate their numerical solvers assumed the bubble behaviour presented by them to be true for all bubbles regardless of the density and viscosity ratios. The usage of the Reynolds and/or Weber numbers in previous studies (e.g. Ohta & Sussman (2012); Tsamopoulos *et al.* (2008*a*)) poses an additional limitation for unsteady bubbles because these parameters depend on the terminal velocity, which is not easy to determine accurately in experiments and is also not known *a priori* to be used in numerical simulations. Other experimental and numerical studies (e.g. Bonometti & Magnaudet (2007); Dijkhuizen *et al.* (2010); Ohta *et al.* (2014); Ohta & Sussman (2012); Tomiyama *et al.* (2002)) focused on individual regimes of bubble behaviour by considering limited sets of parameters.

The literature above shows the limitation of using Reynolds number, as it contains the terminal velocity term, which is not known *a priori*. The Galilei number on the other hand uses $(gR)^{1/2}$ as a velocity scale instead of the terminal velocity. The Galilei number thus can be easily calculated from the radius of the bubble which can be obtained from the initial volume of the bubble. In the first part of this thesis, an extensive experimental study of the standard system (that is a constant viscosity Newtonian fluid) is conducted to generate the phase plot (similar to the one generated numerically by Tripathi *et al.* (2015*a*)) in the Galilei and Eötvös numbers plane experimentally. Close to three hundred air bubbles rising in aqueous glycerol solutions of different concentrations are investigated. A phase plot in *Ga*-*Eo* plane is presented over a much larger range of Galilei and Eötvös numbers than those available in the literature. The plot shows the distinct regimes based on shape and path of a rising bubble. The behaviour of an air bubble in these regimes is investigated and compared with the corresponding numerical simulations. Our results also provide a comprehensive database on bubble behaviour for the standard system.

1.1.2 Two initially spherical bubbles rising side-by-side

Section 1.1.1 deals with the study of single bubble rising in Newtonian fluid (standard system). An extension of this problem is to study the dynamics of two bubbles rising side by side in a Newtonian fluid, which has been carried out numerically in the second part of the thesis. To put our work in context, the literature related to two bubbles is reviewed next.

The dynamics of multiple bubbles have also been a subject of research from a long time. Many researchers, e.g. Bonometti *et al.* (2007); Bunner & Tryggvason (1999) investigated the interactions between flow and many bubbles in the context of bubble-column reactors, bioreactors, etc. The hydrodynamics of two bubbles rising side-by-side not only get affected by direct interactions of the bubbles (which may result in coalescence for some parameter values), but also the interactions between the wakes or boundary layer developed around these bubbles, which can influence the shape deformations and paths of these bubbles.

The interactions and trajectories of a pair of bubbles have been investigated analytically by Leal (1992) in the Stokes flow and by Kok (1993*a*); Legendre *et al.* (2003) in the potential flow regimes. The trajectories of bubbles have been predicted well in the potential flow limit by the solution proposed by Kok (1993*a*,*b*). He has also experimentally shown that the two bubbles rising vertically in ultrapure water tend to rotate to align horizontally. By conducting two-dimensional simulations, Chen *et al.* (2011) found that two bubbles rising side-by-side coalesce, and the resultant single bubble shows shape oscillations, which agrees with those observed in the experiment of Duineveld (1998). Duineveld (1998) experimentally found that the zigzagging pair of bubbles have a higher amplitude of oscillation than a corresponding isolated bubble. He also noted that the potential theory fails to predict such motion because of the boundary layer interactions in the experiments. This has also been supported by the experiments and numerical simulations of Sanada *et al.* (2009) and Legendre *et al.* (2003), respectively. Sanada *et al.* (2009) also experimentally investigated the bouncing and coalescence of a pair of bubbles rising side by side in an initially quiescent liquid. They found that for higher Reynolds numbers and low Weber numbers the bubbles approach each other and collide resulting either in coalescence or bouncing of the bubbles. They found that the Reynolds number at which the bubbles approach each other and collide decreases with an increase in ~~the~~ Morton number ($Mo = Eo^3/Ga^4$). However, they only considered less viscous surrounding fluid ($Mo < 1.14 \times 10^{-5}$), and no information is given regarding the wake characteristics. Legendre *et al.* (2003) predicted that for every Reynolds number, there exists a separation distance for which the two effects, namely irrotational and wake effects due to viscosity, cancel each other and the drag of the two bubbles becomes equal to that of an isolated bubble. Also, it is correlated with the existence of a boundary in separation distance and Reynolds number phase plot which separates the regions of attraction and repulsion between the bubbles. Recently, a few researchers Islam *et al.* (2015); Velez-Cordero *et al.* (2011) also investigated rising of a pair of bubbles inside a shear-thinning fluid, and found that the attractive motion between the bubbles was increased with the increase in the shear-thinning tendency.

As the above literature review shows, very few studies have been conducted to investigate the detailed three-dimensional flow physics of deformable bubbles rising as a pair. In this part of thesis, we have investigated the rise of a pair of bubbles inside a quiescent liquid in the low inertial (high viscosity) regime and have compared it with the dynamics observed in case of single bubble. Although there exist a few numerical studies (see for instance, Shu & Yang (2013)) of two bubbles rising under buoyancy, their focus was mainly on validating the solver against existing experimental data. A detailed numerical study of a pair of non-deformable bubbles rising in a quiescent liquid was also conducted by Legendre *et al.* (2003). They used boundary fitted grids and considered only a quarter of the domain to simulate flow past fixed spherical bubbles. On the other hand, our study is fully three dimensional, which allows motion and deformation of bubbles in the three dimensional space. In contrast to Legendre *et al.* (2003), we observe the zigzagging and spiralling motion of bubbles, whereas they always predicted a steady force acting between the bubbles.

1.1.3 Dynamics of an air bubble rising in a viscosity stratified medium

As mentioned earlier, the focus of this thesis is to study the behaviour of an air bubble rising in varying viscosity media. Two different approaches have been adopted to achieve the viscosity variation: (a) viscosity stratification by considering a fluid whose viscosity increases linearly with height, and (b) considering shear-thinning fluid in which viscosity of fluid varies due to the shear caused by the motion of the bubble. In this section, we review the literature related to the dynamics of rising gas bubble under the action of buoyancy inside an unbounded domain consisting of another fluid, whose viscosity increases linearly in the vertical direction. In next section, we have reviewed the dynamics of air bubble rising in a shear thinning fluid.

There are several application of viscosity stratification in nature as well as in industry, which provides the motivation to investigate such problems. The viscosity stratification can occur due to several factors, for instance due to the presence of gradients in temperature and concentration of some species/solutes. For example, the viscosity of water or milk is made to increase by almost three orders of magnitude by the addition of only 2% carboxymethylcellulose (CMC) (Ghannam & Esmail, 1997) in the ice-cream and lotion industries. Note that the density changes due to such an addition of the species (CMC) are negligible while varying the viscosity by a large amount. The viscosity in the underground crude oil reservoirs may vary upto three orders of magnitude (Beal *et al.*, 1946). Also, the viscosity stratification is observed because of the variation in composition of the crude oil with depth. In contrast to this, the density does not change by even an order of magnitude within the reservoir. Carbon-dioxide flooding is a common method used for the recovery of crude oil, which may lead to the formation of bubbles of carbon-dioxide in the crude oil. Also, viscosity of molten silicates and metals can be made to vary across several orders of magnitude (Urbain *et al.*, 1982) by maintaining a temperature difference of a few hundreds of degrees Celsius between the top and the bottom wall of a domain. However, the gradients of temperature or concentration at the liquid-gas interface can also give rise to surface tension gradients, which in turn induce tangential stresses, known as Marangoni stresses. This forces the fluid to migrate in the vicinity of the interface separating the fluids. Marangoni flows can be of great importance to a large variety of industrial applications, and thus have been investigated by several researchers (Balasubramaniam & Subramaniam, 1996; Balasubramaniam & Subramanian, 2000; Crespo *et al.*, 1998; Subramanian, 1981, 1983; Subramanian *et al.*, 2002; Tripathi *et al.*, 2015*c*; Young *et al.*, 1959).

In most of the literature considered above, the viscosity stratification is achieved by concentration gradient. Next we will consider the literature relevant to stratification caused due to the temperature gradient. The bubble dynamics due to the temperature gradient was first studied by Young *et al.* (1959). They experimentally investigated rise of small or large air bubbles in a container heated from below. In this study, the resultant dynamics is due to the competition of buoyancy and thermocapillary forces. For small air bubbles, they found that for some imposed temperature gradient, the induced Marangoni stresses acting in the downward direction overcome the buoyancy force, and the bubbles move in the downward direction. However, larger bubbles continue to move in the upward direction. In the later case buoyancy force is the winner. Since then this problem has been studied experimentally, numerically and theoretically by several researchers (Balasubramaniam & Subramaniam, 1996; Balasubramaniam & Subramanian, 2000; Crespo *et al.*, 1998; Subramanian, 1981, 1983; Subramanian *et al.*, 2002; Young *et al.*, 1959). Recently, Tripathi *et al.* (2015*c*) studied the dynamics of rising bubble inside a tube wherein temperature along the wall linearly increases in the upward direction. They considered the surrounding fluid to be of “self-rewetting” type, for which surface tension and temperature dependence is non-monotonic. By considering a quadratic dependence of surface tension on temperature, they found that even though this condition is favourable for bubble rise (in case of common fluids, e.g. air, water, viscous oil, etc), the motion of the bubble can be reversed, and then arrested in “self-rewetting” fluids (e.g. high carbon alcohol solutions). Furthermore, they found that under certain conditions bubble elongated significantly as it rose through the tube. Also, by conducting numerical simulations, Merritt *et al.* (1993) studied the effect of buoyancy and thermocapillarity on rising bubble dynamics. In the limit of large Reynolds and Marangoni numbers, Balasubramaniam (1998) studied this problem by an asymptotic analysis. They also included the temperature varying viscosity, and showed that the steady migration velocity is a linear combination of the velocity for purely thermocapillary motion and the buoyancy-driven rising velocity. However, later Zhang *et al.* (2001) found that inclusion of inertia is crucial in the development of an asymptotic solution for small Marangoni numbers in the presence of temperature field. These studies, although took the viscosity stratification due to temperature gradient into account, the influence of viscosity stratification alone was not provided.

Viscosity stratifications achieved due to the presence of temperature and concentration gradients are continuous. Gradual viscosity variations can be naturally found in the mantle liquid below earth's crust and oceans. The stratification can also be achieved without the presence of temperature and concentration gradients. In several applications (Govindarajan & Sahu, 2014), immiscible fluid-layers of almost the same density, but significant viscosity jump are observed. Bubble rise through an interface of two immiscible liquids of different viscosities have been studied in the past by several researchers (Bonhomme *et al.*, 2012; Kemiha *et al.*, 1991; Manga & Stone, 1995). Practically, all phenomena concerning viscosity stratification invariably include density gradient and other factors, which also influence the dynamics. Although, viscosity stratification is expected to play a significant role, with all the factors included, it is impossible to isolate the effect of viscosity stratification from the dynamics of rising bubble.

In the third part of the thesis, we have investigated the axisymmetric dynamics of a bubble rising in an unconfined viscosity stratified medium. As mentioned earlier, this is frequently encountered in industrial as well as natural phenomena. In spite of the large number of studies carried out on bubbles, a very few studies have examined the influence of viscosity stratification on bubble rise dynamics. None of them have isolated the effects of viscosity-stratification alone, even though it is known to influence the dynamics extensively, which is the main objective of the present study. By conducting time-dependent simulations, we present a library of bubble shapes in the Galilei and the Eötvös numbers plane. Our results demonstrate some counter-intuitive phenomena for certain range of parameters due to the presence of viscosity stratification in the surrounding fluid.

1.1.4 Dynamics of an air bubble rising in a non-Newtonian liquid

In this section, we have reviewed the literature relevant to the study of an air bubble rising in a fluid with shear-thinning property. Many materials encountered in natural phenomena and industries, e.g. blood, proteins, slurries, polymers, emulsions and suspensions, etc, are non-Newtonian in nature, i.e. their viscosities depend on shear rate and/or the yield stress of those materials (Govindarajan & Sahu, 2014). These fluids are described by a variety of non-Newtonian rheological models, such as shear thinning/thickening (power-law), viscoplastic and viscoelastic models, and their variants. Of particular scientific interest in terms of the complex dynamics involved, is the behaviour of a rising bubble in such liquids (Chhabra, 2006, 1993; Tsamopoulos *et al.*, 2008*a*). Also there are several applications, such as chemical, biochemical, environmental, petrochemical processes, where one or more rising bubbles are observed (Kilonzo & Margaritis, 2004; Shah *et al.*, 1982).

Earlier researchers (see e.g. Subramanian (1992); Tripathi *et al.* (2015*b*); Zhang *et al.* (2010)) have shown that the flow fields and dynamics of bubbles in non-Newtonian fluids are quite different from those in Newtonian fluids. A question that naturally arises is, what are these differences and what effects do they have on the bubble behaviour. For example, the difference in behaviour can affect the heat and mass transfer between gas-liquid phases in many applications (Kulkarni & Joshi, 2005). Before discussing the phenomena of rising bubbles in non-Newtonian fluids, the dynamics of a bubbles in Newtonian fluids specifically focusing on the observed path instability is discussed next.

In quiescent Newtonian fluids, several researchers have investigated the hydrodynamics of a rising gaseous bubble theoretically (Cano-Lozano *et al.*, 2013; Magnaudet & Mougin, 2007), experimentally (Bhaga & Weber, 1981; Clift *et al.*, 1978; Tomiyama *et al.*, 2002) and numerically (Bonometti & Magnaudet, 2007; Sussman & Puckett, 2000; Tripathi *et al.*, 2015*a*). Saffman (1956) was the first to investigate the onset of path instability (zigzagging/spiralling motion) of a small air bubble. Since then, several researchers have investigated the path instability in Newtonian fluids, which is observed for high inertia and high surface tension (Cano-Lozano *et al.*, 2016*a*; Tripathi *et al.*, 2015*a*; Zenit & Magnaudet, 2002). Researchers in this area believe that either vortex shedding behind the bubble (Lunde & Perkins, 1997) and/or Crow instability (Crow, 1970; Vries, 2001) are the mechanisms for this zigzagging or spiralling motion of an air bubble in water. However, the exact mechanism is still debatable.Tripathi *et al.* (2015*a*) found that the onset of zigzagging or spiralling motion is associated with the asymmetrical shape deformation and vortex shedding in the wake region of the bubble.

In non-Newtonian fluids, Astarita & Apuzzo (1965) experimentally studied the dynamics of a rising bubble in Carbopol solutions (viscoplastic material). They varied the yield stress of the material by changing the concentration of Carbopol in the solution and investigated the dynamics of an air bubble as a function of yield stress. By performing steady state numerical simulations, Tsamopoulos *et al.* (2008*a*) and Dimakopoulos *et al.* (2013) found that a bubble reaches to a steady shape for some values of Bingham number (the dimensionless number associated with yield stress of the material). They also found that the bubble gets arrested for large Bingham number (high yield stress). Recently, Tripathi *et al.* (2015*b*) have performed unsteady simulations for a wider range of parameters in the inertial regime by considering a regularised Herschel-Bulkley model (Frigaard & Nouar, 2005) for the surrounding fluid. They showed that the bubble does not reach to a steady state in the presence of inertia and in the case of weak surface tension. By performing experiments on a gas bubble rising in an elastic non-Newtonian surrounding fluid, Hassager (1979) found that the liquid behind the bubble moves in the downward direction, opposite to that of the rising bubble. This phenomena was termed as negative wake as it is in contrast to the wake in case of Newtonian fluids, where the wake rises up along with the bubble.

Another type of non-Newtonian fluid is a power-law fluid, whose viscosity decreases (shear thinning) or increases (shear thickening) with shear/strain rate. A few researchers (e.g Kishore *et al.* (2007); Kulkarni & Joshi (2005); Ohta *et al.* (2003, 2005*b*); Zhang *et al.* (2010)) studied the dynamics of a rising bubble in shear-thinning fluids. Zhang *et al.* (2010) studied this problem by performing experiments and axisymmetric numerical simulations. They used solutions of carboxymethyl cellulose (CMC), sodium hydroxyl-ethyl cellulose (HEC) and xanthan gum as the surrounding fluids. The viscosities of these solutions were measured as a function of shear rate and the empirical constants associated with the Carreau-Yasuda rheological model were calculated for these fluids. Then, using these constants, axisymmetric numerical simulations were conducted and the flow patterns around the bubble were investigated via contour plots of viscosity and velocity. Ohta and co-workers (Ohta *et al.*, 2012, 2009) conducted three-dimensional numerical simulations of a rising bubble in shear-thinning and thickening fluids described by the Carreau-Yasuda rheological model. The dimensionless parameters considered in their studies were arbitrarily chosen and they investigated the bubble dynamics for a limited range of parameters. Moreover, a very small computational domain was used and the results are presented mostly in terms of shapes of the bubble and viscosity contours.

In the fourth part of the thesis, we investigate the dynamics of a rising bubble in a Carreau-Yasuda shear-thinning fluid by conducting numerical simulations and experiments using carboxymethyl cellulose(CMC) solutions. In our study, the experimental results obtained using CMC solutions qualitatively agree with those of the corresponding numerical simulations. Our work differs from Ohta and co-workers (Ohta *et al.*, 2012, 2009). We use a larger computational domain to remove the wall effect to get accurate bubble dynamics. The computational domain used by them does not eliminate the wall effect as seen in some of their results where the viscosity variation already reached upto the walls, indicating that wall effect must have been encountered in those situations. An extensive parametric study is also conducted using the rheological constants obtained for real fluids.

1.2 Outline of the thesis

The dynamics of an air bubble rising in quiescent viscosity-stratified media has been investigated in this thesis. For purpose of comparison with the standard system (i.e, constant viscosity system), studies have also been conducted on the rise of single and pair of bubble in

Newtonian fluid. In this chapter, an introduction to the topic of rising bubbles in liquid medium has been presented and extensive literature review is carried out specific to the problems studied in this thesis.

In Chapter 2, the numerical and experimental approaches used in this thesis are discussed in details. These approaches are common for all the studies performed in this work. The boundary conditions and rheological properties specific to each problem are discussed in the corresponding chapters. An extensive validation of the numerical solver used in this study are also presented in Chapter 2.

Before studying the dynamics in viscosity-stratified media, in Chapter 3, an air bubble rising in a Newtonian fluid (namely, in water and glycerol-water solutions) is investigated experimentally. The objective of this study is to reproduce the phase diagram obtained numerically by Tripathi *et al.* (2015*a*). Further, new numerical simulations are conducted to compare our experimental results with those obtained from the numerical simulations. The rise dynamics of the bubble is investigated in terms of shapes, topological changes and trajectories followed by the air bubble for different values of dimensionless numbers. This study is extended to investigate the interaction of two same size bubbles rising side-by-side in Chapter 4. It is found that the presence of the second bubble significantly influence the shape deformation and path instability.

Chapter 5 presents the study of an air bubble rising in viscosity varying media. Two situations are considered. (i) When the bubble rises in a medium having an inherent linear viscosity variation in the vertical direction. In order to isolate the effect of viscosity stratification, the density of the surrounding medium is kept constant. (ii) The dynamics of an air bubble in a non-Newtonian medium. Both axisymmetric and three-dimensional regimes are considered. The non-Newtonian fluid is modelled as a Carreau-Yasuda shear- thinning model. Experiments are conducted using solutions of different concentrations of carboxymethyl cellulose (CMC) in deionised water. These solutions exhibit shear-thinning tendency, and are used to compare the bubble behaviour obtained from our numerical simulations.

in Chapter 6, the concluding remarks and the potential future studies which can be pursued based on the contributions made in this thesis are presented.

CHAPTER 2

Method

In this thesis, the dynamics of an air bubble rising in constant and variable viscosity media has been investigated computationally and experimentally. This chapter contains the details of the computational and experimental methods used in this work.

2.1 Computational approach

The three-dimensional computational approach used throughout this work is discussed in this section. The axisymmetric version of the approach can be easily deduced from this formulation. An extensive validation of the solver used in the present study is also conducted by comparing with the previous numerical and experimental results.

2.1.1 Formulation

The following formulation provides a general methodology to study the dynamics of an air bubble rising in a viscosity-stratified medium. The specific viscosity model for the surrounding medium will be discussed in the subsequent chapters.

The motion of an air bubble (fluid 'i') of initial radius R rising under the action of buoyancy inside a square channel (of width H and height L) filled with an incompressible fluid 'o' is investigated. The schematic diagram of the computational domain is shown in Figure 2.1. A Cartesian coordinate system (x, y, z) is used to model the flow dynamics. Initially, the air bubble and the surrounding fluid are stationary, with the air bubble placed at $z = z_i$. Gravity acts in the negative z direction. It is to be noted here that a rising air bubble undergoes an increase in volume as it rises, but for the vertical distances it travels in the present simulations, we have estimated a volume change of $< 0.5\%$. Thus, we assume the flow to be incompressible in the present numerical study.

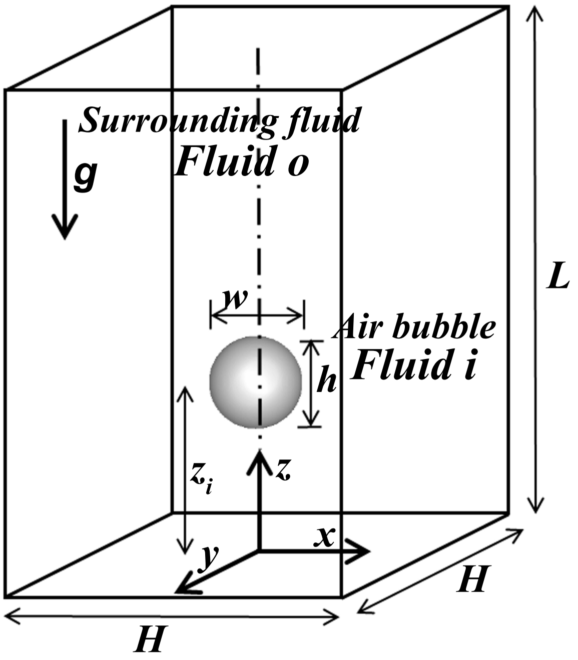

Figure 2.1: Schematic diagram showing the initial configuration of an air bubble (fluid 'i') rising in a liquid (fluid 'o'). Initially the bubble is located at $z = z_i$. H is the width and breadth, and L is the height of the rectangular computational domain. The gravity, g is acting in the negative z direction.

The governing equations, which describe the dynamics of a rising bubble in a surrounding medium are the equations of mass and momentum conservation:

$$\nabla \cdot \mathbf{u} = 0, \tag{2.1}$$

$$\rho \left[\frac{\partial \mathbf{u}}{\partial t} + \mathbf{u} \cdot \nabla \mathbf{u} \right] = -\nabla p + \nabla \cdot \left[\mu (\nabla \mathbf{u} + \nabla \mathbf{u}^T) \right] + \delta \sigma \kappa \mathbf{n} - \rho g \mathbf{j}, \tag{2.2}$$

where $\mathbf{u} = (u, v, w)$ denotes the velocity field in which u, v and w represent the velocity components in the x, y and z directions, respectively. The interface separating the air and liquid phases is obtained by solving an advection equation for the volume fraction of the liquid phase, c ($c = 0$ and 1 for the air and liquid phases, respectively):

$$\frac{\partial c}{\partial t} + \mathbf{u} \cdot \nabla c = 0, \tag{2.3}$$

where p is the pressure field, t denotes time, $\mathbf{j}$ denotes the unit vector along the vertical direction, σ and g represent the (constant) interfacial tension for the pair of fluids considered and gravitational acceleration, respectively, δ is the Dirac delta function (given by $|\nabla c|$), and $\kappa = \nabla \cdot \mathbf{n}$ is the interfacial curvature, in which $\mathbf{n}$ is the outward-pointing unit normal to the interface. In Eq. (2.2), the surface-tension force is included as a body force term using the formulation proposed by Brackbill *et al.* (1992).

The density, ρ, and the viscosity, μ, are assumed to depend on c as

$$\rho = c\rho_o + (1-c)\rho_i, \tag{2.4}$$

$$\mu = c\mu_o + (1-c)\mu_i, \tag{2.5}$$

where ρ_i, μ_i and ρ_o, μ_o are the density and dynamic viscosity of the dispersed (air) and the continuous (liquid) phases, respectively. Note that μ_o is modelled depending upon the the type of fluid considered in the respective problem.

The following scaling is used to non-dimensionalise the above governing equations:

$$(x,y,z) = R\left(\widetilde{x},\widetilde{y},\widetilde{z}\right),\ t = \frac{R}{V}\widetilde{t},\ \mathbf{u} = V\tilde{\mathbf{u}},\ p = \rho_o V^2 \widetilde{p},\ \mu = \mu_o\widetilde{\mu},\ \rho = \rho_o\widetilde{\rho},\ \delta = \widetilde{\delta}/R, \tag{2.6}$$

where the velocity scale is $V = \sqrt{gR}$, and the tildes designate dimensionless quantities. After dropping tildes from all nondimensional variables, the governing dimensionless equations are given by

$$\begin{aligned}
\nabla\cdot\mathbf{u} &= 0, && (2.7)\\
\frac{\partial\mathbf{u}}{\partial t} + \mathbf{u}\cdot\nabla\mathbf{u} &= -\nabla p + \frac{1}{Ga}\nabla\cdot\left[\mu(\nabla\mathbf{u} + \nabla\mathbf{u}^T)\right] + \delta\frac{\nabla\cdot\mathbf{n}}{Eo}\mathbf{n} - \rho\mathbf{j}, && (2.8)\\
\frac{\partial c}{\partial t} + \mathbf{u}\cdot\nabla c &= 0, && (2.9)
\end{aligned}$$

where the dimensionless density and dynamic viscosity are given by

$$\rho = c + (1-c)\rho_r, \tag{2.10}$$

$$\mu = c + (1-c)\mu_r. \tag{2.11}$$

Here, $Ga(\equiv \rho_o g^{1/2}R^{3/2}/\mu_o)$ and $Eo(\equiv \rho_o g R^2/\sigma)$ denote the Galilei number and the Eötvös number, respectively. Note that the Galilei number is similar to the Reynolds number, but defined using $\sqrt{gR}$ as the velocity scale, whereas the latter is usually defined based on the terminal velocity of the bubble. As we do not know the terminal velocity *a priori*, we prefer to use the Galilei number in our simulations. μ_r $(\equiv \mu_i/\mu_o)$ and ρ_r $(\equiv \rho_i/\rho_o)$ represent the viscosity and density ratios, respectively.

2.1.2 Numerical method

A finite-volume open source code, *Gerris* (Popinet, 2003) is used to solve the dimensionless governing equations (5.2)-(2.9). The interface between the two fluids is tracked using the volume-of-fluid (VOF) approach with dynamic adaptive grid refinement based on the vorticity magnitude and the position of the interface. *Gerris* uses a generalized height-function method for calculating the curvature of the interface, thus improving the accuracy of the surface tension force calculation for the VOF methods. It is to be noted that *Gerris* minimizes the spurious currents (to the machine error) at the interface (which are known to appear when the density ratio and the interfacial tension are high) by incorporating a balanced force height-function continuum-surface-force formulation (Brackbill *et al.*, 1992; Popinet, 2009) for the inclusion of the surface force term in the Navier-Stokes equations. Another feature of *Gerris*, the dynamic adaptive mesh refinement, allows one to cluster the grid more in the desired regions dynamically, thus saving the computation time remarkably.

2.1.3 Validations

The *Gerris* solver has been validated extensively. We present below a few validation cases by comparing the results obtained from our solver with the previously reported numerical and experimental results which are relevant to the bubble dynamics.

Comparison with numerical results of Sussman & Smereka (1997)

The evolution of shapes of the bubble at different times for $Ga = 100$, $Eo = 200$, $\rho_r = 0.001$, $\mu_r = 0.01$ are presented in Fig. 2.2. It can be seen that for this set of parameters the bubble is almost spherical till $t = 0.4$. For $t > 0.4$ the bubble undergoes significant deformation and subsequent topological change at $t = 1.6$. Thereafter the bubble continues to move in the upward direction as an annular doughnut-like structure. It is to be noted here that the bubble shapes presented in Fig. 2.2 are in excellent agreement with the numerical simulation (level-set method) results of Sussman & Smereka (1997) for this set of parameters.

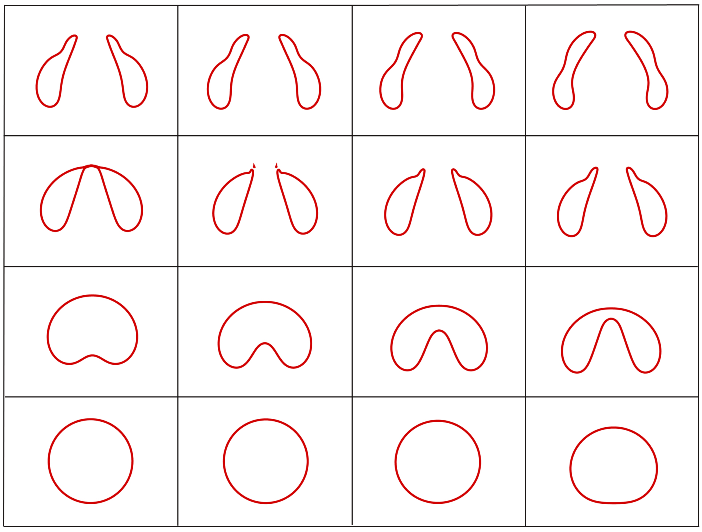

Figure 2.2: The time evolution of the shapes of the bubble for $Ga = 100$, $Eo = 200$, $\rho_r = 0.001$, $\mu_r = 0.01$. From left to right and from bottom to top: $t = 0$; 0.2; 0.4; 0.6; 0.8; 1; 1.2; 1.4; 1.6; 1.8;2;2.2; 2.4; 2.6; 2.8 and 3. The shapes of the bubble agree well with those presented in Sussman & Smereka (1997).

Comparison with experimental results of Bhaga & Weber (1981)

The terminal shapes obtained from our numerical simulation both axisymmetric and three-dimensional are compared with the experimental results of Bhaga & Weber (1981) for different values of Ga and Eo in Figs. 2.3 and 2.4, respectively. In Fig. 2.3, the pictures in the black and white background are the experimental results of Bhaga & Weber (1981) and the red lines show the terminal shape of the bubble obtained from the present (axisymmetric) simulations. Figure 2.4 also shows the comparison of terminal shape of the bubble with Bhaga & Weber (1981). The top row are the experimental results whereas the results in the bottom row are obtained from the present three-dimensional simulations.

Furthermore, the streamline patterns in the wake of the bubble for different Ga and Eo are also plotted. In Fig. 2.5, the left and right hand sides in each panel represent the present simulation results and the experimental results, respectively. It can be seen that the bubble shapes and the streamline patterns are in excellent agreement.

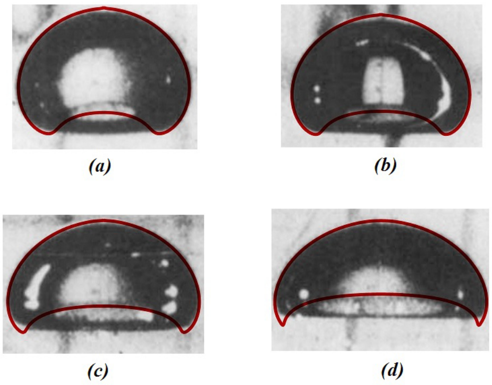

Figure 2.3: Comparison the terminal shapes of an air bubble rising in aqueous sugar solutions obtained from our numerical simulations with those of Bhaga & Weber (1981). (a) $Ga = 2.315$, (b) $Ga = 3.094$, (c) $Ga = 4.935$ and (d) $Ga = 8.157$. The rest of the parameters are $Eo = 29$, $\mu_r = 8.152 \times 10^{-6}$ and $\rho_r = 7.473 \times 10^{-4}$.

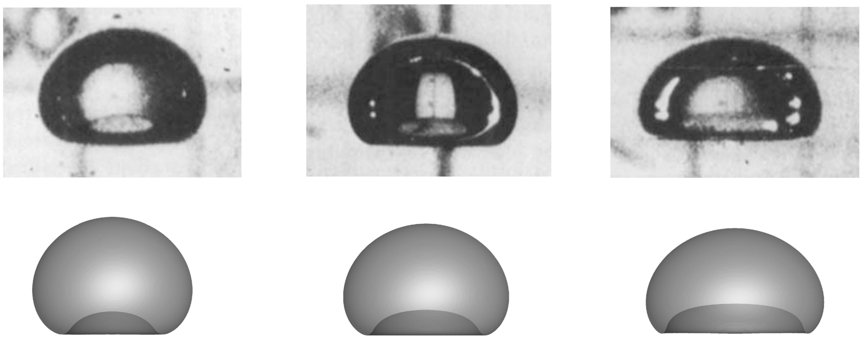

Figure 2.4: Comparison the terminal shapes of an air bubble rising in aqueous sugar solutions obtained from our numerical simulations with those of Bhaga & Weber (1981). (a) $Ga = 2.315$, (b) $Ga = 3.094$ and (c) $Ga = 4.935$. The rest of the parameters are $Eo = 29$, $\mu_r = 8.152 \times 10^{-6}$ and $\rho_r = 7.473 \times 10^{-4}$.

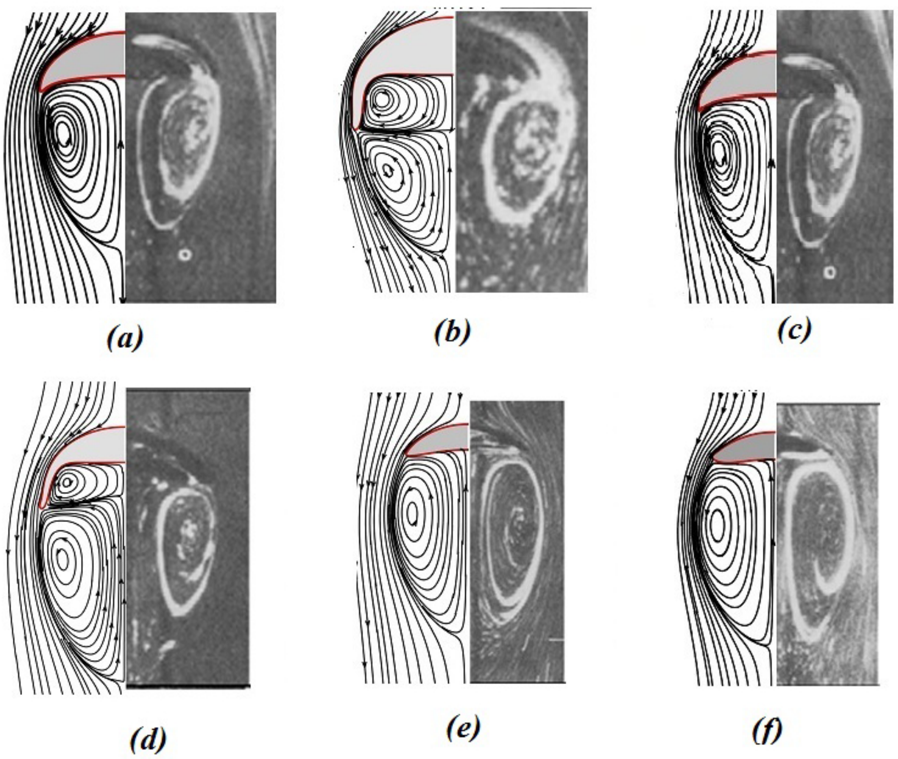

Figure 2.5: Comparison of streamline patterns along with the terminal shapes of the bubble (shown by red lines) obtained from the present simulation (on the left hand side of each panel) with those presented in Bhaga & Weber (1981) (right hand side of each panel) for (a) Ga = 10.96, Eo = 24.05, (b) Ga = 12.61, Eo = 29, (c) Ga = 17.54, Eo = 23.9, (d) Ga = 24.72, Eo = 37.75, (e) Ga = 41.12, Eo = 23.57, and (f) Ga = 46.1, Eo = 15.47. The rest of the parameter values are $\mu_r = 8.152 \times 10^{-6}$ and $\rho_r = 7.473 \times 10^{-4}$.

2.2 Experimental approach

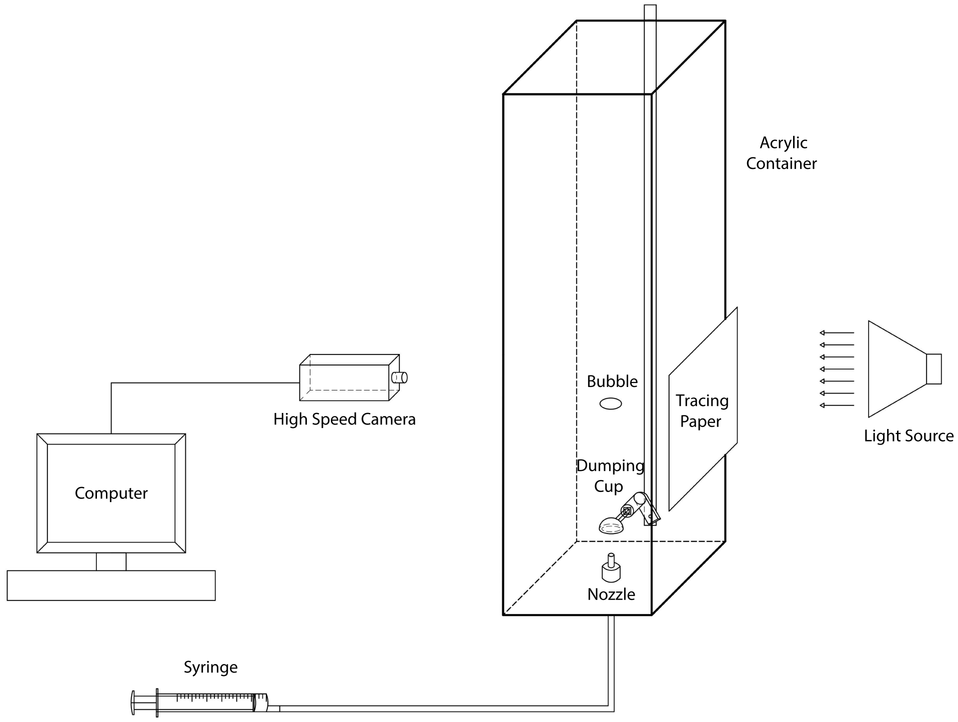

Figure 2.6: Schematic diagram (not to scale) showing different parts of the experimental set-up.

The experimental set-up consists of (i) an acrylic tank of size 200 mm × 200 mm × 700 mm, (ii) a stainless steel nozzle (inner diameter 0.6 *mm*) fitted at the center of the bottom wall of the tank and connected to a syringe (50 *mL* capacity) at its other end, (iii) a hemispherical dumping cup mechanism, and (iv) a high-speed camera (Photron FASTCAM SA1.1) along with back-lit illumination system and a computer. The schematic diagram of the experimental setup is shown in Fig. 2.6. The acrylic tank is used to hold the surrounding fluid. The fluid in the tank is kept at a constant height of 300 mm (from the bottom of the tank) for all experiments. The cross-sectional dimensions of the tank are chosen such that the distance from the bubble to tank wall is about 10 times the maximum bubble radius used in our experiments. This minimises the wall effect on the bubble dynamics.

A stainless steel nozzle along with the dumping cup mechanism is used to create bubbles of different sizes inside the tank. The top end of the nozzle extends to a height of about 30 *mm* from the bottom wall of the tank at its center. The other end of the nozzle is connected to a syringe through a Poly-Tetra-Fluoro-Ethylene (PTFE) tubing. In order to create the bubbles, air is filled inside the syringe and is released by pushing the plunger with the help of a syringe pump. The air comes out through the nozzle opening inside the tank in the form of individual bubbles. These bubbles are small, spherical in shape and consistent in size ($\sim$ 1.4 *mm* radius). For creating bubbles of larger sizes, a dumping cup mechanism is used. It consists of three components: (i) a cup shaped part with a hemispherical dome in the end, (ii) a holder, which is connected to the bottom wall of the tank through a ball bearing, and (iii) a rod connected to one end of the holder for rotating the cup. Although the individual bubbles leaving from the nozzle are small, when they are collected inside the dumping cup they coalesce together to form a larger air bubble. The size of big bubble is calculated from the volume of air collected in the dumping cup as a volume of a sphere of an equivalent volume. The maximum equivalent radius of the bubble used in this experiment is 26.7 *mm*.

The size of bubbles are calculated from the volume of air collected in the dumping cup. Note that rotating the dumping cup creates a lateral thrust on the bubble. However, we control this effect by rotating the dumping cup very slowly. It is also observed that the disturbances created by the dumping cup die down quickly as the bubble starts rising. In case of CMC solutions (highly viscous fluid), the disturbances die down even faster as compared to the Newtonian fluid. Moreover, the bubble motion significant distance away from the dumping cup is considered for data acquisition. Thus, we confirm that the disturbances created due to the release of the bubble from the dumping cup has negligible effect on the results presented.

Almost all the experimental techniques in bubble dynamics uses the differences in refractive indices of water and air to visualize the bubble. In our set-up, the bubbles are recorded by using the high-speed camera (Photron FASTCAM SA1.1), which is capable of capturing 675000 frames/second (fps) at reduced resolutions. In all our experiments, a resolution of 448×800 pixels and a frame rate of 3000 fps are used. This camera is connected through a LAN port to a computer with Photron FASTCAM Viewer (PFV) application installed in it. The camera can be controlled by using this PFV software. Two LED lighting systems along with the controller (Videoflood Controller by Visual Instrumentation Corporations) were installed opposite to the camera. These provide illumination using a diffused back-lighting method (using a tracing paper), which allows a clear visualization of the bubble boundaries on a light background.

CHAPTER 3

An air bubble rising in a Newtonian fluid: An experimental study

In this chapter, shapes and paths of an air bubble rising inside a liquid are investigated experimentally. A phase plot in the Galilei and Eötvös numbers plane, which separates distinct regimes in terms of bubble behaviour is presented. Direct numerical simulations are conducted to study the bubble dynamics, which show excellent agreement with the corresponding experiments. The similarities and differences between the experimental and numerical results are discussed in detail. To the best of our knowledge, none of the previous studies have shown an experimentally obtained phase plot for such a large range of Galilei and Eötvös numbers.

3.1 Experimental procedure

The detailed description of the experimental set-up is discussed in section 2.2. It consists of (i) an acrylic tank, (ii) a stainless steel nozzle fitted at the center of the bottom wall of the tank and connected to a syringe at its other end, (iii) a hemispherical dumping cup mechanism, and (iv) a high-speed camera (Photron FASTCAM SA1.1) along with back-lit illumination system and a computer. To investigate the behaviour of an air bubble in a Newtonian fluid, the acrylic tank is used to hold an aqueous solution of glycerol with ultra pure millipore water (purity of 18.2MΩ), which acts as a surrounding fluid. A total of 19 different concentrations of glycerol in water is used to obtain a wide range of Ga and Eo numbers. The viscosities of these solutions are measured using a MCR 301 rheometer by Anton Paar equipped with a cone-and-plate geometry (diameter: 40 mm, angle: 0.034 radian) at a controlled temperature of 303 K, whereas the other fluid properties, such as density and surface tension are taken from the literature (http://www.aciscience.org/docs/physical-properties-of-glycerine-and-its-solutions.pdf). The properties of these solutions are given in Table 3.1. The fluid in the tank is kept at a constant height of 300 mm (from the bottom of the tank) for all experiments. The cross-sectional dimensions of the tank are chosen such that the distance from the bubble to tank wall is about 10 times the maximum bubble radius used in our experiments. This minimises the

Sample number	% of Glycerol	μ_0 (mPa·s)	ρ_0 (kg/m^3)	σ (mN/m)	Mo
1	100	1657	1260	62.1	230.314
2	99.8	1524	1259	62.2	163.38
3	98.2	1115	1256	62.3	46.48
4	97	967.8	1254	62.4	28.259
5	96	797	1249	62.6	12.9
6	94.8	681	1246	62.8	6.83
7	93.7	581	1243	63.0	3.6
8	92.2	478	1241	63.1	1.6
9	90.8	319.7	1235	63.4	0.3256
10	88.5	258	1230	63.6	0.1372
11	85	170	1222	64.2	0.0253
12	80	96.9	1209	64.8	0.00263
13	70	57.8	1182	65.8	0.000324
14	60	26	1154	66.6	1.315×10^{-5}
15	50	15.1	1127	67.5	1.5×10^{-6}
16	40	9.6	1100	68.4	2.4×10^{-7}
17	25	7	1061	69.5	6.57×10^{-8}
18	10	4.3	1023	69.8	9.56×10^{-9}
19	Pure water	1	1000	72.8	2.52×10^{-11}

Table 3.1: Properties of different aqueous solution of glycerol.

wall effect on the bubble dynamics.

3.2 Numerical procedure

Three-dimensional simulations are conducted to understand the dynamics of a rising air bubble, fluid 'i', in a far denser and more viscous fluid, fluid 'o', under the action of buoyancy. The schematic diagram of the computational domain is shown in Figure 2.1, and the detailed description of the numerical method used is discussed in section 2.1.

A Cartesian coordinate system (x, y, z) is used to model the flow dynamics. Initially, the air bubble and the surrounding fluid are stationary, with the air bubble placed at $z = z_i = 15R$. Gravity acts in the negative z direction. Free-slip and no-penetration conditions are imposed on all the boundaries of the computational domain. It is to be noted here that a rising air bubble undergoes an increase in volume as it rises, but for the vertical distances it travels in the present simulations, we have estimated a volume change of $< 0.5\%$. Thus, we assume the flow to be

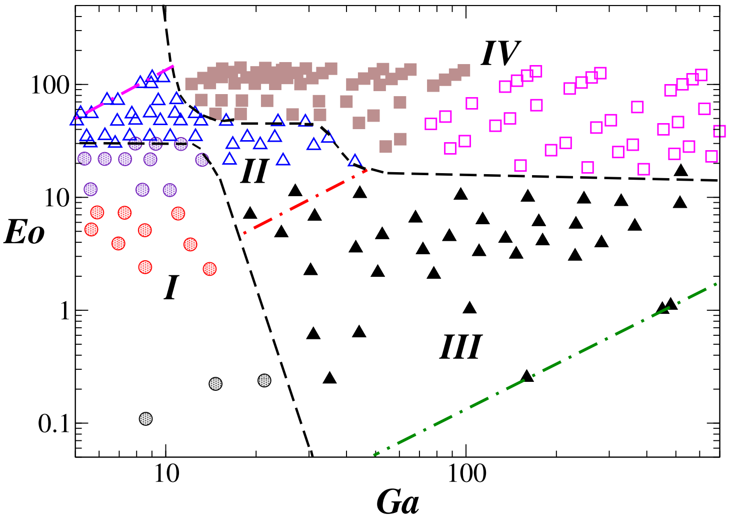

Figure 3.1: Different regions of bubble shape and behaviour. Circles, triangles and squares represent the axisymmetric (region I), skirted (region II), oscillatory (region III) and breakup (region IV) regions, respectively. In region IV, three types of breakup bubbles are observed, namely, skirted breakup (brown filled squares), satellite and toroidal breakups (magenta squares). The red dash-dotted line represents $Mo = 10^{-3}$, which separates region II and region III. The green and magenta lines represent $Mo = 2.52 \times 10^{-11}$ (pure water) and $Mo = 230.3$ (pure glycerol).

incompressible in the present numerical study.

3.3 Results and Discussion

The dynamics of a total of 300 bubbles are analysed in terms of shapes, trajectories, breakups and topological changes and a *Ga*-*Eo* phase plot (Fig. 3.1) is obtained. The phase-plot was obtained by observing the rising behaviour of bubbles visually, and a minimum of 3 runs were performed to check the reproducibility for each parameter combination. Fig. 3.1 shows that although regions I, II and III in the phase plot look qualitatively similar to those obtained numerically by Tripathi *et al.* (2015*a*) (see Fig. 1.2), quantitatively there are differences. One major difference is that unlike five different regions of bubble behaviour in the numerical phase plot, we see only four regions in Fig. 3.1, i.e. in our experiments central breakup (region V) is not observed. The term ‘central breakup’ has been used by the authors for the kind of breakup which results in a toroidal structure without any other significant gaseous regions forming just after the breakup. This unstable toroidal bubble further disintegrates into several smaller bubbles. This is possibly due to the difference in the initial shape of the bubble between simulations and experiments. The initial shape of the bubble used by Tripathi *et al.* (2015*a*) was perfectly spherical, whereas in the experiments it is not possible to inject a spherical bubble into the tank, particularly while dealing with big bubbles, i.e. for high *Ga* and high *Eo*. The effect of initial shape of the bubble was also investigated by Ohta *et al.* (2005*a*). The reader may also note that none of the experimental studies so far have reported central breakup for an air bubble rising in a liquid. Another possible reason for this discrepancy could be the difference in viscosity and density ratios. In the numerical simulations of Tripathi *et al.* (2015*a*)), $\rho_r = 10^{-3}$ and $\mu_r = 10^{-2}$. However, in our experiments the viscosity of the solutions used varies from 1 mPa·s (pure water) to 1657 mPa·s (pure glycerol), while the density varies from 1000 kg/m^3 (pure water) to 1260 kg/m^3 (100% glycerol). In addition, contamination in the tank can also alter the dynamics particularly for smaller bubbles (Duineveld, 1995; Sanada *et al.*, 2008; Vries, 2001). However, we have taken care to minimise this problem by changing the liquid frequently, and minimising the time taken to carry out each experiment while allowing sufficient time for the flow to subside after pouring the liquid. All these variations contribute to the differences observed between Fig. 3.1 and numerically obtained phase plot by Tripathi *et al.* (2015*a*).

Next, we present the bubble behaviours in each region at different dimensionless times, normalised with $\sqrt{R/g}$, and compare the dynamics with that obtained from the numerical simulations.

3.3.1 Region I bubbles

Three types of bubble shapes, namely spherical, oblate and dimpled (for reference see two-dimensional images of Fig. 3.2) can be observed in region I (axisymmetric regime). The differences in shape are evident by visual examination. In Fig. 3.2(a), (b) and (c), the time evolution of shape obtained from the numerical simulations (left column) and experiments (right column) for the spherical, oblate and dimpled bubbles are shown, respectively. The Galilei number is nearly the same (close to 8.5) for these bubbles. For $Eo = 0.109$ (Fig. 3.2(a)), the bubble remains spherical, and increasing the value of *Eo* (i.e, decreasing the interfacial tension), the bubble becomes oblate (Fig. 3.2(b)) and then changes to a dimpled shape (Fig. 3.2(c)). Our observations mostly agree with that of Clift *et al.* (1978), who also observed spherical bubbles for *Eo* below 0.2 (approximately).

Fig. 3.2(d) shows the temporal variation of the position of the tip of the bubble nondimensionalised with the radius of the bubble (z_{tip}) obtained from the experiments (symbols) and numerical simulations (lines). It is observed that in region I, the rise velocity of the bubble decreases with increase in *Eo*, i.e a spherical (dimpled) bubble has the highest (lowest) rising velocity. This is to be expected as the drag force experienced by a spherical bubble is lower

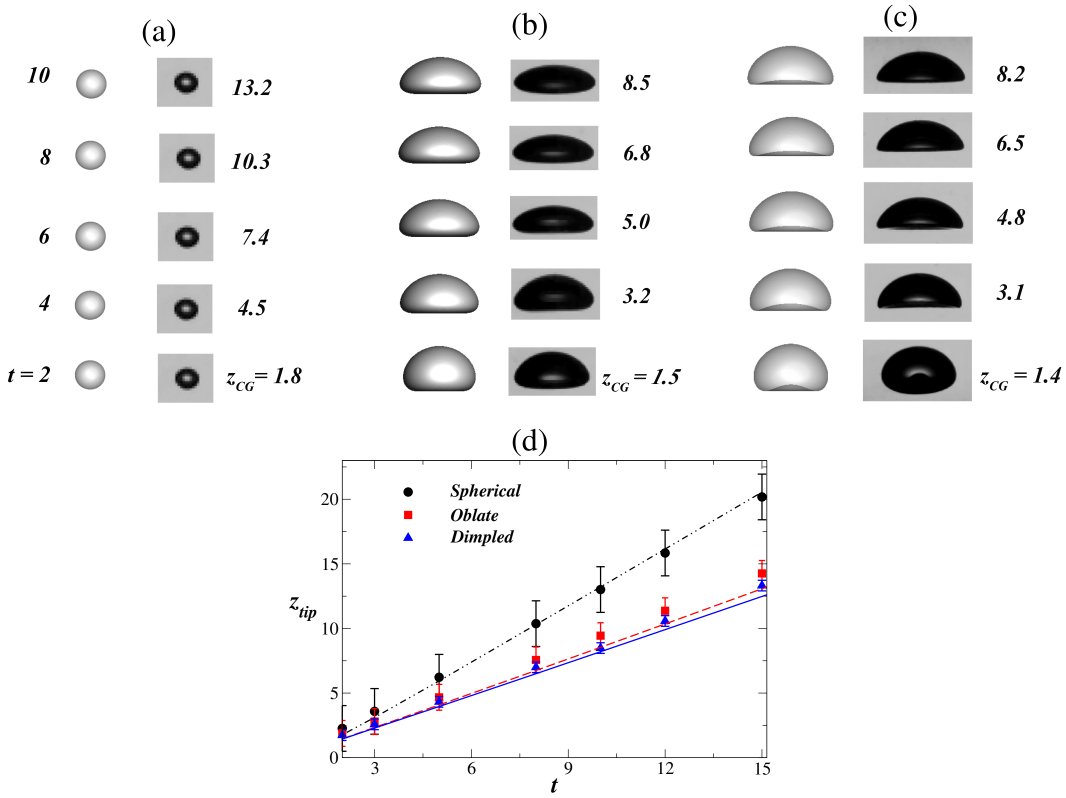

Figure 3.2: Evolutions of region I bubbles: (a) spherical, (b) oblate and (c) dimple shaped bubbles obtained from numerical simulations (first column in each panel) and experiment (second column in each panel). (d) Temporal variations of position of the tip of these bubbles nondimensionlised with the radius of the bubble, z_{tip}; the symbols and lines represent the experimental and numerical results, respectively. The surrounding fluid in (a), (b) and (c) are 40% of glycerol in water (i.e $\mu_r = 1.04 \times 10^{-3}$, $\rho_r = 9.09 \times 10^{-4}$, $Ga = 8.58$ and $Eo = 0.109$), 85% of glycerol in water (i.e $\mu_r = 5.9 \times 10^{-5}$, $\rho_r = 8.2 \times 10^{-4}$, $Ga = 8.52$ and $Eo = 5.11$), and 90.8% of glycerol in water (i.e $\mu_r = 3.13 \times 10^{-5}$, $\rho_r = 8.1 \times 10^{-4}$, $Ga = 8.36$ and $Eo = 11.7$), respectively. The radii of the bubble in panels (a), (b) and (c) are 0.83 *mm*, 5.2 *mm* and 7.8 *mm*, respectively.

than that of an oblate bubble. This behaviour can also be deduced from the streamlines plotted in Fig. 3.3. It can also be noticed in Fig. 3.2(d) that the temporal variations of z_{tip} of the bubbles obtained from the experiments matched with those of numerical simulations within the limit of experimental error.

3.3.2 Region II bubbles

A bubble in region II rises in a straight path, but forms a skirt-like structure along the periphery. The skirted bubbles have been investigated by a few researchers numerically (e.g. Baltussen *et al.* (2014); Ohta & Sussman (2012); Tripathi *et al.* (2015*a*)) and experimentally

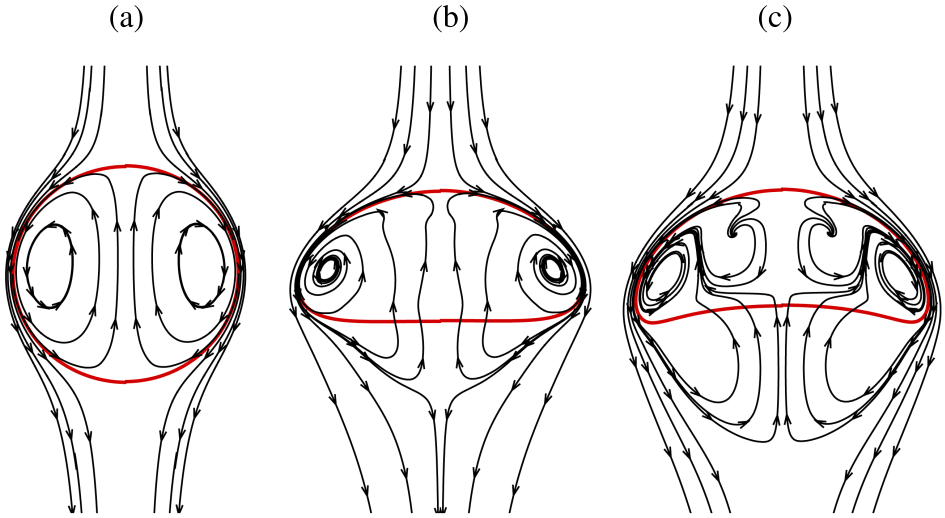

Figure 3.3: Streamlines in the vicinity of the (a) spherical, (b) oblate and (c) dimpled shaped bubbles of region I at $t = 10$ by taking a cross-section at the center of gravity of the bubble in the plane of paper and moving with the frame of reference of the bubble. The shape of the bubble is plotted in red. The parameters are the same as those used in Fig. 3.2.

(e.g. Bhaga & Weber (1981)) in the past. Fig. 3.4(a) shows a typical region II bubble obtained from experiment (right panel) and numerical simulation (left panel). The experiment shows that as the bubble rises, a dimple forms at an early time ($t = 3$). The dimple evolves into a skirt (see the translucent part of the bubble at the bottom), which grows as the bubble rises ($t \geq 4$). For this set of parameters, the skirt does not develop holes, but we see oscillations at the edge of the skirt (see $t = 8$). The corresponding numerical simulation also shows very similar bubble dynamics. Both experiment and numerical simulation show an initial continuous elongation of the skirt, slight oscillation in the shape of the bubble and local oscillations at the edge of the skirt. In our experiment, we found an excellent agreement on the time evolution of a skirted bubble (through high speed imaging) and the corresponding numerical simulation. Fig. 3.4(b) presents the temporal variation of z_{tip} obtained from the experiment and numerical simulation, which also shows a good agreement.

3.3.3 Region III bubbles

Region III bubbles show extensive unsteady behaviour in the paths as well as bubble shapes. A trajectory of an air bubble ($R \approx 2mm$) rising in 25% of glycerol in water solution obtained from the experiment is shown in Fig. 3.5(a). The shapes at different time instants (shown in zoomed view in the left panel) are overlapped to show the trajectory (right panel of Fig. 3.5(a)). In this particular view, the trajectory shows a total deviation of six times the bubble radius

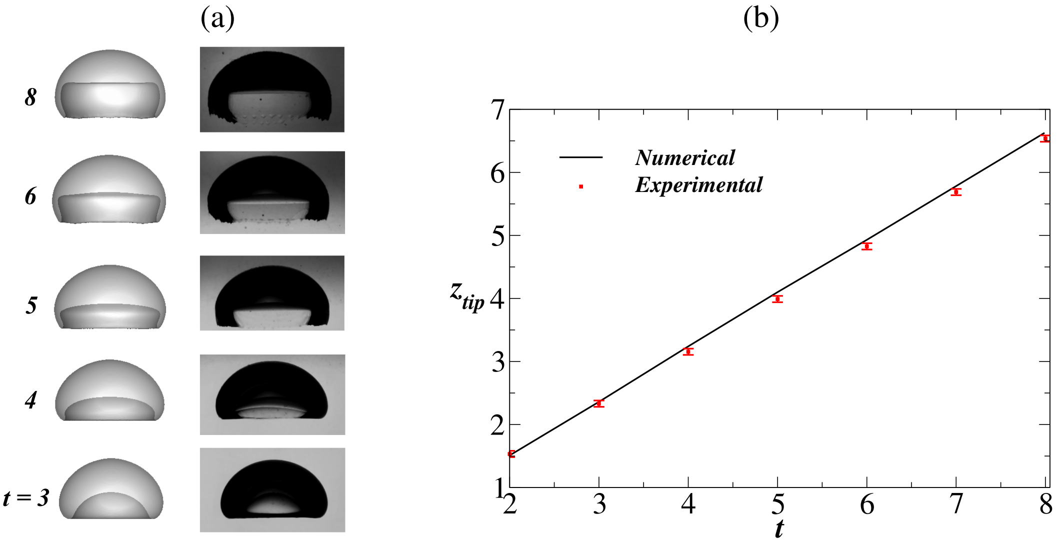

Figure 3.4: (a) Evolution of shapes of a typical skirted (region II) bubble. The left and right panels show the bubble shapes obtained from numerical simulation and experiment, respectively. (b) The temporal variation of z_{tip} obtained from the experiment (symbols) and numerical simulation (solid line). The surrounding fluid is 97% of glycerol in water ($\mu_r = 1.03 \times 10^{-5}$, $\rho_r = 7.97 \times 10^{-4}$, $Ga = 10.86$ and $Eo = 73.28$). The radius of the bubble is 19.27 *mm*.

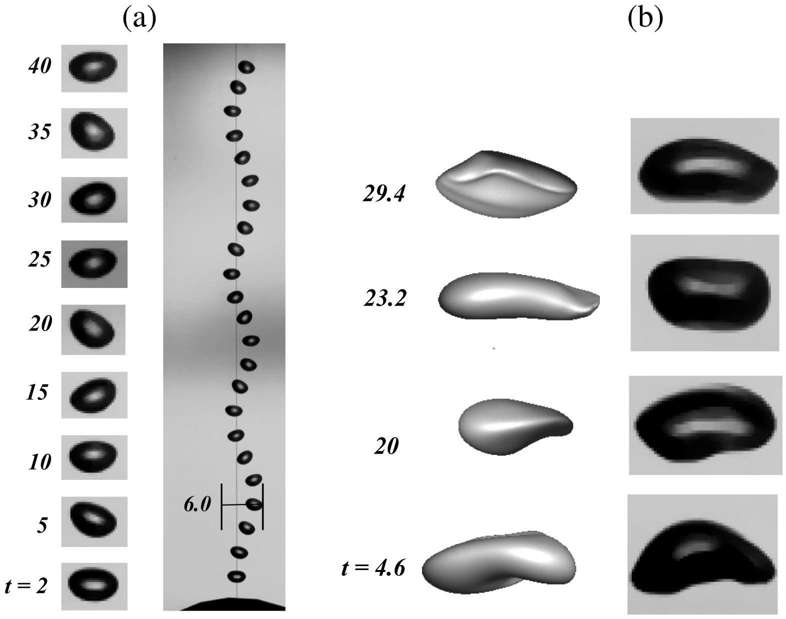

Figure 3.5: Evolution of paths and shapes of two region III bubbles. (a) The left panel shows zoomed view of the shapes of the bubbles at different times and the right panel shows the trajectory of the bubble. The initial bubble radius is 2 *mm* and the surrounding fluid is 25% of glycerol in water ($\mu_r = 1.43 \times 10^{-3}$, $\rho_r = 9.43 \times 10^{-4}$, $Ga = 44.06$ and $Eo = 0.63$). (b) Evolution of bubble shapes at four time instances for an air bubble of initial radius 4.57 *mm* and a surrounding fluid of 10% of glycerol in water ($\mu_r = 2.33 \times 10^{-3}$, $\rho_r = 9.78 \times 10^{-4}$, $Ga = 230.8$ and $Eo = 3$). The left and right panels show numerical and experimental results, respectively.

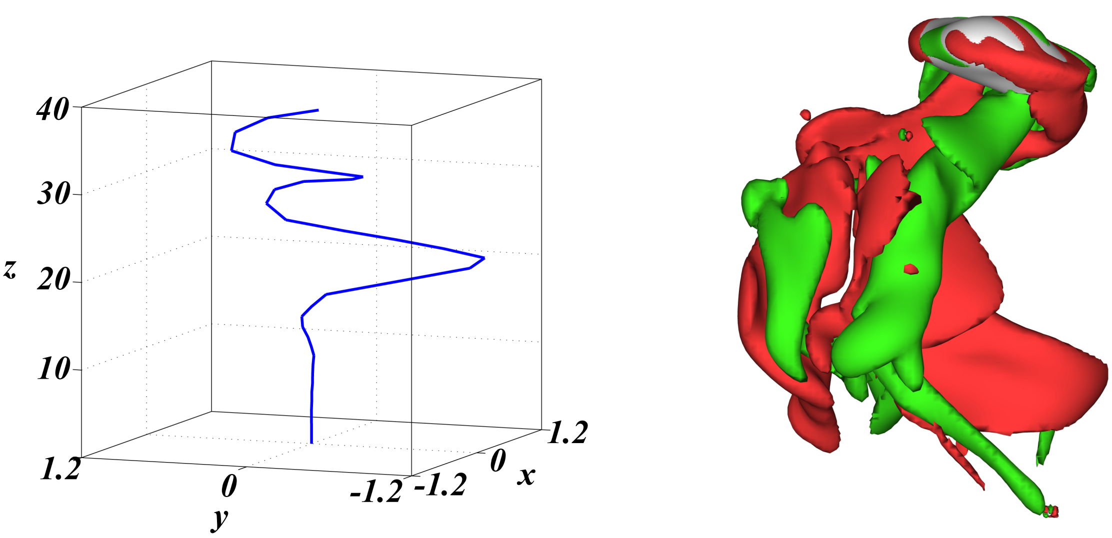
(a) (b)

Figure 3.6: (a) Trajectory and (b) iso-surfaces of the vorticity component in the z direction (magnitude ±0.8) at time $t = 25$ (obtained from numerical simulation). The parameters are the same as those used in Fig. 3.5(b).

about the axis of symmetry (vertical dashed line). The path of the bubble in this case is found to be spiralling. In a recent paper, Cano-Lozano *et al.* (2016*a*) demonstrate that the unsteady shape deformations are related to the rotation of the bubble along the zigzag path. However, the correlation between the shape oscillations and the trajectory of the bubble is not clear.

Fig. 3.5(b) shows the temporal evolution of the shape of another region III bubble of size, $R \approx 4.57\ mm$, obtained from the experiment (right panel) and the numerical simulation (left panel). Note that this bubble (with $Ga = 230.8$ and $Eo = 3$) lies in region IV of Tripathi *et al.* (2015*a*)) (satellite breakup). This bubble falls into region IV based on their numerical simulations with $\rho_r = 10^{-3}$ and $\mu_r = 10^{-2}$. The experimental results for this case are obtained for an air bubble rising in a solution of 10% glycerol in water with $\rho_r = 9.78 \times 10^{-4}$ and $\mu_r = 2.33 \times 10^{-3}$. In the numerical simulation, when we consider the modified viscosity and density ratios, i.e. $\mu_r = 2.33 \times 10^{-3}$, $\rho_r = 9.78 \times 10^{-4}$ instead of $\mu_r = 10^{-2}$, $\rho_r = 10^{-3}$ as considered by Tripathi *et al.* (2015*a*), it is observed that the bubble now does not break and behaves like a region III bubble, which agrees with experiment qualitatively. These results also possibly explain the discrepancy observed in the boundary separating region III and breakup (regions IV and V) (i.e., $Ga > 110$ and $1 < Eo < 10$) between our experimentally obtained phase diagram (Fig. 3.1) with that of Tripathi *et al.* (2015*a*).

Numerical simulation shows that this bubble follows a wobbling motion as shown in Fig. 3.6(a). It is observed that although the shape deformation happens at a very early time ($t = 4.6$)

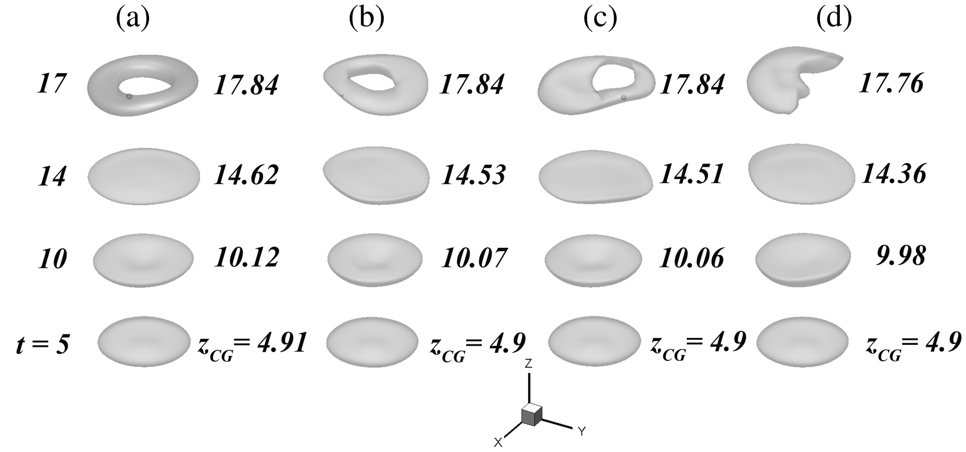

Figure 3.7: Effect of viscosity ratio on the evolution of shapes: (a) $\mu_r = 10^{-1}$, (b) $\mu_r = 10^{-2}$, (c) $\mu_r = 10^{-3}$ and (d) $\mu_r = 10^{-4}$. The rest of the parameters are $\rho_r = 10^{-3}$, $Ga = 230.8$ and $Eo = 3$. The locations of center of gravity, z_{CG} of the bubble at different times are also shown. The shapes shown in panel (b) correspond to a region V bubble (central breakup) in Tripathi *et al.* (2015*a*).

(see Fig. 3.5(b)), the bubble travels in a straight path till $t \approx 15$. This is in accordance with the finding of Cano-Lozano *et al.* (2016*a*), as discussed above. The iso-surfaces of the vorticity component in the z direction at $t = 25$ are shown in Fig. 3.6(b). The pair of streamwise vortices result in a lift force, which is responsible for the nonzero horizontal velocity component of the bubble. It is also found that the occurrence of streamwise vorticity in the wake coincides with the path instability.

Effect of viscosity and density ratios

The result presented above (Fig. 3.5(b)) also reveals that a change in viscosity ratio (with a negligible change in density) can change the bubble region from central breakup (region V) to oscillatory region (region III). This motivated us to investigate the effect of changing the viscosity and density ratios on bubble behaviour. Numerical simulations were conducted by separately varying μ_r and ρ_r while keeping the rest of the parameters constant.

In Fig. 3.7, μ_r is varied from 10^{-1} to 10^{-4} while the rest of the parameters are kept fixed at $\rho_r = 10^{-3}$, $Ga = 230.8$ and $Eo = 3$. It can be seen that for $\mu_r \geq 10^{-3}$ (Fig. 3.7(a), (b) and (c)), the bubble undergoes central breakup to form a doughnut-like or toroidal shape, which becomes unstable at later times and breaks down into smaller bubbles (not shown). It is found that bubbles in Fig. 3.7(a), (b) and (c) travel in a straight path. This is consistent with the finding of Tripathi *et al.* (2015*a*) for an air-water system ($\mu_r = 10^{-2}$ and $\rho_r = 10^{-3}$) for $Ga = 230.8$ and $Eo = 3$. Decreasing the viscosity further to $\mu_r = 10^{-4}$, the bubble behaves like a region

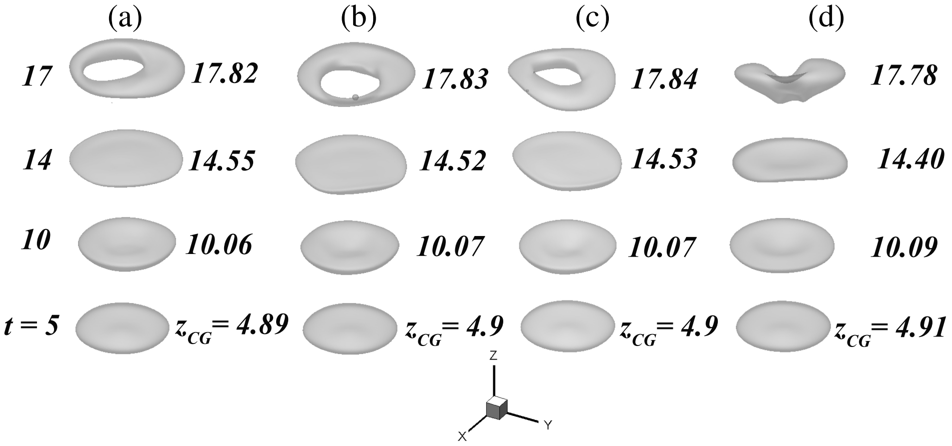

Figure 3.8: Effect of density ratio on the evolution of shapes: (a) $\rho_r = 10^{-1}$, (b) $\rho_r = 2 \times 10^{-3}$, (c) $\rho_r = 10^{-3}$ and (d) $\rho_r = 10^{-4}$. The rest of the parameters are $\mu_r = 10^{-2}$, $Ga = 230.8$ and $Eo = 3$. The locations of center of gravity, z_{CG} of the bubble at different times are also shown. The shapes shown in panel (c) correspond to a region V bubble (central breakup) in Tripathi *et al.* (2015*a*).

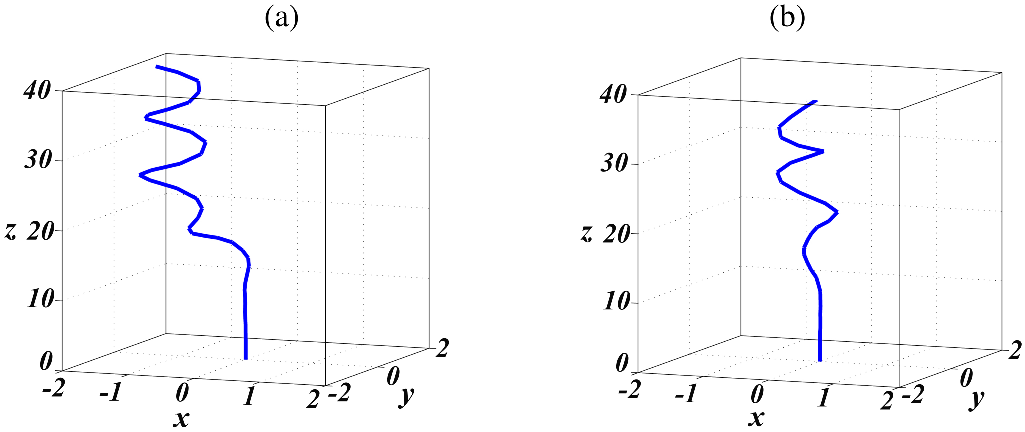

Figure 3.9: Trajectories of the bubble for (a) $\mu_r = 10^{-4}$, $\rho_r = 10^{-3}$, $Ga = 230.8$, $Eo = 3$, and (b) $\mu_r = 10^{-2}$, $\rho_r = 10^{-4}$, $Ga = 230.8$, $Eo = 3$.

III (oscillatory/wobbling) bubble (see Fig. 3.7(d)). The trajectory of the bubble for $\mu_r = 10^{-4}$ is shown in Fig. 3.9(a). We found that vortex shedding behind the bubble (which occurs for $\mu_r = 10^{-4}$ for this set of parameters) promotes this oscillatory motion by adjusting its shape without allowing it to break.

The effect of density ratio (varying from 10^{-1} to 10^{-4}) on bubble shapes for $\mu_r = 10^{-2}$, $Ga = 230.8$ and $Eo = 3$ is presented in Fig. 3.8. It can be seen that for $\rho_r \geq 10^{-3}$ (Fig. 3.8(a), (b), (c)) the bubble undergoes topological change to form a doughnut-like shape (region V of Tripathi *et al.* (2015*a*)), but behaves like an oscillatory bubble (region III) for $\rho_r = 10^{-4}$ (see Fig. 3.8(d)). The oscillatory path of this bubble is shown in Fig. 3.9(b).

The mechanisms behind the central breakup observed for large liquid-to-gas density and viscosity ratios are discussed below. In the literature, two types of mechanisms were suggested for the toroidal breakups: (i) inertial upward jet mechanism (Walters & Davidson, 1963) and (ii) downward jet pinch-off mechanism (Bonometti & Magnaudet, 2006; Collins, 1965). In the inertia dominated regime, as the bubble rises, it deforms by the additional pressure generated due to the hydrostatic pressure head equivalent to $2\rho_o g R$ between the top and bottom poles of the bubble. This in turn creates an upward liquid jet which squeezes the bubble in the vertical direction. This deformation is counteracted by the surface tension force, in general. In this competition between the inertia and surface tension forces, if inertia wins, then the bubble breaks from the centre to form a toroidal bubble. The downward jet pinch-off could be explained as follows. The rise in pressure at the front pole of the bubble is balanced by the capillary pressure and the normal viscous stress. However, if the capillary effects are small (high Eo) and if the viscous forces are also small as compared to the inertial forces (high Ga), the pressure excess at the front pole causes a downward jet to destabilize the interface (Bonometti & Magnaudet, 2006).

We observe a third kind of toroidal breakup which occurs for a much higher value of surface tension although it resembles the downward jet mechanism. It can be seen in Figs. 3.7 and 3.8 that the bubble attains a disc-like shape and keeps on expanding its circumference, eventually resulting in a breakup from the center. It is to be noted that a large fraction of air accumulates in the peripheral regions rather than the central part, thus making the bubble increasingly thinner at the center. This could be explained as follows. The formation of counter-rotating vortices in the wake, move the fluid outwards from the center of the bubble. This action causes the bubble to form an increasingly thinner core which punctures at a later time. Moreover, the bubble remains flat in these cases due to high inertia.

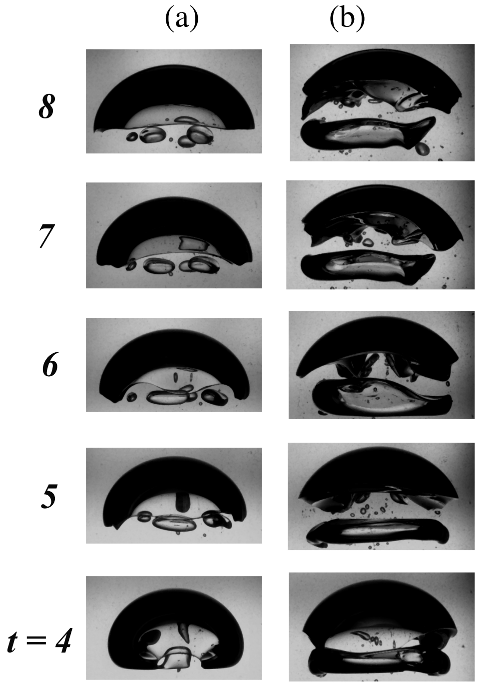

Figure 3.10: Evolution of breakup bubbles (region IV): (a) 70% of glycerol in water and 22.8 *mm* bubble radius ($\mu_r = 1.73\times10^{-4}$, $\rho_r = 8.46\times10^{-4}$, $Ga = 221.5$ and $Eo = 92.1$), and (b) 80% of glycerol in water and 26.7 *mm* bubble radius ($\mu_r = 5.9\times10^{-5}$, $\rho_r = 8.27\times10^{-4}$, $Ga = 171$, $Eo = 131$).

3.3.4 Breaking-up bubbles: bubbles in region IV

The numerical phase diagram of Tripathi *et al.* (2015*a*) indicates that there are two types of breakups for bubbles, namely peripheral (region IV) and central (region V) breakups. However, in the experimental phase diagram (Fig. 3.1) the central breakup is not observed. Within the region classified as breakup, we only observed peripheral-type breakups, which we have further classified as skirted, satellite and toroidal breakups. In the skirted breakup region, a thin skirt forms on the periphery of the bubble which breaks to form small satellite bubbles rising in the wake region following the main bubble. The satellite and toroidal breakups seem to happen arbitrarily and there is no specific boundary between them. Two recorded cases of each of these breakups are shown in Fig. 3.10(a) and (b), respectively. In case of the satellite breakup (Fig. 3.10(a)), the bubble breaks near the center to form satellite bubbles (at the wake) and a spherical cap bubble. For toroidal breakup (Fig. 3.10(b)), a ring-like structure is detached from the main body of the bubble. Walters & Davidson (1963) have predicted this kind of breakup for an initially spherical bubble rising in an inviscid liquid. They found the toroidal bubble to be stable, but we see that the presence of unsteadiness in the wake of the bubble makes the system of bubbles unstable.

3.4 Concluding remarks

The dynamics of a rising air bubble inside aqueous solutions of glycerol is investigated resulting in a phase plot in the Galilei and Eötvös numbers plane, which separates four distinct regions in terms of bubble behaviour, namely axisymmetric, skirted, spiralling and break-up regions. The experimental results are compared with those of numerical simulations to show the similarities and differences. The differences observed in the breakup region are attributed to the difficulty in creating a perfectly spherical bubble in experiment, particularly when the size of the bubble is large, i.e. for high Ga and high Eo. Apart from Reynolds and Eötvös numbers, which were thought to be the only important governing parameters for rising bubbles in air-liquid systems, our results show that the actual density and viscosity ratios are also required to describe the bubble dynamics accurately, especially in the parameter space close to the region boundaries in the phase-plot.

CHAPTER 4

Two initially spherical bubbles rising in quiescent Newtonian liquid

A pair of bubbles starting from rest and rising side-by-side in a liquid have been shown earlier to display spherical and ellipsoidal shapes. In contrast to earlier computational studies on the two-dimensional dynamics of a pair of bubbles, in this chapter, we study the fully three-dimensional motion of the bubbles in the inertial regime. We reveal the destabilizing nature of the interaction between the wakes of the bubbles, which causes them to rise in an oscillatory path. Such three dimensionality sets in earlier in time than for a single bubble and also at a lower inertia. The interaction leads to a mirror symmetry in the trajectories of the two bubbles, which persists for some time even in the high inertia regime where each path is chaotic. The effect of the inertia and initial separation on the mirror symmetry of the path, the vortex shedding pattern and the attraction/repulsion between the bubbles are examined. The bubble rise has been interestingly observed to be symmetrical about the plane perpendicular to the separation vector for all separation distances considered in the present study.

As discussed in Chapter 1, the hydrodynamics of a single bubble in quiescent liquid has been studied both computationally (see e.g. Baltussen *et al.* (2014); Dijkhuizen *et al.* (2010); Sussman & Puckett (2000)) and experimentally (see e.g. Bhaga & Weber (1981); Clift *et al.* (1978)). The experimental investigation on this subject provides a library of bubble shapes, including skirted, spherical cap, and oscillatory and non-oscillatory oblate ellipsoidal. Recently, Tripathi *et al.* (2015*a*) conducted three-dimensional numerical simulations of an initially spherical gaseous bubble rising under buoyancy in a liquid, and identified five different regions (shown in Fig. 4.1), which agree well with the gross features obtained in the experimental study of Bhaga & Weber (1981). It was shown in the computational study (Tripathi *et al.*, 2015*a*) that in region I (which corresponds to low Eötvös number, Eo ($\equiv \rho_o g R^2/\sigma$) and low Galilei number, Ga ($\equiv \rho_o \sqrt{gR}R/\mu_o$)) the bubble maintains azimuthal symmetry. The bubble shapes in this region are either spherical, oblate or dimpled. In region II (high Eo and low Ga), a bubble form axisymmetrical cap with a thin skirt trailing from the main body of the bubble (known as skirted bubble). A bubble in region III (low Eo and high Ga) rises in a zigzag or a spiral path. A region

III bubble remains its integrity but its shape changes with time due to the influence of relatively low surface tension force, but high inertial force as compared to an axisymmetric (region I) bubble. This phenomenon, commonly known as path instability (Mougin & Magnaudet, 2002; Tomiyama *et al.*, 2002; Veldhuis *et al.*, 2008). A bubble in regions IV and V undergoes different types of break-ups, namely peripheral break-up (region IV) and central break-up (region V). In this chapter, we have investigated the rise of a pair of bubbles inside a quiescent liquid in the low inertial (high viscosity) regime and have compared it with the dynamics observed in case of single bubble.

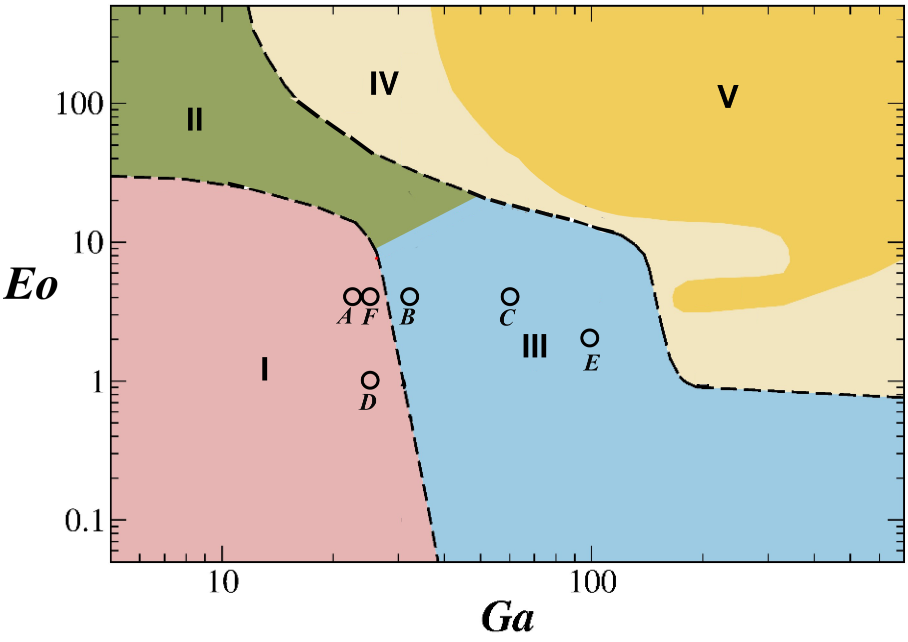

Figure 4.1: Different regions in $Ga - Eo$ plane. Region I: axisymmetric; region II: skirted, region III: zigzagging or spiralling, region IV: peripheral break-up, and region V: central break-up. Also shown are the points A, B, C, D, E and F which corresponds to (Ga,Eo) = (22.4,4), (32,4), (60,4), (25,1), (100,2) and (25,4), respectively. These sets of Ga and Eo are considered in the present study. This figure is a modified plot taken from Tripathi *et al.* (2015*a*).

4.1 Formulation

The governing equation and numerical method used to study this problem is the same as those discussed in Chapter 2. However, the differenence here is the presence of two bubbles instead of one.

A schematic diagram of flow configuration considered in this study is given in Fig. 4.2. Two air bubbles (designated by '1' and '2' of fluid '*i*') of equal radius R rise side-by-side under

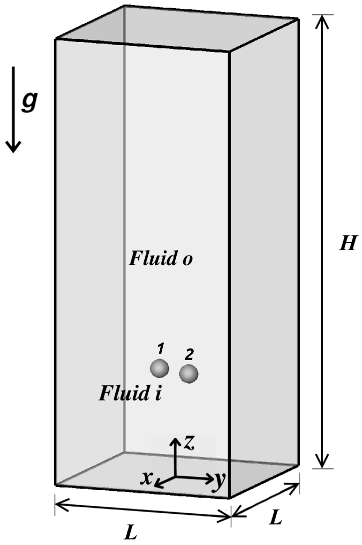

Figure 4.2: Schematic diagram showing the initial configuration of the bubbles of equal radius R (designated by '1' and '2') rising under the action of buoyancy inside a square computational domain of width L and height H. The gaseous and the liquid phases are designated by 'i' and 'o', respectively. The two bubbles are initially separated by a distance q along the y coordinate, and placed at $z = 10R$ initially. The value of L, and H are fixed at $40R$ and $120R$, respectively. The acceleration due to gravity, g acts in the negative z direction.

the action of buoyancy inside a square channel of width L and height H filled with a liquid (designated by fluid 'o'). A Cartesian coordinate system (x, y, z) is used to model the flow dynamics. Gravity acts in the negative z direction. At time $t = 0$, the two spherical air bubbles '1' and '2' are kept at $(0, -q/2, 10R)$ $(0, q/2, 10R)$, respectively. Initially, the air bubbles and the surrounding fluid are stationary. Three-dimensional numerical simulations are performed to understand the rising dynamics of the bubbles. In order to minimise the boundary effect, the outer boundaries are kept far away from the bubbles. Free-slip and no-penetration conditions are imposed on all the boundaries of the computational domain.

4.2 Results and discussion

The non-dimensional parameters in this problem are the Galilei number, the Eötvös number and the initial horizontal separation q between the bubbles, expressed as a multiple of a bubble radius. The first two, as mentioned above, are defined respectively by

$$Ga \equiv \frac{\rho_o g^{1/2} R^{3/2}}{\mu_o}, \qquad \text{and} \qquad Eo \equiv \frac{\rho_o g R^2}{\sigma}.$$

Ga is a ratio of the inertial to the viscous forces in the problem. It is effectively a Reynolds number, with the velocity scale based on gravity ($\sqrt{gR}$). Eo is also known as the Bond number, giving the ratio of gravitational to surface forces. Throughout this chapter, the values of the density and viscosity ratios are kept fixed at 10^{-3} and 10^{-2}, respectively. First, we study the effect of varying the Galilei number and the initial separation in turn, for a fixed $Eo = 4$.

4.2.1 Effect of bubble inertia (Ga)

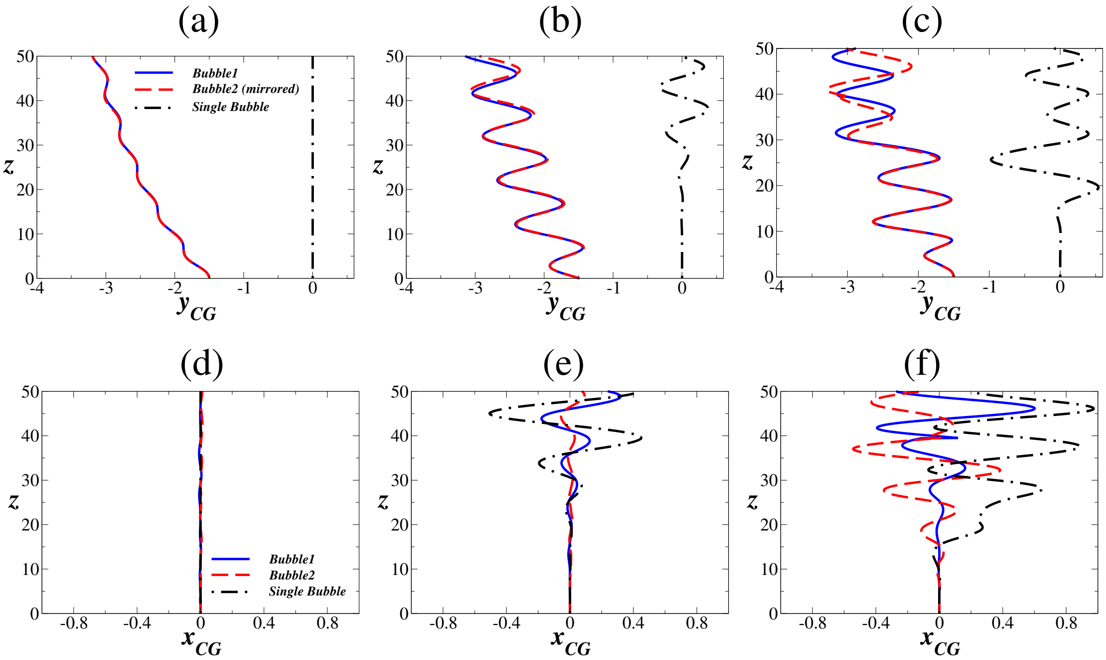

Figure 4.3: Variation of y_{CG} (top panels) and x_{CG} (bottom panels) along the vertical path of the two bubbles released side by side. The Galilei numbers in each case are (a,d) $Ga = 22.4$, (b,e) $Ga = 32$, and (c,f) $Ga = 60$. The rest of the parameter values are $Eo = 4$, $q = 3$, $\rho_r = 10^{-3}$ and $\mu_r = 10^{-2}$. The position of the bubble initially placed at positive y (bubble '2') has been mirrored about the x axis in order to compare its path with that of the other bubble. The black dot-dashed lines represent the path a single bubble released at $(x, y, z) = (0, 0, 10R)$ would follow.

The dynamics of two bubbles rising side-by-side are shown for different inertia, i.e., for $Ga = 22.4$, 32 and 60 in Fig. 4.3(a), (b) and (c), respectively. The Eötvös number is kept fixed at $Eo = 4$, and initially the bubbles are separated by a distance $q = 3$ in the y coordinate. These values of Ga are chosen because they represent qualitatively distinct regimes of the behaviour of a single bubble rising in an initially quiescent liquid. This can be seen in Fig. 4.1, where these parameters are denoted by small circles termed as A, B and C. In the context of a single bubble, point A lies well within region I, where the bubble would adopt an axisymmetric shape and, after some initial transience, attain a terminal velocity. Point C lies in region III, where a single bubble would execute zigzagging/spiralling motion. Point B lies in the latter region, but very close to the border between regions I and III. We now wish to examine how the behaviour of the bubble gets modified by the presence of another bubble of the same size rising simultaneously. The horizontal location of the centre of gravity of each bubble is denoted by y_{CG} and x_{CG} in the y and x coordinates, respectively. These positions of the center-of-gravity of the bubbles are presented in the top and bottom panels of Fig. 4.3(a), (b) and (c), respectively as the bubbles rise, as functions of the height z. The path of bubble '2' has been mirrored about the x axis, so that one may easily examine whether the dynamics is symmetric. In order to compare the rise dynamics with the single bubble behaviour, the variations of y_{CG} and x_{CG} obtained for a single bubble rising in the same liquid are plotted by black dot-dashed lines.

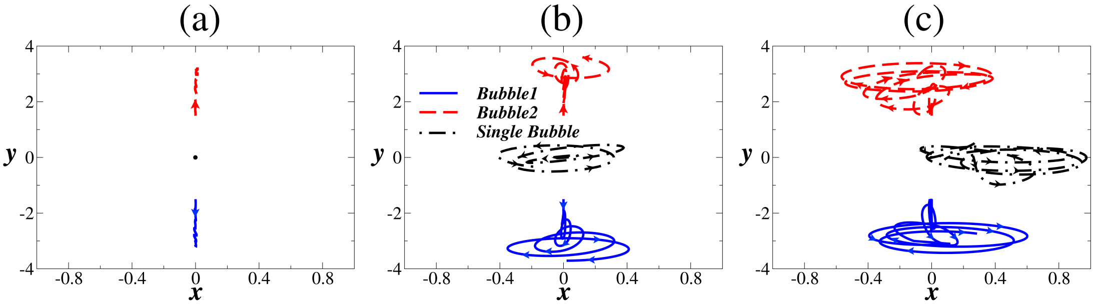

Figure 4.4: The top view of the trajectories of the two bubbles for (a) Ga = 22.4, (b) Ga = 32, and (c) Ga = 60. The top view of the trajectories of the single bubble are also shown by black dot-dashed lines. The other parameter values are the same as in Fig. 4.3.

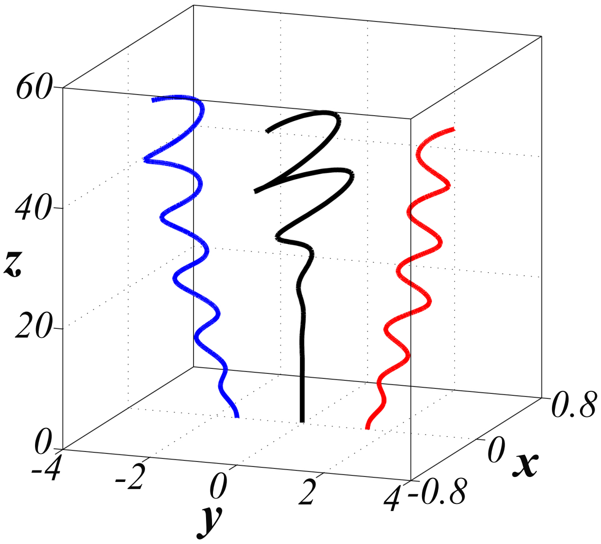

Figure 4.5: Three dimensional trajectories of single bubble (shown in black) and bubble pair (shown in indigo and red) for Ga = 32. The rest of the parameter values are the same as in Fig. 4.3.

The effect that is immediately evident is that the bubbles move away from each other progressively, i.e., their horizontal separation in y shows an overall tendency to increase. This increase is modulated by oscillations. At low inertia, where a single bubble would merely have travelled vertically upwards at constant velocity, the two bubbles show small amplitude oscillations in the y-z plane as they move away from each other (Fig. 4.3(a)), and their motion in the x-axis is negligible, so the dynamics remains two-dimensional. For $Ga = 32$ and 60 (Fig. 4.3(b,c)), the frequency of pitch of the spiralling motion of the bubbles in the y-z plane is 0.12. In the case of single bubble, as well, it is nearly the same (0.118). For $Ga = 22.4$, the two bubbles oscillate at a frequency 0.11 (Fig. 4.3(a)), but the single bubble does not oscillates but merely migrates vertically along the axis of symmetry. The bubbles for $Ga = 22.4$ migrate away from each other achieving a terminal vertical velocity and a small spreading angle (made with the z axis) of radians. This migration is modulated by small amplitude oscillations. Thus the transition to oscillatory behaviour sets in at a lower Galilei number than in the single bubble case. In other words, the dynamics of a single bubble for $Ga = 22.4$ and $Eo = 4$ lies completely in the axisymmetric region (region I in Fig. 4.1), i.e., the bubble rises along a vertical line, whereas the two bubbles display an increasing separation modulated by small amplitude oscillations. The bubbles for $Ga = 32$ also move away from each other at a spreading angle (with the z axis) of 0.017 radians, but modulated now by high amplitude oscillations. In contrast, the dynamics of the bubbles for $Ga = 60$ appears to be chaotic. For two bubbles, the amplitude of oscillations at later times are 0.175, 0.708 and 1.2 for $Ga = 22.4$, 32 and 60, respectively. In the case of a single bubble, the amplitude of oscillations are much smaller, at 0.0317 and 0.157 for $Ga = 32$ and 60, respectively. Inspection also reveals that for $Ga = 32$ and 60, single bubble rises in a straight vertical path initially and then oscillates later. However, it can be seen that the oscillations start from $t = 0$ in case of two bubbles rising simultaneously. Thus the presence of the second bubble significantly increases the amplitude of oscillations, decreases the time of onset of oscillations as well as decreases the Ga at which the transition from steady to oscillatory motion occurs. These changes due to the presence of the second bubble can be directly correlated with the changes in vortex shedding, as will be seen later. In the case shown, the paths of the two bubbles are perfect mirror images of each other about the x-axis. When we examine the top view shown in Fig. 4.4(a), the systematic increase in separation between the bubbles is apparent, and it is clear that the motion is confined to the $y - z$ plane.

At a higher Galilei number (Fig. 4.3(b)) a single bubble begins to display spiralling motion. The two bubbles execute spiralling motion too, while each increases its distance from the other. A breaking of mirror-symmetry is already in evidence. Note that the scale for x_{CG} is exaggerated compared to the one for y_{CG}, but it is clear that the motion is three dimensional now. The top view in Fig. 4.4(b) shows how an initial rapid repulsion is followed by a slowly widening spiral motion. For purposes of illustration, the three dimensional trajectories in this case are shown in Fig. 4.5. Superimposed on the moving apart of the two bubbles, a spiralling motion is seen whose pitch is comparable to its radius, and whose amplitude at later times is smaller than that of a single bubble. At an even higher Galilei number (Fig. 4.3(c) and Fig. 4.4(c)) the dynamics is fully three dimensional, and the asymmetry in the tracks of the two bubbles is very noticeable, as is the irregularity in the spiralling motion. Oscillations set in sooner for the two bubbles case than for a single bubble.

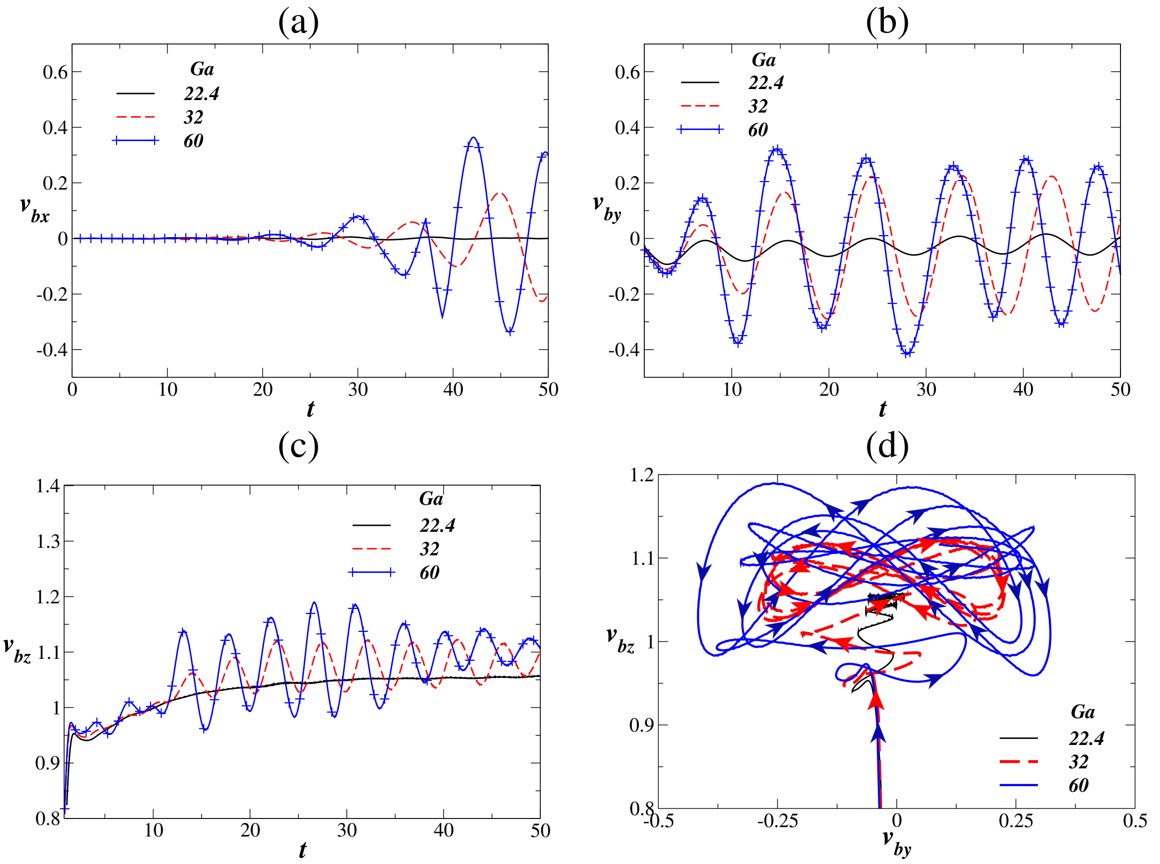

Figure 4.6: Temporal variations of the velocity, v_b of the left bubble (bubble '1') for different values of Ga in the (a) x, (b) y and (c) z directions. The components v_b in the x, y and z directions are v_{bx}, v_{by} and v_{bz}, respectively. (d) Phase portrait (v_{by} versus v_{bz} plot). The other parameter values are the same as in Fig. 4.3.

The trajectories we have seen lead us to expect oscillations in the horizontal velocity components as well, and these are shown as functions of time for the three Galilei numbers in Fig. 4.6 (a) and (b). The temporal variations of vertical velocity component of the bubble, v_{bz} are also shown in Fig. 4.6 (c) for different values of Ga. Interestingly, for the higher Galilei numbers, the vertical velocity shows oscillations (Fig. 4.6 (c)) as well, with the bubbles alternatingly rising slower and faster. The frequency of this variation is twice than that of the horizontal components. The in-plane velocities in the phase portrait of Fig. 4.6 (d) are therefore seen to follow figures of ‘eight’. This oscillation in the vertical velocity is caused by the breaking of left-right symmetry in the two-bubble configuration, and is absent in the single bubble velocity pattern. It can also be seen in Fig. 4.6 (b,c) that only for low Galilei number (Ga = 22.4), the left bubble achieves a terminal velocity in the z-direction (v_{bz} is approximately equals to 1.05), and the variations in other components of bubble velocity, v_{bx} and v_{by} are very small. The average values of v_{bx} and v_{by} for $Ga = 22.4$ are about 0 and -0.02, respectively. The motions of the right and left bubbles are symmetrical about the x axis. Thus, the bubbles for low Ga move away from each other very slowly in the y-z plane at $x = 0$. In other words, for $Ga = 22.4$ and $Eo = 4$, a single bubble rises along a vertical line, whereas the two bubbles display an increasing separation modulated by small amplitude oscillations. The dynamics of the bubbles at high Ga values is three dimensional. The transition from two-dimensional motion to three-dimensional motion occurs at $Ga \approx 30$ for $Eo = 4$. The mechanism of this transition was studied by Cano-Lozano *et al.* (2013, 2016*b*) via a stability analysis. Their study consisted of perturbations on an axisymmetric bubble shape, whereas the presence of another bubbles breaks the axisymmetry of the flow around a given bubble at all Ga. We have seen that this promotes three-dimensionality. For $Ga = 60$, the motion appears to be chaotic. The dimensionless force of attraction and repulsion acting on bubble ‘1’ and ‘2’, which are defined as $m_b a_1$ and $m_b a_2$, are plotted in Fig. 4.7. Here, m_b represents the mass of each bubble, and a_1 and a_2 represent the accelerations of bubble ‘1’ and ‘2’ in the y direction, respectively. Kok (1993*a*) derived the equations of motion for a spherical bubble in the Lagrangian framework using a potential flow approximation, which was later used by Vries (2001) after taking into account the dipole interactions between a vertical wall and a bubble. Additional physics was accounted for in these equations by the authors to obtain the repeated bouncing, sliding and lift effects in the model. The dimensionless lift force derived by Vries (2001) for their experiments is given by $L \approx \pi U_T^2/13$, which in dimensionless form is 0.24. Our bubbles are not restricted to a plane, and are seen to undergo spiralling motion. The main force of one bubble on the other is thus in the azimuthal (horizontal component along the spiral) rather than the radial direction (y). Accordingly the lift forces obtained in the present study (Fig. 4.7) are two orders of magnitude smaller as compared to the magnitudes suggested by these authors. Also, the lift forces obtained by Hallez & Legendre (2011) were of the order of 0.05 for $Ga \approx 100$ and $q = 1$, which too is an order of magnitude larger than the results of the present study. It is to be noted that in the case of Kok (1993*a*), Hallez & Legendre (2011) and Vries (2001), the bubbles were spherical with no motion in the x-direction. Our study displays the importance of a three-dimensional study of bubbles in the flow regime considered in our investigation.

In order to understand the associated shape deformation, while the two bubbles are moving away (for $Ga = 22.4$) or spiralling (for $Ga = 60$), the spatio-temporal evolutions of shape of

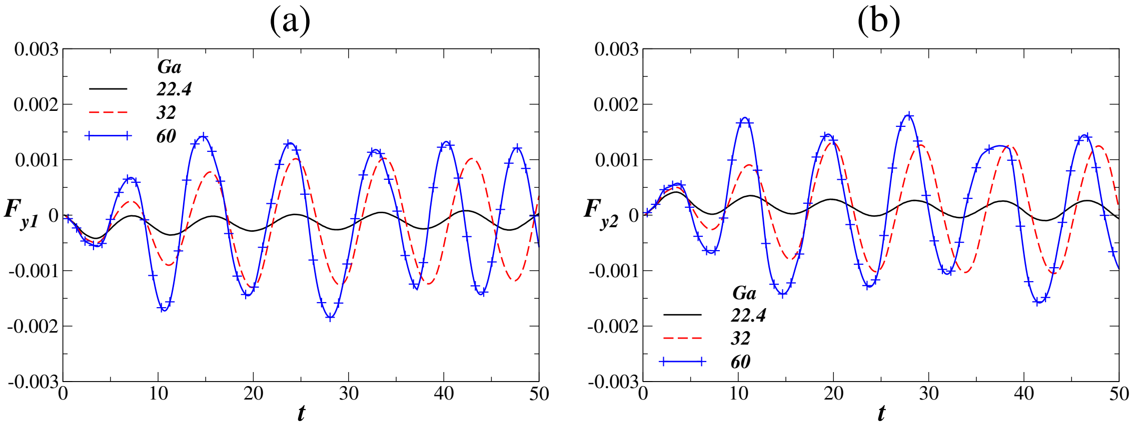

Figure 4.7: Temporal variations of lateral force (in the *y* direction) acting on bubble ‘1’ and ‘2’ for different values of *Ga*. The other parameter values are the same as in Fig. 4.3.

bubbles are shown for these Galilei numbers in Figs. 4.8 and 4.9, respectively. Two views: tilted-side and top views are shown. The shape evolutions of the corresponding case of rising of single bubble are also shown in the right panel of each figure. It can be seen in Fig. 4.8(a) that the two bubbles deform to steady oblate shapes, which look similar to that observed for the single-bubble case. The bubbles remain circular when viewed from the top (Fig. 4.8(b)) as they move away from each other. Unlike for $Ga = 22.4$, in the high Galilei number case ($Ga = 60$), it can be seen in Fig. 4.9(a) and (b) that the bubbles undergo unsteady large asymmetrical deformations, which are evident in both the tilted-side and top views. The deformations are similar to those displayed by a single bubble, but set in sooner than for a single bubble, this difference is visible at $t = 10$ in the figure.

The effect of one bubble on the other is most apparent in the vortex shedding patterns, as shown for different Galilei numbers in Fig. 4.10(a,b,c) at $t = 15$ and (d,e,f) at $t = 30$. The positive and negative values are shown by red and green colors respectively for $\omega_z = \pm 0.3$. At the low Galilei number ($Ga = 22.4$; see Fig. 4.10(a,d)) of regime I motion, there is no visible vorticity in the case of a single bubble, but vorticity is developed in the equatorial plane when two bubbles rise side-by-side. Further the wake of each is distorted from a straight path by the presence of the other wake, with the oppositely signed vortices being drawn to each other. This lead to an asymmetry in the pressure distribution on each bubble, resulting in repulsive motion rather than a solely vertical rise. With the increase in the Galilei number (for $Ga = 32$, see Fig. 4.10(b,e)), vortex shedding occurs in the wake regions in case of two bubbles. It is to be noted that when we plot the vorticity contours for $\omega_z = \pm 0.05$ or less, we observe vortex shedding even in case of single bubble at $Ga = 32$, but vortex shedding does not appear for both the single and two bubbles at $Ga = 22.4$. This is a strong evidence that vortex shedding is the mechanism behind the oscillatory motion of the bubbles. The vortex shedding becomes more

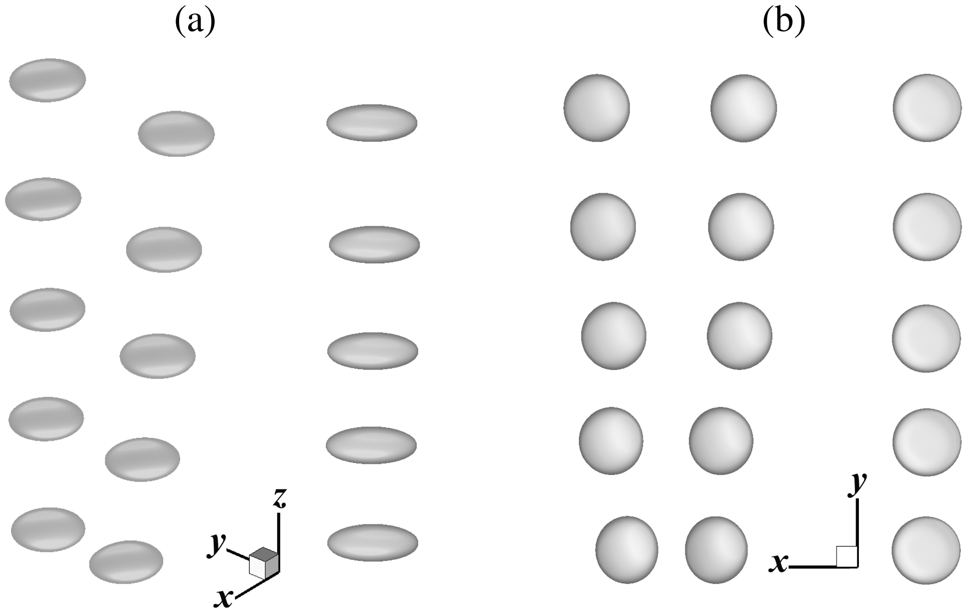

Figure 4.8: Spatio-temporal variation of the shape of the bubble in (a) tilted-side view, and (b) top view for $Ga = 22.4$. From bottom to top: $t = 10$, 20, 30, 40 and 50. The remaining parameter values are the same as in Fig. 4.3.

intense for high Galilei number ($Ga = 60$) as shown in Fig. 4.10(c,f). For $Ga = 60$, a smaller tail (less intense) of vortex shedding appears for the single-bubble case. For the intermediate and high Galilei numbers, the shed vortex from each bubble alternates in sign with time. This results in oscillatory and spiralling behaviour. The shedding from one bubble moreover is out of phase with the shedding from the other bubble and again there is a distortion in the shed pattern, resulting in overall increase in bubble separation, as was seen in figure 4.3.

4.2.2 Effect of initial separation, q

We now examine the effect of initial separation between the bubbles, for a fixed Galilei number of 32. The trajectories are shown in the $y - z$ and $x - z$ planes in figure 4.11. Two features are noteworthy. The first is that the initial increase in bubble separation is stronger when the bubbles are nearer to each other, while at later times they settle into a trajectory which, in the $y - z$ plane alone, does not depend on the initial separation. The frequencies of oscillations for $q = 2.2$, 3 and 4 are found to be 0.1, 0.12 and 0.12, respectively. The amplitude and frequency of oscillations appear to be insensitive to q for the parameter values considered in this study. The speed of the bubbles along the line of separation is shown in figure 4.12, and it is seen that barring a phase, all three initial separations settle into the same oscillation in the

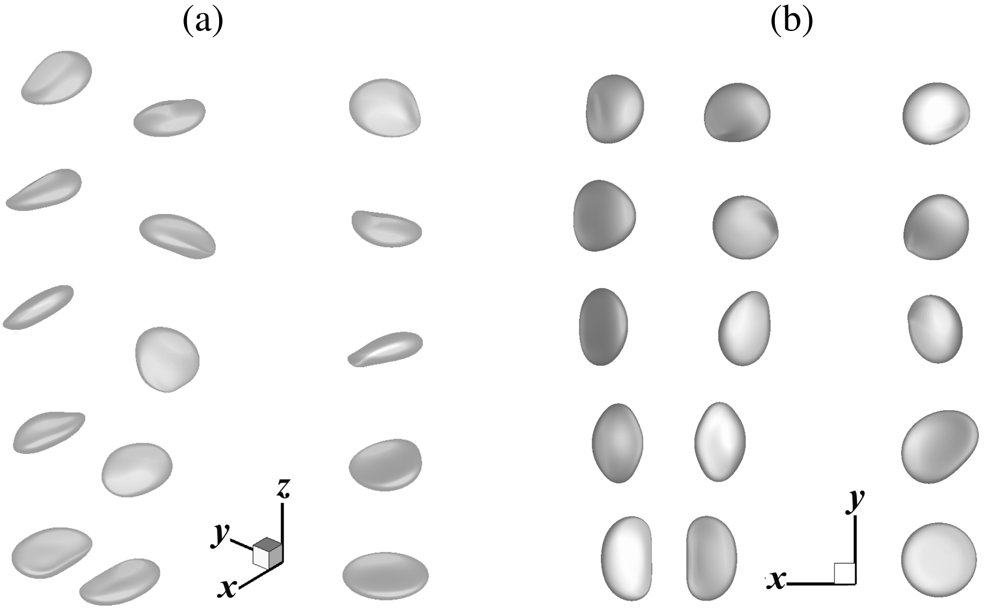

Figure 4.9: Spatio-temporal evaluations of shape of the bubble for (a) tilted-side, (b) top view for $Ga = 60$. From bottom to top: $t = 10$, 20, 30, 40 and 50. The rest of the parameter values are the same as in Fig. 4.3.

speed along the y direction. Thus, for initial separations below a threshold, the dynamics, in the $y - z$ plane alone, at this Galilei number follows a common pattern except at early times.

The second striking feature of this dynamics is that the three-dimensional nature of the trajectories is highly dependent on the initial separation. Bubbles which start life close to each other, remain tightly bound in their futures, displaying trajectories that are mere mirror images of each other, as seen in figure 4.11(a), top and bottom panels. However, this symmetry is broken when bubbles start life further apart. One of the bubbles oscillates gently into the third dimension whereas the other displays large forays in the x (cross) direction. While the dynamics remains out-of-phase in the $y - z$ plane, the phase in the $x - z$ plane of one bubble is not tied to the other. The resulting complete trajectories are seen in figure 4.13. For $q \geq 3$, one of the bubbles has a significantly lower spiralling radius than the other. At all initial separations, both bubbles have smaller spiralling amplitudes than a single bubble does under the same conditions.

4.2.3 Some other cases

In order to understand how the dynamics changes if we slightly vary the parameters, we investigate motion of bubbles for some other sets of (Ga, Eo), designated by points D ($Ga = 25$, $Eo = 1$), E ($Ga = 100$, $Eo = 2$) and F ($Ga = 25$, $Eo = 4$) in Fig. 4.1. In Fig. 4.14(a), the variations of y_{CG} and x_{CG} in the z directions are plotted for bubble ‘1’ and bubble ‘2’ (mirrored about the x axis) for $Ga = 25$ and $Eo = 1$ (point D). This point is slightly closer to the boundary separating regions I and II, i.e. with slightly higher inertia than the bubbles at point A, whose dynamics is investigated in Fig. 4.3(a). It can be seen in Fig. 4.14(a) that the bubbles ‘1’ and ‘2’ migrate away from each other with some path oscillations at the earlier times. The wavelength of these initial oscillations are larger than that of the bubbles at point A (Fig. 4.3(a)). However, the higher surface tension (low Eo) suppresses asymmetrical shape deformations of the bubbles as compared to those associated with point A. This in turn minimises the path oscillations of the bubbles at later times. In Fig. 4.14(a), the bubbles are initially separated by a distance $q = 3$ in the y coordinate.

Then we investigate the rising dynamics of the bubbles at point F for two values of q, i.e. $q = 4$ and 2.2. The value of Eo for point F is the same as that of point A, but Ga is slightly higher than that of point A. In Fig. 4.14(b) ($q = 4$, point F), it can be seen that both the bubbles move away for each other progressively, and this increasing separation is modulated by oscillations. The oscillations in the top panel of Fig. 4.14(b) is larger than those observed in Fig. 4.3(a). In Fig. 4.14(c) ($q = 2.2$, point F), top panel shows that when we increase the initial distance between the bubbles, the lateral motion of the bubble decreases. This can be visualised by comparing the top panels of Fig. 4.14(b) and (c). It can be seen in the bottom panels of Fig. 4.14(b) and (c) that their motion in the $x - z$ plane is negligible. Close inspection also reveals that the amplitude of oscillations increases progressively for $Eo = 4$ (see Fig. 4.14 (b) and (c)), while it decreases for $Eo = 1$ (see Fig. 4.14(a)). The increase in the amplitude of oscillations observed for $Eo = 4$ can be attributed to the larger deformation of the bubbles (due to lower surface tension) as compared to that for $Eo = 1$.

Next, we investigate the dynamics at point E in Fig. 4.14(d). This point is located in the central part of region III and corresponds to a set of parameters in the high inertial regime. It can be seen in the top panel of Fig. 4.14(d) that the motion of the bubbles in the $y - z$ plane is chaotic, although the paths of the two bubbles are perfect mirror images of each other about the x axis till they reach upto $z \approx 40$, after that they deviate slightly from each other. The bottom panel of Fig. 4.14(d) presenting the motion of the bubbles in the $x - z$ plane shows that there is some foray into the third dimension as they rise.

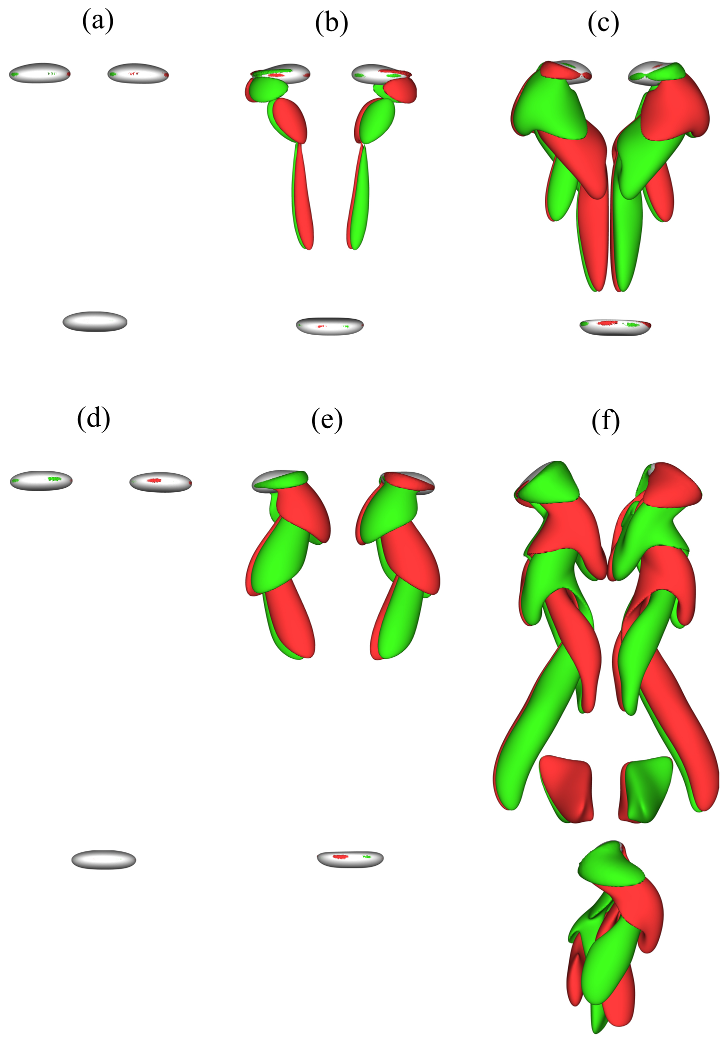

Figure 4.10: Isosurfaces for z vorticity at $t = 15$ (a,b,c) and $t = 30$ (d,e,f) for (a,d) $Ga = 22.4$, (b,e) $Ga = 32$ and (c,f) $Ga = 60$. The positive and negative values are shown by red and green colors respectively; $\omega_z = \pm 0.3$. The top and bottom panels in each subfigure are for two bubbles and single bubble, respectively. The rest of the parameter values are the same as in Fig. 4.3.

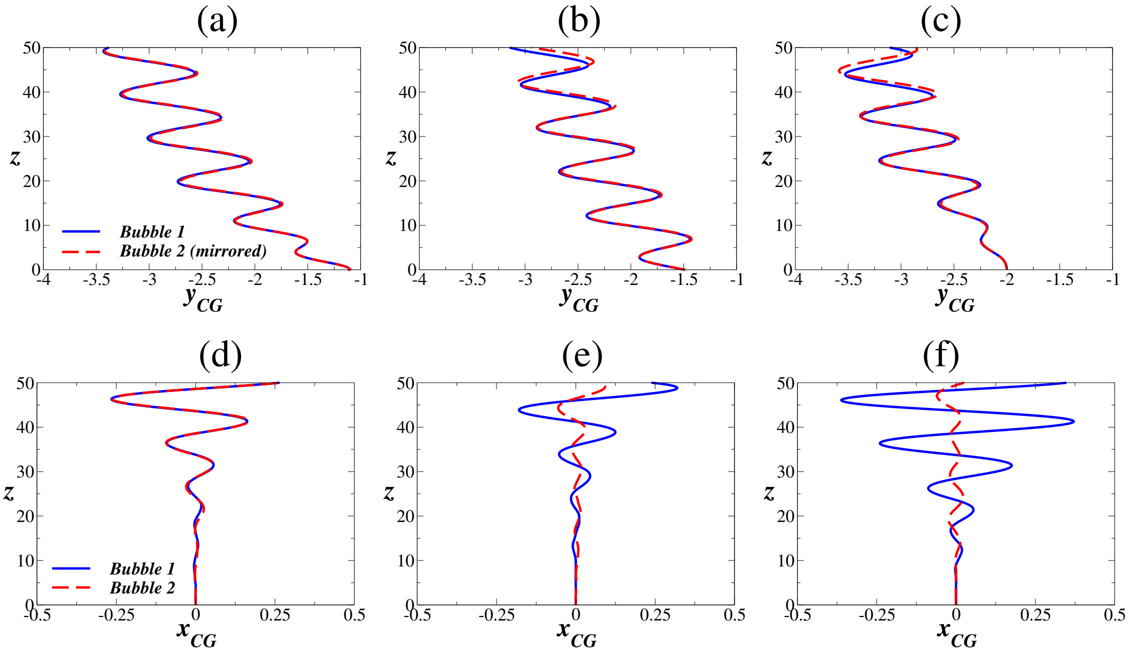

Figure 4.11: Variation of y_{CG} (top panels) and x_{CG} (bottom panels) along the vertical path of the two bubbles released side by side for different values of q: (a,d) $q = 2.2$, (b,e) $q = 3$ and (c,f) $q = 4$. Here $Ga = 32$ and $Eo = 4$ (Point B). The position of the bubble initially placed at positive y (bubble '2') has been mirrored about the x axis in order to compare its path with that of the other bubble.

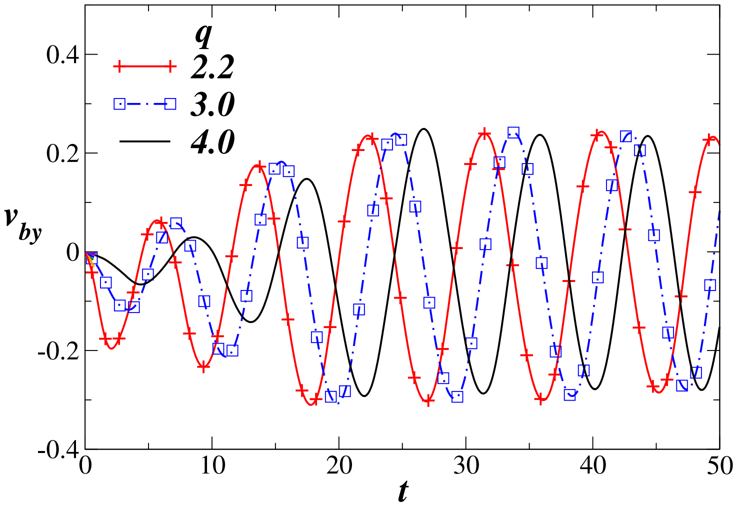

Figure 4.12: Variation of v_{by} (velocity of the left bubble, bubble '1' in the y direction) with time for different values of q. The rest of the parameter values are the same as in Fig. 4.11.

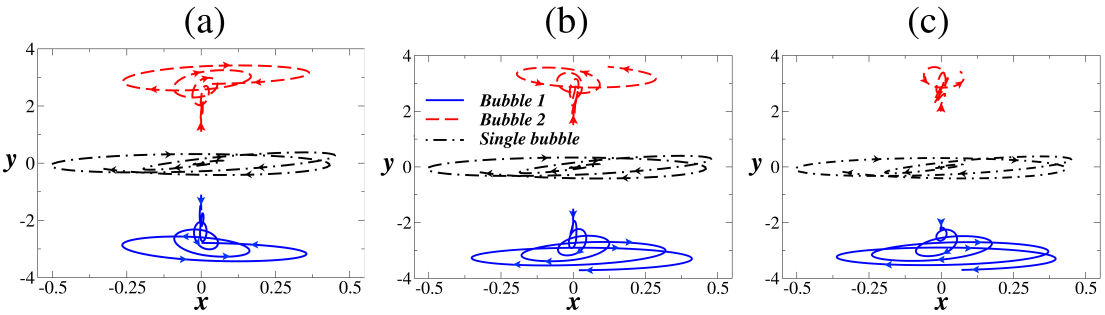

Figure 4.13: The top view of the trajectories of the bubble for (a) $q = 2.2$, (b) $q = 3$ and (c) $q = 4$. The top view of the trajectorie of the single bubble is also shown by black dot-dashed lines. The rest of the parameter values are the same as in Fig. 4.11.

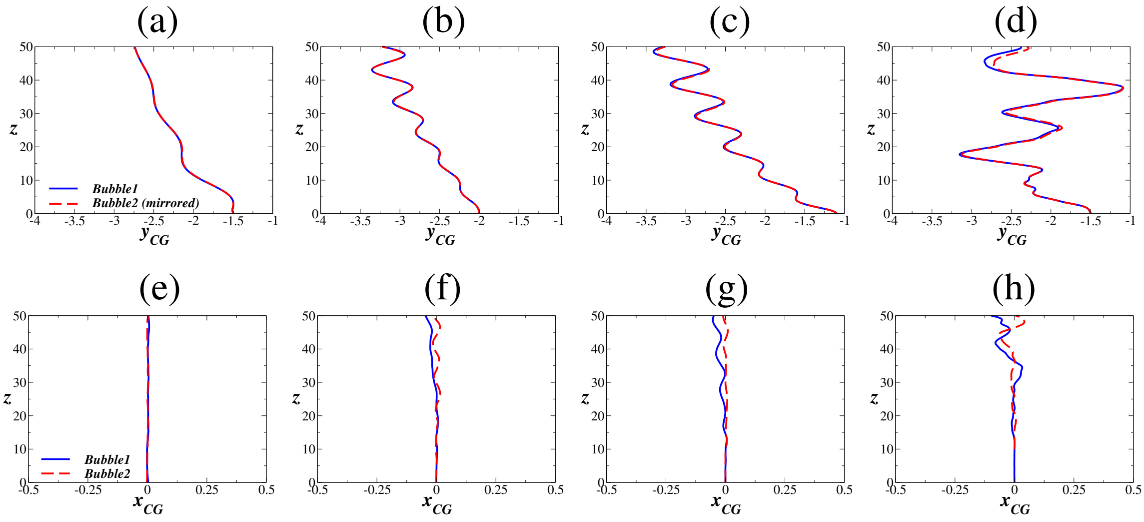

Figure 4.14: Variation of y_{CG} (top panels) and x_{CG} (bottom panels) along the vertical path of the two bubbles released side by side: (a,e) $Ga = 25$, $Eo = 1$, $q = 3$ (Point D), (b,f) $Ga = 25$, $Eo = 4$, $q = 4$ (Point F), (c,g) $Ga = 25$, $Eo = 4$, $q = 2.2$ (Point F) and (d,h) $Ga = 100$, $Eo = 2$, $q = 3$ (Point E). The position of the bubble initially placed at positive y (bubble '2') has been mirrored about the x axis in order to compare its path with that of the other bubble.

4.3 Concluding remarks

Two spherical solid objects rising through a heavier fluid in the Stokes flow regime would maintain their spacing. In particular, if the two objects are initially in the same horizontal plane, they would rise in straight vertical paths and the line separating them would be horizontal and of constant length. We ask how two identical inertial bubbles rising under gravity would respond to each other. We focus our attention on two regimes, termed regimes I and III in Tripathi *et al.* (2015*a*), in which a single bubble would display vertical rise in a straight line and oscillatory/zig-zag motion, respectively. We find that in both regimes, the vortices shed by the two bubbles interact strongly with each other, and the bubbles tend to move apart from each other as they rise. Further, the propensity to go to a spiralling or oscillatory state is increased by the presence of the second bubble. The interaction between the shed vortices organises the phase of the oscillations such that the motion of the bubbles tend to be mirror images of each other, except at significant inertia and high initial separation, where the motion is three dimensional and departures from mirror symmetry are observed particularly in the plane perpendicular to the separation vector. While the presence of the second bubble causes a drift along the separation line, it reduces the spiralling amplitude of each bubble. Increasing inertia has the effect of destabilising the steady trajectories, and chaotic motion is observed at high inertia, in a regime where a single bubble would display periodic oscillations. Interestingly however, the mirror symmetry is preserved in the chaotic regime as well, which speaks of a phase-locking in the vortex shedding of the two bubbles. A stability analysis of this flow will confirm our findings.

CHAPTER 5

Rising of an air bubble in a varying viscosity media

In this chapter, the dynamics of an air bubble rising in viscosity varying media is investigated. Two situations are considered. (i) When the bubble rises in a medium having an inherent linear viscosity variation in the vertical direction. In order to isolate the effect of viscosity stratification, the density of the surrounding medium is kept constant. This has been discussed in Section 5.1. (ii) The dynamics of an air bubble in a non-Newtonian medium. Both axisymmetric (see Section 5.2) and three-dimensional regimes (see Section 5.3) are considered. The non-Newtonian fluid is modelled as a Carreau-Yasuda shear- thinning model. Experiments are conducted using solutions of different concentrations of carboxymethyl cellulose (CMC) in deionised water. These solutions exhibit shear-thinning tendency, and are used to compare the bubble behaviour obtained from our numerical simulations.

5.1 Dynamics of an air bubble rising inside a viscosity stratified medium

The rising bubble dynamics in an unconfined quiescent viscosity-stratified medium has been numerically investigated. This is frequently encountered in industrial as well as natural phenomena. In spite of the large number of studies carried out on bubbles and drops, very few studies have examined the influence of viscosity stratification on bubble rise dynamics. To the best of our knowledge, none of them have isolated the effects of viscosity-stratification alone, even though it is known to influence the dynamics extensively, which is the main objective of this study. By conducting time-dependent simulations, we present a library of bubble shapes in the Galilei and the Eötvös numbers plane. Our results demonstrate some counter-intuitive phenomena for certain range of parameters due to the presence of viscosity stratification in the surrounding fluid. We found that in a linearly increasing viscosity medium, for certain values of parameters, bubble undergoes large deformation by forming an elongated skirt, while the skirt tends to physically separate the wake region from the rest of the surrounding fluid. This peculiar dynamics is attributed to the migration of less viscous fluid that is carried in the wake of the bubble as it rises, and thereby creating an increasingly larger viscosity contrast between the fluid occupied in the wake region and the surrounding fluid, unlike that observed in a constant viscosity medium. It is also observed that the effect of viscosity stratification is qualitatively different for different regimes of the dimensionless parameters.

5.1.1 Formulation

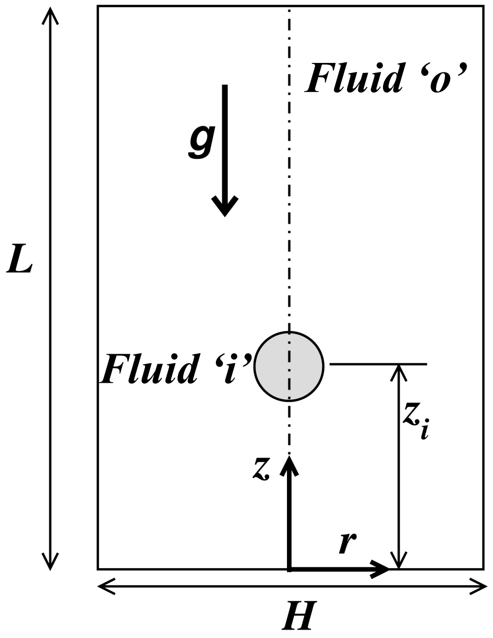

Figure 5.1: Schematic diagram showing the initial configuration of a bubble (fluid 'i') rising inside a viscosity stratified medium (fluid 'o') under the action of gravity, which is acting in the negative z direction. Initially the bubble is located at $z = z_i = 4R$; R being the radius of the bubble. The viscosity of the surrounding fluid 'A' is linearly increasing along the vertical direction, z.

The dynamics of an axisymmetric air bubble (designated by fluid 'i') of initial radius R, having constant viscosity μ_i rising under the action of buoyancy inside an unbounded domain consisting of another fluid (designated by fluid 'o') is investigated. The schematic diagram of this system is shown in Fig. 5.1. Both the fluids are considered to be incompressible and Newtonian. The viscosity and density of fluids 'i' and 'o' are μ_i, ρ_i and μ_o, ρ_o, respectively. The cylindrical coordinates (r, z) is used to model the rising bubble dynamics starting from a position $z_i = 4R$ at time, $t = 0$ in quiescent liquid. Here, r and z are the radial and vertical coordinates, respectively. The viscosity field of fluid 'o', μ_o is initialized as $\mu_o = \mu_{ref}(a_1 + a_2 z)$, μ_{ref} being the viscosity of fluid 'o' at $z = z_i$, and a_1, a_2 are constants, which are defined below. The flow dynamics is assumed to be symmetrical about $r = 0$, and the acceleration due to gravity, g is acting in the negative z direction, as shown in Fig. 5.1.

Note that the scaling used to non-dimensionalised the variables is different from that given for general description in Chapter 2. Unlike in Chapter 2, in this section only, the viscosity and density of the inner fluid (air phase) is used as the viscosity and density scales, respectively. This is due to the fact the viscosity of the outer fluid is not constant. However, the velocity scale, $V \equiv \sqrt{gR}$, is the same as that used in Chapter 2. Thus, the following scaling is employed in order to render the governing equations dimensionless:

$$(r,z) = R\left(\widetilde{r},\widetilde{z}\right), \; t = \frac{R}{V}\widetilde{t}, \; (u,v) = V(\widetilde{u},\widetilde{v}), \; p = \rho_i V^2 \widetilde{p}, \; \mu = \widetilde{\mu}\mu_i, \; \rho = \widetilde{\rho}\rho_i. \tag{5.1}$$

After dropping tildes from all nondimensional terms, the governing dimensionless equations are given by

$$\nabla \cdot \mathbf{u} = 0, \tag{5.2}$$

$$\rho\left[\frac{\partial \mathbf{u}}{\partial t} + \mathbf{u}\cdot\nabla\mathbf{u}\right] = -\nabla p + \frac{1}{Ga}\nabla\cdot\left[\mu(\nabla\mathbf{u} + \nabla\mathbf{u}^T)\right] + \frac{\delta}{Eo}\hat{n}\nabla\cdot\hat{n} - \rho\vec{e}_z, \tag{5.3}$$

$$\frac{\partial c}{\partial t} + \mathbf{u}\cdot\nabla c = 0, \tag{5.4}$$

$$\frac{\partial \mu}{\partial t} + \mathbf{u}\cdot\nabla\mu = 0, \tag{5.5}$$

where $\mathbf{u}(u,v)$ represents axisymmetric velocity field, wherein u and v are the velocity components in the radial and vertical directions, respectively; p denotes the pressure field; c is the volume fraction of the fluid 'o', whose values are 0 and 1 for the air and liquid phases, respectively; μ is the viscosity field which is advected with the local velocity of the fluid; δ is the Dirac delta function; $\kappa = \nabla\cdot\mathbf{n}$ is the curvature, $\mathbf{n}$ is the unit normal to the interface pointing towards fluid 'o', $\vec{e}_z$ represents the unit vector in the vertically upward direction, and σ is the interfacial tension coefficient of the liquid-gas interface. Here, $Ga(\equiv \rho_i VR/\mu_i)$ and $Eo(\equiv \rho_i gR^2/\sigma)$ denote the Galilei number and Eötvös number, respectively.

The dimensionless density ρ is given by:

$$\rho = (1-c) + \rho_r c, \tag{5.6}$$

and the initial viscosity field is given by:

$$\mu = (1-c) + \mu_{r0}(a_1 + a_2 z)c, \tag{5.7}$$

where $\mu_{r0} \equiv \mu_{ref}/\mu_i$ and $\rho_r \equiv \rho_o/\rho_i$. Note that by setting $a_1 = 1$ and $a_2 = 0$ one could recover a system with constant viscosity of the surrounding fluid.

The boundary conditions used for this study are the symmetrical at $r = 0$ and the Neumann boundary conditions for the velocity components at the rest of the boundaries of the computational domain. The pressure is Neumann in all the boundaries.

5.1.2 Results and discussion

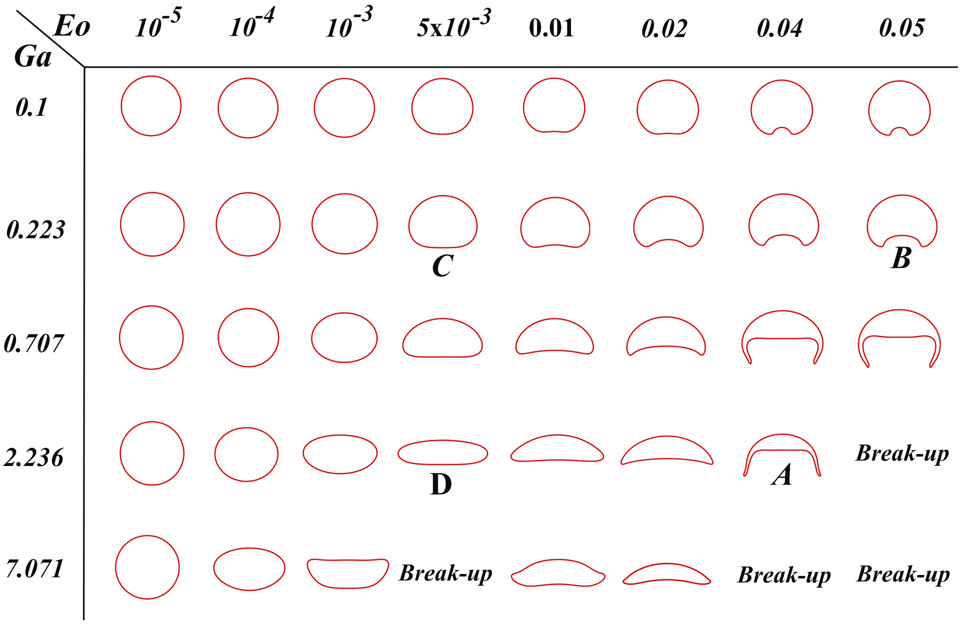

Figure 5.2: The terminal shapes of the bubble obtained from the present simulations in $Ga - Eo$ space for the constant viscosity case ($a_1 = 1, a_2 = 0$). The rest of the parameter values are $\rho_r = 10^3$, $\mu_{r0} = 10^2$.

We begin the presentation of our results in Fig. 5.2 by plotting the terminal shapes of the bubble for the constant viscosity case ($a_1 = 1, a_2 = 0$) obtained from our time-dependent simulations in $Ga - Eo$ space. Below, this is referred to as the "base case". A similar plot based on the steady state calculations was presented by Tsamopoulos *et al.* (2008*b*). Note that in their study, the viscosity and density of the surrounding fluid were used as the characteristic scales to nondimensionalize the governing equations, hence a suitable conversion is applied to get our dimensionless variables. We found that for low Ga and low Eo the shapes of the bubble presented in Fig. 5.2 are qualitatively similar to those obtained by Tsamopoulos *et al.* (2008*b*). However, the shapes of the bubble are different for larger values of Eo and Ga. This discrepancy can be attributed to the steady state assumption considered in their study. We also found that the bubble undergoes topological changes and the bubble dynamics remain unsteady for few sets of Ga and Eo (designated by "break-up" in Fig. 5.2). The time evolution of shapes of the bubble for one typical "break-up" case ($Ga = 7.071$ and $Eo = 0.05$) is shown in Fig. 5.3. It can be seen in this figure that bubble has a different topology for $t > 2$ for this set of parameters. Note that Tsamopoulos *et al.* (2008*b*) also did not find a steady state solution for cases designated by "break-up".

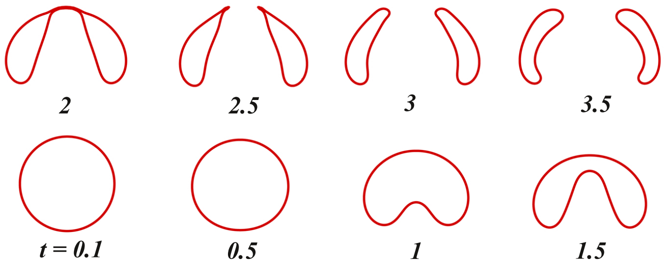

Figure 5.3: Time evolution of the shapes of the bubble obtained for a typical "break-up" case ($Ga = 7.071$ and $Eo = 0.05$). The rest of the parameter values are the same as those used to generate Fig. 5.2. The dimensionless time is written at the bottom of each bubbles.

The effect of viscosity stratification of the surrounding fluid (for a system where the viscosity increases with increasing z) on the bubble dynamics is investigated next. The viscosity of the surrounding fluid (at rest, $t = 0$) is given by:

$$\mu_o = \mu_{r0}(a_1 + a_2 z), \tag{5.8}$$

where values of the constants a_1 and a_2 are fixed at 0.2.

The bubble rise dynamics of four typical sets of (Ga, Eo) designated by points A, B, C and D in Fig. 5.2, which correspond to $(Ga, Eo) = (2.236, 0.04), (0.223, 0.05), (0.223, 0.005)$, and $(2.236, 0.05)$, respectively, are investigated below. The behaviour of the rest of the bubbles in Fig 5.2 can be extrapolated from these four typical cases analyzed below.

Linearly increasing viscosity, $\mu_o = \mu_{r0}(a_1 + a_2 z)$

Point A: $Ga = 2.236, Eo = 0.04$

The temporal evaluation of bubble shapes for $Ga = 2.236, Eo = 0.04$ are shown in Fig. 5.4. The shapes of the bubble in linearly increasing viscosity medium (shown in Fig. 5.4(b)) are compared with those of constant viscosity case (shown in Fig. 5.4(a)) at different times. It can be seen that for the case of the linearly increasing viscosity medium an elongated skirt (longer than that appears for the constant viscosity case (Fig. 5.4a)) is formed leading to a single recirculation region (as shown in Fig. 5.5 (b)). This is counter intuitive due to the fact that as the

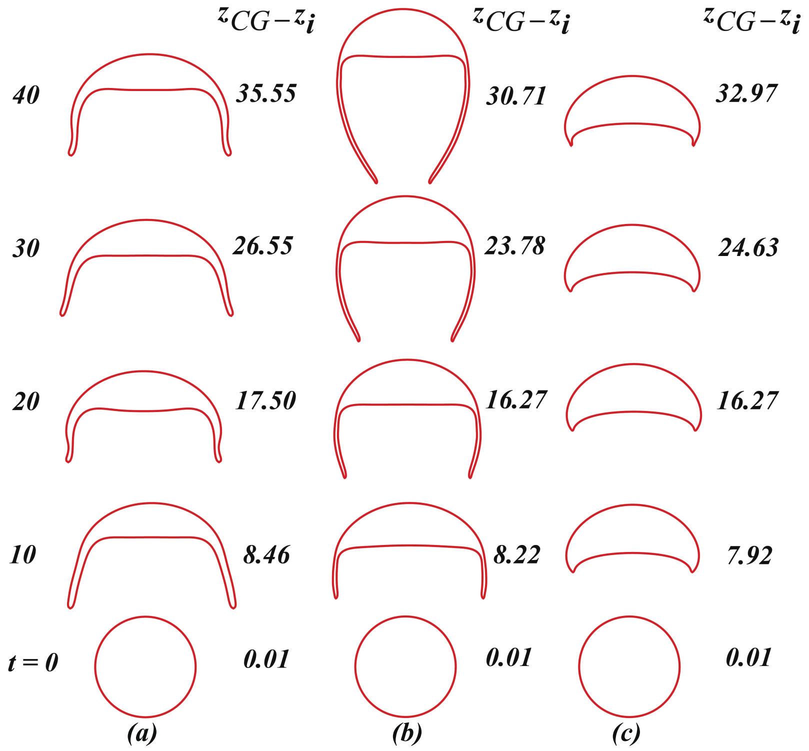

Figure 5.4: Time evolution of bubble shapes for $Ga = 2.236, Eo = 0.04$: (a) constant viscosity system ($a_1 = 1, a_2 = 0$), (b) linearly increasing viscosity ($a_1 = 0.2, a_2 = 0.2$), (c) constant viscosity case in which μ_{r0} is set to the average viscosity of the linearly increasing viscosity system (panel (b)) for the distance traversed by the center of gravity of the bubble (μ_{avg}).

bubble rises in the vertical direction the local viscosity increases, which in turn decreases the local Ga. It has been observed that at lower Ga the bubble tends to take a dimpled ellipsoidal shape instead of forming skirt (see for instance, the bubble shapes for $Eo = 0.04$ in Fig. 5.2). As the bubble rises in the upward direction, the less viscosity fluid from the bottom part of the domain advects along with the recirculation region. Thus the viscosity contrast between inside and outside regions separated by the skirt continues to increase with the ascent of the bubble. The stresses generated due to the differential viscosity on both sides of the skirt forces it to curl inwards. This deformation of the skirt leads to a physical separation of the two regions with high viscosity contrast by means of the air film contained in the skirt of the bubble. This separation of fluids allows fast recirculation to occur in the fluid captured inside the wake of the bubble, while simultaneously allowing a slow flow outside of the skirt, thus creating a contrast in Reynolds number as well. This may be beneficial to certain processes where a low viscosity fluid is required to be carried through a highly viscous fluid with the help of a carrier bubble.

In order to investigate whether this dynamics is due to our viscosity scale, we re-examine how the results reflect our choice of viscosity scale. In Fig. 5.4(c), the evolution of shapes of

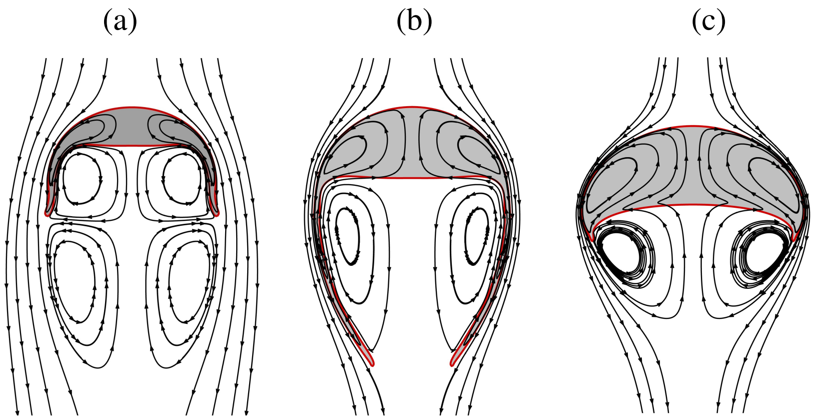

Figure 5.5: Comparison of the streamlines at $t = 40$ for (a) constant viscosity system ($a_1 = 1, a_2 = 0$), (b) linearly increasing viscosity ($a_1 = 0.2, a_2 = 0.2$), (c) constant viscosity case in which μ_{r0} is set to the average viscosity of the linearly increasing viscosity system (panel (b)) for the distance traversed by the center of gravity of the bubble (μ_{avg}). The rest of the parameter values the same as those used to generate Fig. 5.4.

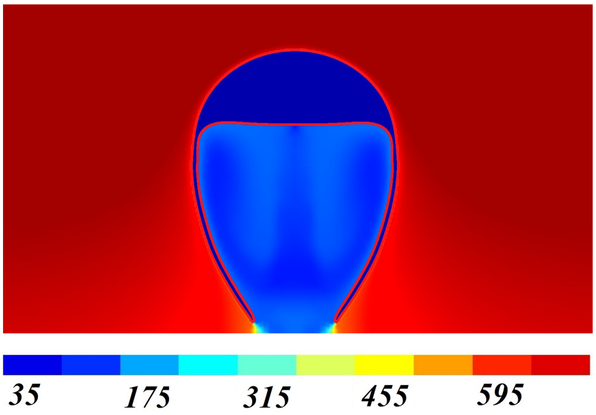

Figure 5.6: Viscosity contours for the linearly increasing viscosity case at $t = 40$. The rest of the parameter values are the same as those used to generate Fig. 5.4(b).

the bubble are plotted for constant outer fluid viscosity equal to the average of the lowest (i.e. μ_o at $z = 0$) and highest (i.e. μ_o at $z = 30.71$) viscosity values, i.e. the average viscosity of the linearly increasing viscosity system (Fig. 5.4(b)) for the distance traversed by the center of gravity of the bubble (μ_{avg}). As there is no ideal viscosity scale, we have made this simplest choice possible. It can be seen in Fig. 5.4 (c) that the skirt formation delays significantly (starts at $t \approx 32$) as compared to the cases presented in Fig. 5.4 (a) and (b). It is surprising that the bubble rise velocity in Fig. 5.4 (c) is almost the same as those of the cases presented in Fig. 5.4 (a) and (b), suggesting that the wake viscosity plays an important role in skirt formation and the deformation of the bubble. The viscosity distribution for the linearly increasing viscosity case at later time, $t = 40$ (shown in Fig. 5.6) reveals that as the bubble rises it carries the low viscosity fluid from the bottom part of the domain in its wake region. Thus it can be deduced from Fig. 5.4 (a) and (b) that the stresses inside the wake affect the formation of skirt the most, which can be expressed as the local Ga and Eo inside the skirt. This is confirmed by the fact that Fig. 5.4(c) forms skirt at later times since the local Ga in the wake is not favourable (lesser than the corresponding value of Ga in Fig. 5.4(a) and (b)) to form skirt.

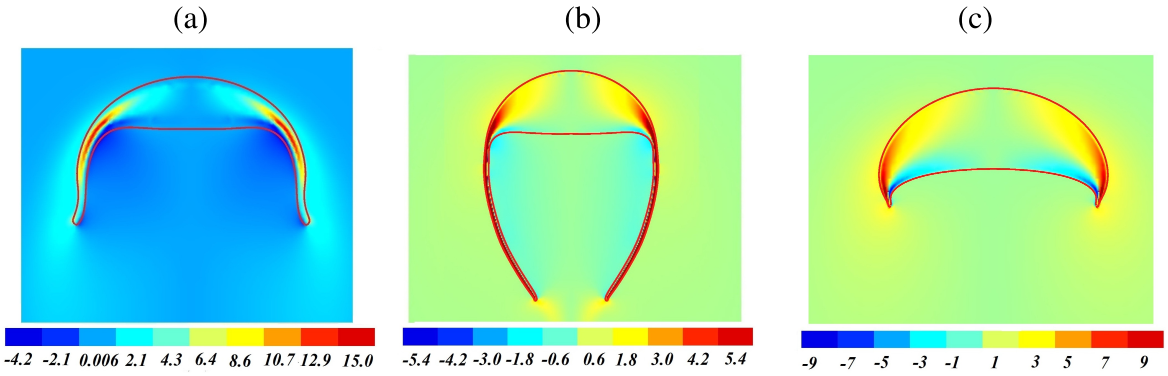

Figure 5.7: Vorticity magnitude at $t = 40$ for (a) constant viscosity system ($a_1 = 1, a_2 = 0$), (b) linearly increasing viscosity case ($a_1 = 0.2, a_2 = 0.2$), (c) constant viscosity case in which μ_{r0} is set to the average viscosity of the linearly increasing viscosity system (panel (b)) for the distance traversed by the center of gravity of the bubble (μ_{avg}). The rest of the parameter values are the same as those used to generate Fig. 5.4.

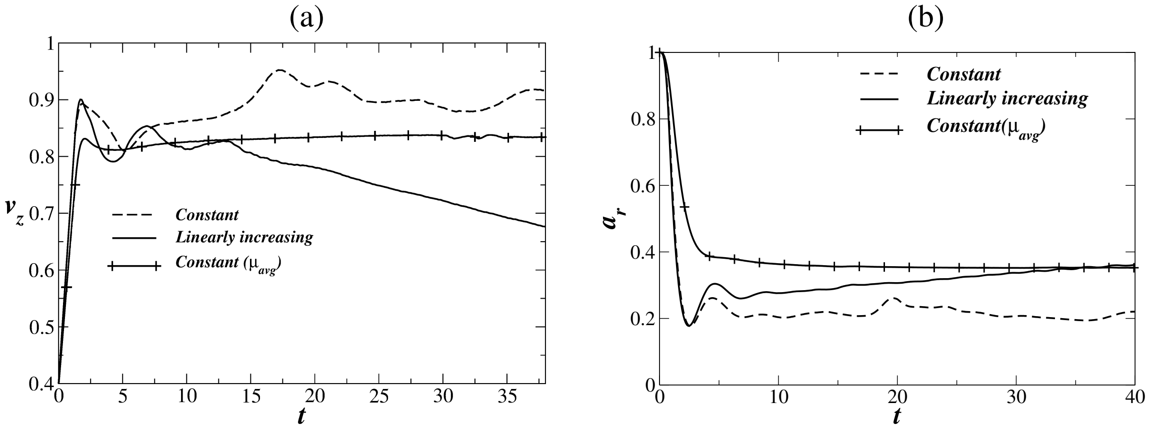

Figure 5.8: Variation of the (a) rise velocity (v_z) and (b) aspect ratio ($a_r = h/w$) of the bubble with time. Here h and w represents the height and width of the bubble. The rest of the parameter values are the same as those used to generate Fig. 5.4.

In Fig. 5.5, the streamlines in the reference frame moving with the same velocity as that of the tip of the bubble at $t = 40$ are plotted for the same parameter values as those used to generate Fig. 5.4. It is also noted here that the wake structures of the constant viscosity and linearly increasing viscosity cases are very different from each other, as shown in Fig. 5.5. For the constant viscosity system ($a_1 = 1, a_2 = 0$) with $\mu_{r0} = 100$ (Fig 5.5 (a)), it can be seen

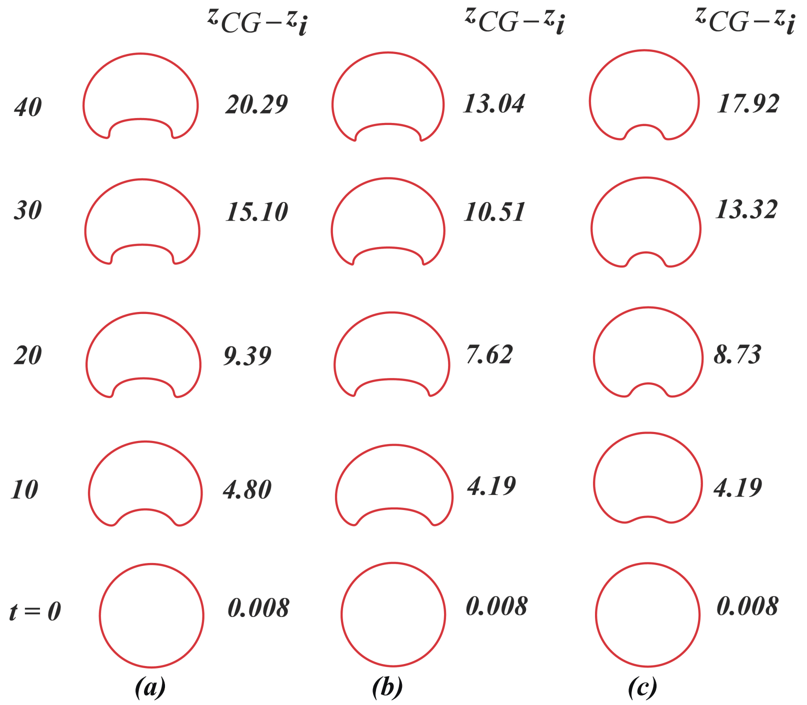

Figure 5.9: Time evolution of bubble shapes for $Ga = 0.223, Eo = 0.05$: (a) constant viscosity system (base case), ($a_1 = 1, a_2 = 0$), (b) linearly increasing viscosity case ($a_1 = 0.2, a_2 = 0.2$), (c) constant viscosity case in which μ_{r0} is set to the average viscosity of the linearly increasing viscosity system (panel (b)) for the distance traversed by the center of gravity of the bubble (μ_{avg}).

that there are two recirculation zones in the wake region of the bubble, whereas, the bubble in linearly increasing viscosity medium (Fig. 5.5 (b)) shows only one recirculation zone in its wake region which is enclosed by the skirt. The two recirculation zones in the wake of the bubble corresponding to Fig. 5.5 (a) prevent the skirt from closing in on itself, and depending on the strength of circulation in the two zones, the skirt may develop travelling waves on the skirt which is termed as wavy skirt (Bhaga & Weber, 1981). Close inspection of Fig 5.5 (c) reveals that the streamlines cross the air-liquid interface in the wake region, which implies that the shape is far from steady and the skirt may become longer at later times. It can also be inferred from the streamline patterns of Fig 5.5 (c) that there must be two toroidal recirculation zones inside the bubble of which only one can be seen by choosing the frame of reference moving with the tip of the bubble. There must be a counter-rotating vortex inside the bubble in order to satisfy the continuity of stress and velocity components inside the bubble between the two co-rotating vortices which are shown in this figure. Inspection of contours of vorticity magnitude plotted in Fig. 5.7 reveals that the maximum vorticity always lies inside the bubble. A similar finding was also observed by Tripathi *et al.* (2014).

The temporal variations of rise velocity (v_z) and aspect ratio ($a_r = h/w$) of the bubble

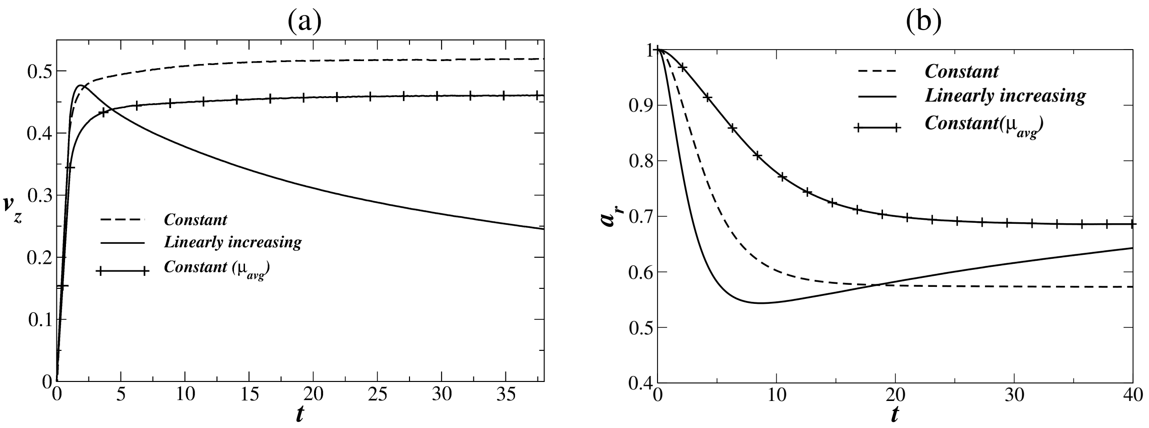

Figure 5.10: Variation of velocity of the center of gravity and aspect ratio of the bubble with time. The rest of the parameter values are the same as those used to generate Fig. 5.9.

for all the cases considered in Fig. 5.4 are shown in Fig. 5.8(a) and (b), respectively. Fig. 5.8(a) shows an expected behaviour; the bubbles for constant viscosity cases attain a terminal velocity. However, the bubble in linearly increasing viscosity medium (shown in Fig. 5.4(b)) keeps decelerating, with a peak at an early time (approximately at $t = 2$). The peak may be attributed to the initial acceleration due to buoyancy, and the gradual decay in the rise velocity is due to the viscous forces overcoming the gravitational forces at later times. This is evident from the ratio of the viscous and the gravitational time scales ($\sqrt{R/g}/(\rho R^2/\mu)$), which is the Galilei number. It can be seen in Fig. 5.8 (a) that the viscous force overcomes the gravitational force (when the rise velocity reaches a maximum) at $t \approx 2$ which approximately matches with the value of Galilei number considered. In Fig. 5.8(b), it can be seen that the bubble reaches to a terminal oblate shape for constant viscosity cases. The aspect ratio of the bubble when the outer fluid viscosity is $\mu_{r0} = \mu_{avg}$ is higher than that when $\mu_{r0} = 100$ (base case). In case of linearly increasing viscosity system the bubble becomes oblate by decreasing the value of a_r to approximately 0.2, which subsequently increases gradually with time.

Point B: $Ga = 0.223, Eo = 0.05$

Next in Fig. 5.9, we investigate the dynamics associated with the bubble marked as point ‘B’ in Fig. 5.2 ($Ga = 0.223, Eo = 0.05$). In this case, Eo is slightly higher, but Ga is ten times lower than the value used for the bubble designated by point ‘A’ (discussed above). It can be seen in Fig. 5.9 that the shapes of the bubble at different times for linearly increasing viscosity medium (Fig. 5.9(b)) and constant viscosity system ($a_1 = 1, a_2 = 0$) (Fig. 5.9(a)) are similar. However, these are qualitatively different from the shapes exhibited by bubble shown in Fig. 5.9(c). This result also suggests that the bubble dynamics is predominantly

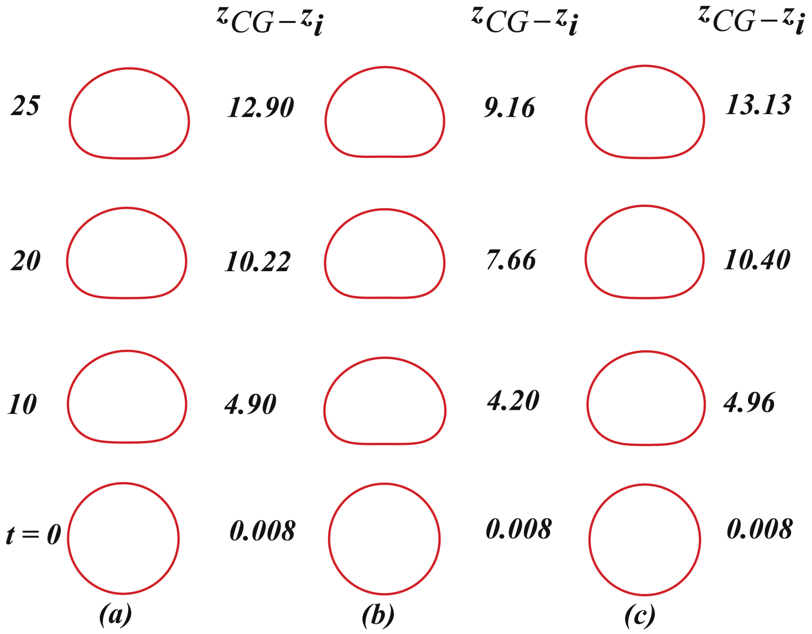

Figure 5.11: Time evolution of bubble shapes for $Ga = 0.223, Eo = 0.005$: (a) constant viscosity system ($a_1 = 1, a_2 = 0$), (b) linearly increasing viscosity case ($a_1 = 0.2, a_2 = 0.2$), (c) constant viscosity case in which μ_{r0} is set to the average viscosity of the linearly increasing viscosity system (panel (b)) for the distance traversed by the center of gravity of the bubble (μ_{avg}).

dominated by the wake region of the bubble. Inspection of this figure also reveals that the cross section of the bubbles in panels (a) and (b) is elliptical, but in panel (c) it is more or less semicircular. The variation of center of gravity and aspect ratio of the bubbles presented in Fig. 5.9 are shown in Fig. 5.10(a) and (b), respectively. It can be seen that the bubbles for constant viscosity cases (Fig. 5.9(a) and (c)) attain terminal shape and velocity. However, the bubble in linearly increasing viscosity medium (shown in Fig. 5.9(b)) decelerates, with a peak at an early time. The early accelerating phase is driven by the initial acceleration due to buoyancy. In Fig. 5.10(b), it can be seen that the aspect ratio of the bubble inside a linearly increasing viscosity medium decreases (approximately to $a_r = 0.55$) and it assumes an oblate shape, after which the bubble has a tendency to go towards the original shape. It is to be noted that the bubble for this case has not reached a steady state, and expected to deform continuously with time.

Point C: $Ga = 0.223, Eo = 5 \times 10^{-3}$

In Fig. 5.11, the shapes of the bubble for $Ga = 0.223, Eo = 5 \times 10^{-3}$ are plotted. It is to be noted here that both Ga and Eo are small. In this case the surface tension dominates the dynamics; the shapes of the bubble become slightly oblate after reaching an apparent steady

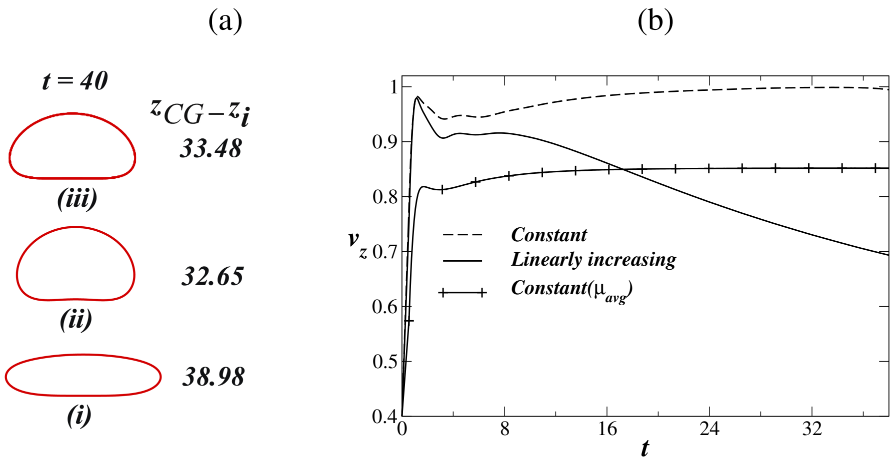

Figure 5.12: (a) Terminal shape of the bubbles: (i) constant viscosity system ($a_1 = 1, a_2 = 0$), (ii) linearly increasing viscosity case ($a_1 = 0.2, a_2 = 0.2$), (iii) constant viscosity case in which μ_{r0} is set to the average viscosity of the linearly increasing viscosity system (panel (ii)) for the distance traversed by the center of gravity of the bubble (μ_{avg}). (b) Variation of velocity of the center of gravity of the bubble with time. The rest of the parameter values are $Ga = 2.236, Eo = 5 \times 10^{-3}$.

state at very early time (for $t > 10$). However, it can be seen that as the Ga considered in this case is very low, the velocity of the bubbles for constant viscosity cases (panels a and c) are nearly the same. However, in case of linearly increasing viscosity medium (panel b) the velocity of the bubble decreases as the local Ga decreases further due to the increase in local viscosity as the bubble moves in the upward direction.

Point D: $Ga = 2.236, Eo = 5 \times 10^{-3}$

The terminal shapes of the bubbles for $Ga = 2.236, Eo = 5 \times 10^{-3}$ corresponding to the case ‘D’ in Fig. 5.2 are shown in Fig. 5.12(a). It can be seen that the shapes of the bubbles for the linearly increasing viscosity medium (shown in sub-panel ii of Fig. 5.12(a)) and constant viscosity case when μ_{r0} is set to μ_{avg} (sub-panel iii of Fig. 5.12(a)) are almost similar (oblate shape). However, the dimple of the bubble in case of the linearly increasing viscosity medium (sub-panel ii of Fig. 5.12(a)) is not visible in sub-panel iii of the same figure. It can also be seen in sub-panel (i) that the bubble takes a disk like shape for the base case ($a_1 = 1, a_2 = 0$). The velocity of the centre of gravity versus time plot (Fig. 5.12(b)) confirms the above-mentioned conclusion. Inspection of this figure also reveals that the bubble in linearly increasing viscosity medium decelerates after the accelerating phase observed during the early time.

5.1.3 Concluding remarks

Here, we have examined the axisymmetric dynamics of bubble rise in an unconfined viscosity stratified medium. In spite of the large number of studies carried out on bubbles and drops, very few studies have examined the influence of viscosity stratification (to the best of our knowledge none of them isolate the effects of viscosity-stratification) on the bubble rise dynamics. We have presented a library of bubble shapes in the Galilei and the Eötvös numbers plane. The present results (terminal shapes of the bubbles) agree well with those obtained by Tsamopoulos *et al.* (2008*b*) for low Ga and low Eo. The shapes of the bubbles are qualitatively different for higher values of Ga and Eo. This difference may be attributed to the steady state calculations conducted in their study. Our results demonstrate a counter-intuitive phenomenon that the bubble undergoes extensive deformation by forming elongated skirt for linearly increasing viscosity medium for certain sets of parameter values. This is due to the migration of less viscous fluid, which is trapped inside the wake region bounded by the skirt of the bubble. This dynamics is very different from that observed in constant viscosity medium. We found that for lower values of Eo and Ga, although the bubble moves slowly in case of the linearly increasing viscosity medium, the shapes look very similar to those observed in constant viscosity medium. In future, it will be interesting to investigate this phenomenon in three-dimensions and by conducting experiments.

5.2 An air bubble rising in a non-Newtonian liquid in the axisymmetric regime

This section presents the numerical study of the dynamics of an air bubble rising in a non-Newtonian fluid (shear thinning/thickening) in the axisymmetric regime. The governing equations consist of mass and momentum conservation, coupled to an equation for the volume fraction of the non-Newtonian fluid, which is modelled using the Carreau-Yasuda model. This study is motivated from Tripathi *et al.* (2015*a*) who investigated the dynamics of a rising bubble in a quiescent Newtonian fluid under the action of buoyancy by conducting three-dimensional simulations. As discussed in Chapter 1, they had identified five different regimes of starkly distinct behaviours (namely, axisymmetric, skirted, zigzagging/spiralling, peripheral break-up and central breakup regions) in the Galilei, Ga and Eötvös, Eo numbers plane. We specifically focus on a bubble in the low Ga and low Eo region but for a non-Newtonian surrounding fluid, where for a similar region on the Ga and Eo plane, Tripathi *et al.* (2015*a*) had shown that for a Newtonian fluid, the bubble maintains azimuthal symmetry. A parametric study is conducted by varying the shear-thinning/thickening tendency of the surrounding fluid for different Galilei and Eötvös numbers in this region. As compared to a Newtonian fluid, it is found that increasing the shear thinning tendency increases the rise velocity, and reduces the deformations of the bubble. The deformation of the bubble is enhanced for higher Ga and low Eo.

5.2.1 Formulation

The dynamics of a rising air bubble (Newtonian fluid 'i') in a non-Newtonian medium (fluid 'o') under the action of buoyancy within a confined cylindrical domain of diameter $H(= 20R)$ and height $L(= 90R)$, as shown in Fig. 5.13, is considered. As shown by Tripathi *et al.* (2015*a*), the parameters considered in this study (high surface tension and low inertia) allow us to assume that the dynamics is axisymmetric. Thus a cylindrical coordinate system, (r, z), is used to model the flow dynamics, in which r and z denote the radial and axial coordinates, respectively. Gravity acts in the negative z direction. The bubble is initially present at a distance $z_i = 5R$ above the bottom of the domain located at $z = 0$. The boundary conditions used for this study are as follows: Symmetrical at $r = 0$ and the Neumann boundary conditions for the velocity components at the rest of the boundaries of the computational domain. Neumann boundary condition is applied for pressure in all the boundaries.

The governing equations and the solution methods are similar to the one discussed in Chap-

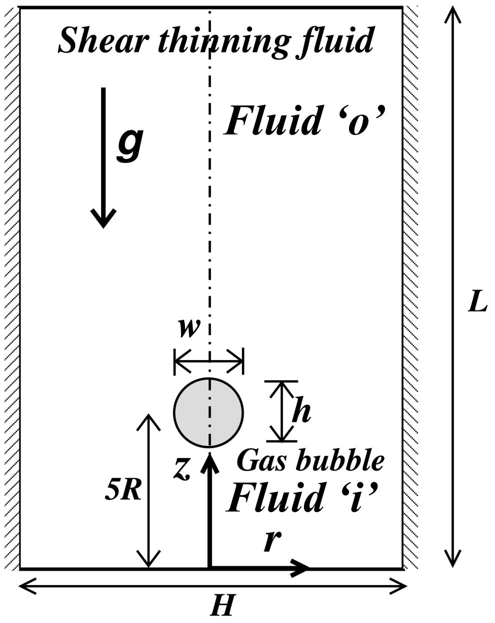

Figure 5.13: Schematic diagram (not to scale) showing the initial configuration of an air bubble (designated as fluid 'B') rising inside a shear-thinning fluid (designated as fluid 'A') under the action of gravity, which is acting in the negative z direction. Initially the bubble is located at $z = z_i = 5R$; R being the radius of the bubble. The diameter (H) and height (L) of the cylindrical computational domain are $20R$ and $90R$, respectively. Initially, the aspect ratio, $h/w = 1$. The origin and the r and z axes are as shown.

ter 2. However, it should be noted here that while the dynamic viscosity of the air phase, μ_i is considered to be constant, the viscosity of fluid 'o', μ_o varies with shear rate as the fluid is non-Newtonian. The viscosity μ_o is given by the Carreau-Yasuda model (Zhang *et al.*, 2010)

$$\mu_o = \mu_{ref}\left[1 + (\lambda\Pi)^2\right]^{(n-1)/2}. \tag{5.9}$$

This simplified rheological model (Eq. (5.9)) is derived from the general form (Bird *et al.*, 1987)

$$\mu_i = \mu_\infty + (\mu_0 - \mu_\infty)\left[1 + (\lambda\Pi)^\beta\right]^{(n-1)/\beta}, \tag{5.10}$$

where μ_∞ is the dynamic viscosity corresponding to the infinite shear rate; β is the parameter describing the transition region between the zero shear rate and power-law regions. The simplified viscosity model (Eq. (5.9)) is obtained by setting $\beta = 2$ and $\mu_\infty = 0$ in Eq. (5.10). Here, λ is the inelastic time constant, n is the flow index, μ_{ref} represents the dynamic viscosity corresponding to the zero shear rate, and $\Pi = \left(E_{ij}E_{ij}\right)^{1/2}$ is the second invariant of the strain rate tensor, wherein $E_{ij} \equiv \frac{1}{2}\left(\partial u_i/\partial x_j + \partial u_j/\partial x_i\right)$. Zhang *et al.* (2010) found that for CMC solutions, the value of λ lies in the range of 0.2 s to 0.5 s. The various dimensionless numbers characterising the flow are Galilei number, $Ga(\equiv \rho_o g^{1/2}R^{3/2}/\mu_{ref})$ and Eötvös number, $Eo(\equiv \rho_o g R^2/\sigma)$. Also, $\mu_r(\equiv \mu_i/\mu_{ref})$ represents the ratio of the dynamic viscosities of fluid 'i' and fluid 'o' at zero shear rate. In this study, the densities of fluid 'i' and fluid 'o' are assumed to be constant, such that the density ratio $\rho_r (\equiv \rho_i/\rho_o)$ is 10^{-3}.

Thus the dimensionless density and dynamic viscosity are given by

$$\rho = c + (1 - c)\rho_r, \tag{5.11}$$

and

$$\mu = c\left[1 + (\lambda\Pi)^2\right]^{(n-1)/2} + (1 - c)\mu_r, \tag{5.12}$$

respectively. For a typical air bubble of radius 1 *cm* rising in a CMC solution, the value of dimensionless λ ranges from 6.2 to 15.6 (calculated based on Eq. (5.1)). Therefore, a representative value, $\lambda = 10$ is used throughout this study.

As discussed in Chapter 2, several validation exercises are performed to validate the numerical solver used in this study. In addition, in Fig. 5.14, we perform a grid convergence test by plotting the variation of the location of center of gravity (z_{CG}), and the aspect ratio (defined as h/w) of the bubble with respect to time for a typical set of parameters ($Ga = 10$, $Eo = 10$, $\mu_r = 10^{-2}$, $\rho_r = 10^{-3}$, $\lambda = 10$ and $n = 0.5$). Three computational grids whose smallest grid-sizes are 0.0195 (grid 1), 0.0097 (grid 2), and 0.0049 (grid 3) are considered. The slope of z_{CG} versus time (Fig. 5.14(a)) at later times gives the terminal velocity of the bubble. We found that the values of the terminal velocity of the bubbles are 0.997, 0.985 and 0.981 for grid 1, grid 2 and grid 3, respectively. Thus, the maximum error between the results obtained using grid 2 and grid 3 is 0.4 % for this set of parameter values. It can be seen from Fig. 5.14 that the results are indistinguishable for all three grid sizes. A similar conclusion can also be obtained from Fig. 5.15, where the shape of the bubble and the viscosity contours are plotted for these three grids. We also found that decreasing the value of H does not change the results; we have checked this for $H = 10$, 6 and 3. For the rest of the study, we chose grid 2, having the smallest grid size of 0.0097 for generating the results. The maximum time step used for this grid is 0.003. The temporal discretisation used in the present study is also second-order accurate.

After establishing the validity of our solver and subsequently performing a grid convergence study, we have validated our solver specifically for simulation of bubbles rising in non-Newtonian fluids. This has been done by comparing the terminal velocity obtained from the present simulations with the experimental and numerical results of Zhang *et al.* (2010). The comparisons are shown in Table 1 for two solutions of sodium aqueous carboxymethyl cellulose (CMC) which were used by them. The properties of these solutions and diameters of the bubble are given in this table. The corresponding dimensionless numbers (e.g. Ga, Eo, ρ_r and

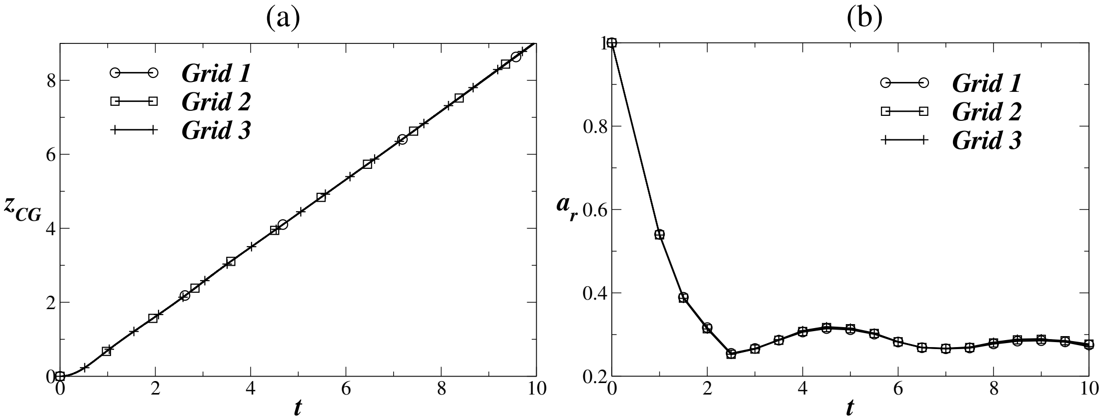

Figure 5.14: The variation of center of gravity, z_{CG} and aspect ratio ($a_r = h/w$) of the bubble for different grids: The smallest grid size in grid 1, grid 2 and grid 3 are 0.0195, 0.0097, and 0.0049, respectively. The rest of the parameter values are $Ga = 10$, $Eo = 10$, $\mu_r = 10^{-2}$, $\rho_r = 10^{-3}$, $\lambda = 10$ and $n = 0.5$.

μ_r) based on the current formulation are calculated for our simulations. It can be seen from table I that the terminal velocities of the bubble rising inside these solutions using our simulations are in good agreement with the experimental and numerical results of Zhang *et al.* (2010). The percentage of errors calculated using $\left(\frac{U_T(exp)-U_T(present)}{U_T(exp)} \times 100\right)$ for both the cases considered are less than 1.5 %.

Table 5.1: Comparison of the terminal velocities obtained by Zhang *et al.* (2010) and the present work for two solutions of sodium aqueous carboxymethyl cellulose (CMS). The terminal velocities obtained from their experiment and simulation are non-dimensionalized by $\sqrt{gR}$. The dimensionless values of λ for each solution are calculated for a typical bubble of radius 1 *cm*. Here $\rho_r = 1.2\times10^{-3}$ and $\mu_r = 4.8\times10^{-4}$. The values obtained from their work are taken from tables 2 and 3 of Zhang *et al.* (2010).

Liquids	diameter (in mm)	$U_{T,exp}$ Zhang *et al.*	$U_{T,cal}$ Zhang *et al.*	μ_{ref} (Pas)	λ (s)	n	Ga	Eo	U_T
CMC1	4.19	1.44	1.48	0.0377	0.512	0.89	8.04	0.61	1.42
CMC2	3.96	0.66	0.7	0.122	0.207	0.9	2.28	0.544	0.658

5.2.2 Results and discussion

Figs. 5.16(a) and (b) show plots of the variation of the center of gravity and the aspect ratio (defined as h/w), respectively, of a bubble rising in a shear thinning fluid ($n = 0.8$) with respect to time for different values of Eo. For a skirted bubble, h is the distance from the tip of the bubble to the bottom of the skirt. The rest of the parameter values are $Ga = 10$, $\lambda = 10$, $\mu_r = 10^{-2}$ and $\rho_r = 10^{-3}$. For comparison, Figs. 5.16(a) and (b) also show the results for an air

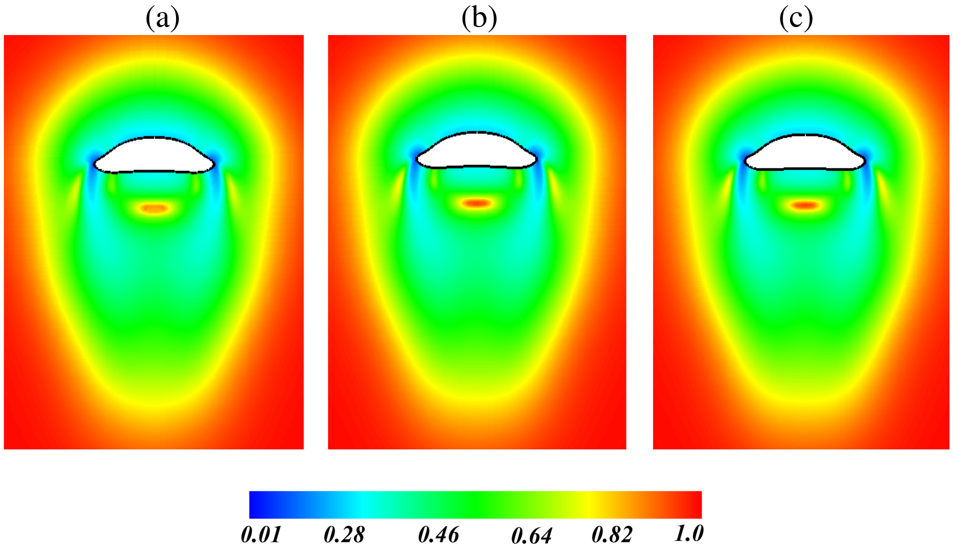

Figure 5.15: The contours of viscosity are plotted along with the shapes of the bubble for three different grid sizes at $t = 10$. The parameters and the grid sizes used are the same as those used in Fig. 5.14. The background color contours represent the viscosity variation.

bubble rising in a Newtonian medium ($n = 1$), whose viscosity is the same as the zero-shear-rate viscosity of the shear-thinning fluid (dashed lines). The variations of the terminal velocity (v_T) of the bubble for different Eo for shear-thinning and Newtonian surrounding fluids are shown in Fig. 5.16(c). It can be seen in Fig. 5.16(a,c) that the rise velocity of the bubble in the shear-thinning fluid is higher than that in the Newtonian medium. The terminal velocities of the bubble presented in Fig. 5.16(c) are obtained by measuring the slopes of the lines (z_{CG} versus t) in Fig. 5.16(a) for $1 \leq Eo \leq 100$. This observation is explained as follows. The viscosity of a shear-thinning fluid decreases with an increase in shear stress. Therefore, as the bubble rises, the viscosity of the surrounding fluid near the bubble decreases (high shear region). This in turn reduces the drag force acting on the rising bubble, which results in an increase of the rise velocity of the bubble in a shear thinning fluid, as compared to the Newtonian fluid. This thinning effect is significant for lower values of Eo. Fig. 5.16b shows that the shape of the bubble reaches a terminal oblate shape for lower values of Eo, but the bubble forms a skirt for high value of Eo ($Eo = 100$), and the dynamics remains unsteady even at latter times. The aspect ratio (h/w) decreases (i.e. the bubble becomes more oblate) as the value of Eo increases. A close inspection of Fig. 5.16(b) also reveals that the deformation of the bubble is more in the case of a shear-thinning fluid as compared to a Newtonian fluid as a surrounding medium.

The spatio-temporal evolutions of shapes of the bubbles are shown in Fig. 5.17(a) and (b) for for $Eo = 1$ and 100, respectively. For each Eo, the second column shows the results for a Newtonian fluid with viscosity the same as the zero-shear-rate viscosity of the shear-thinning

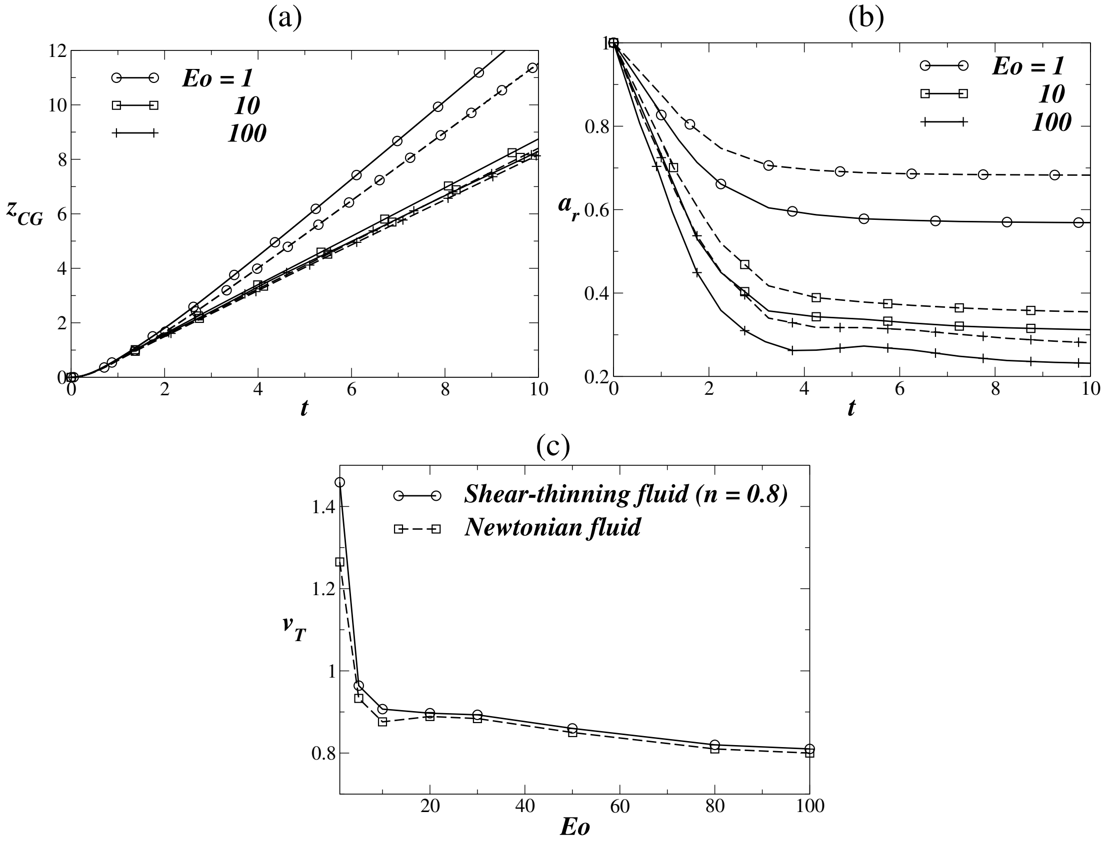

Figure 5.16: Variation of (a) the center of gravity and (b) the aspect ratio (h/w) of the bubble with time for different values of Eo for $n = 0.8$ (solid lines). (c) The variations of the terminal velocity (v_T) of the bubble for different Eo for shear-thinning and Newtonian surrounding fluids. Dashed lines show the results corresponding to the Newtonian fluid ($n = 1$), whose viscosity is the same as the zero-shear-rate viscosity of the shear-thinning fluid. The rest of the parameter values are $Ga = 10$, $\lambda = 10$, $\mu_r = 10^{-2}$ and $\rho_r = 10^{-3}$.

fluid. The third and fourth columns present the results for shear-thinning fluids with $n = 0.5$ and $n = 0.2$, respectively. In the first column for each Eo, we have also plotted the spatio-temporal evolutions of the bubble rising in a Newtonian fluid with viscosity equal to the viscosity of the shear-thinning fluid at a dimensionless shear-rate of unity.

It can be seen that for $Eo = 1$ (Fig. 5.17(a)) the bubble shape becomes a steady oblate (at $t \geq 10$) for all the surrounding fluids considered. It can also be observed in Fig. 5.17(a) that the upper part of the bubble becomes slightly flattened for shear-thinning fluids. This flattening effect is increased with an increase in the shear-thinning tendency (i.e. decrease in the value of the flow index, n). This behaviour is more prominent for $Ga = 20$ (see Fig. 5.19 for more discussion). Comparing the Newtonian fluid results presented in first and second columns of Fig. 5.17(a), it can be observed that the dynamics is not influenced by the scaling of Newtonian fluid viscosity for $Eo = 1$.

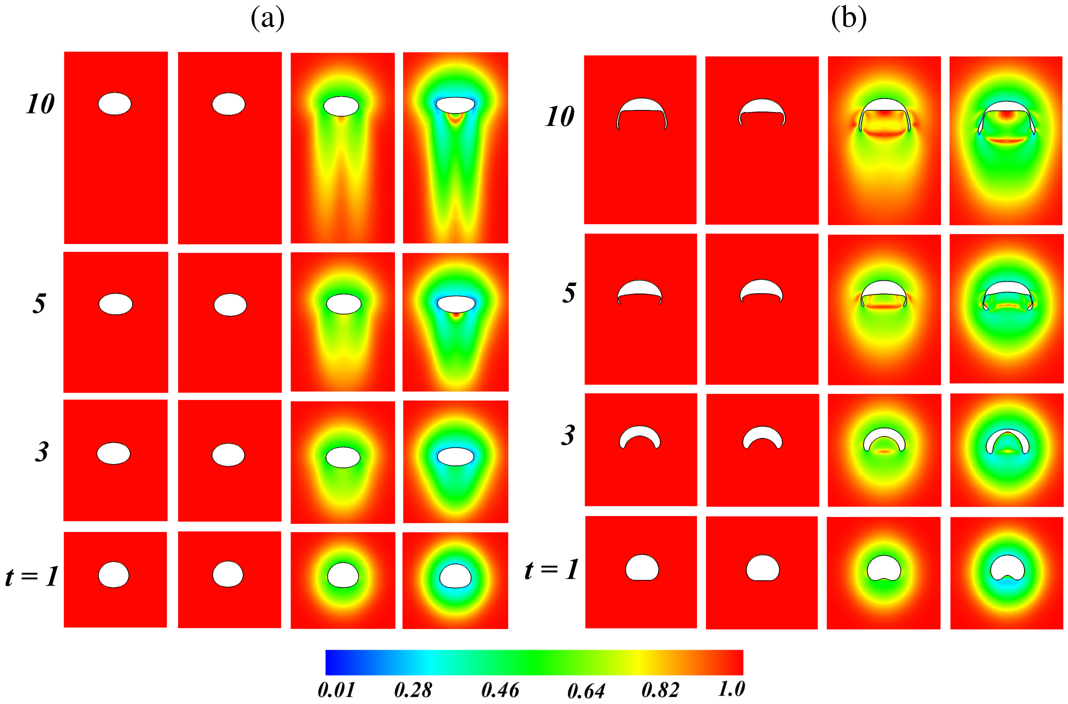

Figure 5.17: The spatio-temporal evolutions of the shapes of the bubbles for (a) $Eo = 1$ and (b) $Eo = 100$. For each Eo value, the first column shows the results for a Newtonian fluid ($n = 1$) with viscosity the same as that of the shear-thinning fluid at the dimensionless shear-rate of unity; the second column shows the results for Newtonian fluid ($n = 1$) with viscosity the same as that of the shear-thinning at zero-shear-rate; the third and fourth columns show the results for shear-thinning fluid with $n = 0.8$ and shear thinning fluid with $n = 0.6$, respectively. The rest of the parameter values are the same as those used in Fig. 5.16.

For $Eo = 100$, it can be seen from Fig. 5.17(b) that the skirt of the bubble at latter times ($t \geq 10$) bends toward the inner region for Newtonian case. This effect is more pronounced in a Newtonian fluid whose viscosity is the same as that of the shear-thinning fluid at a dimensionless shear-rate of unity (first column) as compared to a Newtonian fluid having viscosity equal to the zero shear-rate viscosity (second column). For shear-thinning fluids, the skirt of the bubble expands toward the outer region at later times. However, close inspection of Fig. 5.17(b) reveals that the length of the skirt of the bubble in a Newtonian fluid whose viscosity is the same as that of the shear-thinning fluid at a dimensionless shear-rate of unity lies in between those observed in the shear-thinning fluid with $n = 0.8$ and Newtonian fluid with the viscosity the same as that of a shear-thinning fluid at the zero-shear rate. The deformation of the bubble leads to different streamline patterns which are shown in Fig. 5.18. It can be seen from Fig. 5.18 that for $Eo = 1$ two circulating regions appear inside the bubble, without any additional recirculating zones in the wake region of the bubble for both the Newtonian ($n = 1$) and shear-thinning fluids. For $Eo = 10$, the bubble deforms more and forms two additional recirculating zones in the wake of the bubble. The size of these recirculating zones increases with an increase in the shear-thinning

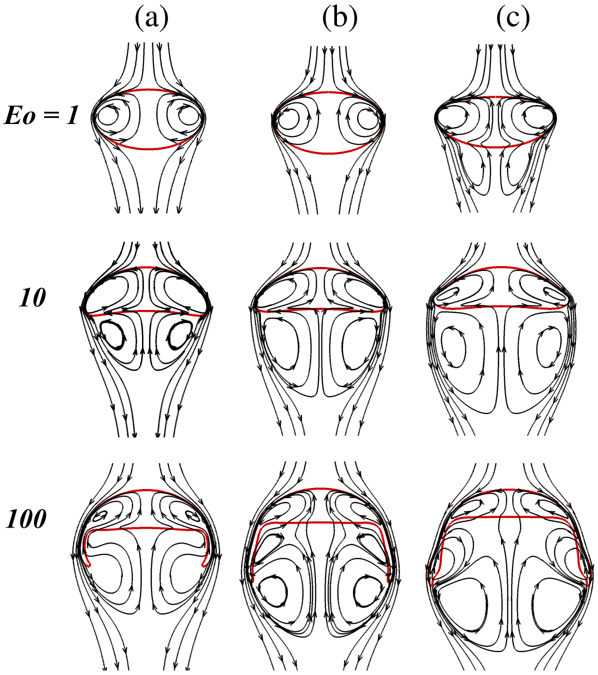

Figure 5.18: Streamline patterns at $t = 30$ for different values of Eo for (a) Newtonian, (b) shear-thinning fluid with $n = 0.8$ and (c) shear-thinning fluid with $n = 0.6$, respectively. The rest of the parameter values are the same as those used to generate Fig. 5.16.

tendency (decreasing n) of the surrounding fluid. In the skirted bubble case for $Eo = 100$, in addition to the four recirculating zones (two inside and two in the wake of the bubble), two more recirculating zones appear surrounding the skirt of the bubble. In Fig. 5.18 and rest of the figures, while presenting the Newtonian fluid results, we only show the results obtained for Newtonian fluid with viscosity the same as that at the zero-shear rate of the shear-thinning fluid.

The effect of Galilei number on the dynamics of an air bubble in a shear-thinning fluid is discussed next. The temporal variations of the center of gravity and the aspect ratio of the bubble are plotted in Fig. 5.19(a) and (b), respectively for different values of Ga. The variations of the terminal velocity (v_T) of the bubble for different Ga for shear-thinning and Newtonian surrounding fluids are also shown in Fig. 5.19(c). It can be seen in Fig. 5.19(a,c) that for lower Ga ($Ga = 1$), the rise velocities of the bubble in Newtonian ($n = 1$) and shear-thinning (with $n = 0.5$) fluids are almost equal. For $Ga = 1$, even though the viscosity of the surrounding fluid decreases (to approximately 80% of the value at zero shear-rate) near the bubble due to shear, the bubble remains spherical for this set of parameter values (as shown in Fig. 5.20(a)). This is due to the fact that for the same size of the bubble, for $Ga = 1$ the surrounding fluid viscosity is high enough so that the dynamics and shape of the bubble do not change even when the viscosity decreases to 80 % of the maximum viscosity. It can be seen in Fig. 5.19(b) that there is a little difference in the aspect ratios of the bubble for both the shear-thinning and Newtonian

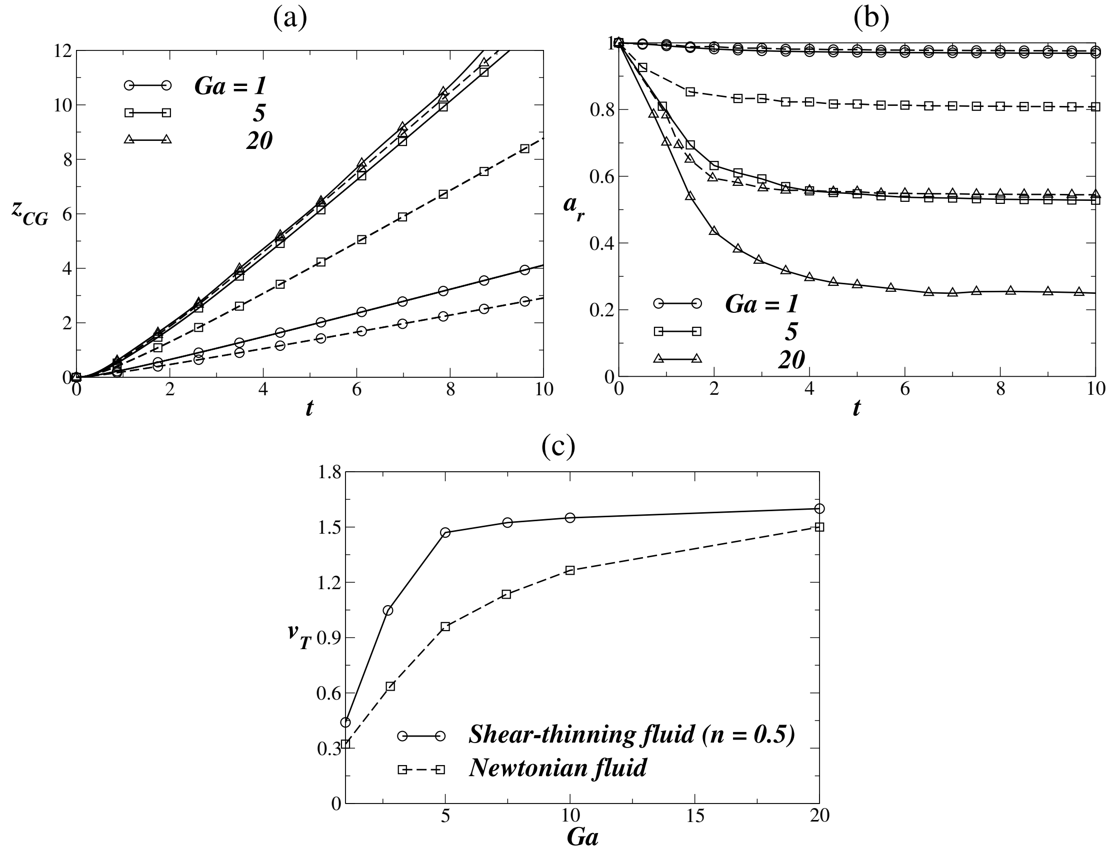

Figure 5.19: Variation of (a) center of gravity, and (b) aspect ratio (h/w) of the bubble, with time for different values of Ga for a shear thinning fluid with $n = 0.5$ (solid lines). The Newtonian fluid, (whose viscosity is the same as the zero-shear rate viscosity of the shear-thinning fluid) results are shown by dashed lines. (c) The variations of the terminal velocity (v_T) of the bubble for different Ga for shear-thinning and Newtonian surrounding fluids. The rest of the parameter values are $Eo = 1$, $\lambda = 10$, $\mu_r = 10^{-2}$ and $\rho_r = 10^{-3}$.

fluids for $Ga = 1$. For higher values of Ga the difference between the dynamics of a bubble in Newtonian and shear-thinning fluid is apparent. It can be observed that increasing Ga increases the deformation of the bubble (reflected in its aspect ratio). For $Ga = 20$, the aspect ratio of the bubble in shear-thinning fluid is almost half of that of the bubble in the Newtonian fluid for this set of parameters. The increased deformation at higher Galilei numbers can also be observed from Fig. 5.20, which shows the spatio-temporal evolution of the bubble shape for $Ga = 1$ (Fig. 5.20a) and $Ga = 20$ (Fig. 5.20b). In Fig. 5.20(b) for $Ga = 20$, an oblate shaped bubble is observed in the case of a Newtonian fluid, but the bubble deforms more and forms a clearly visible flat region at the top of the bubble in case of shear-thinning fluid due to the significant decrease in the viscosity of the surrounding fluid near the upper part of the rising bubble. The tail of the less viscous surrounding shear-thinning fluid is also observed to increase as time progress for $Ga = 20$ (see Fig. 5.20(b)).

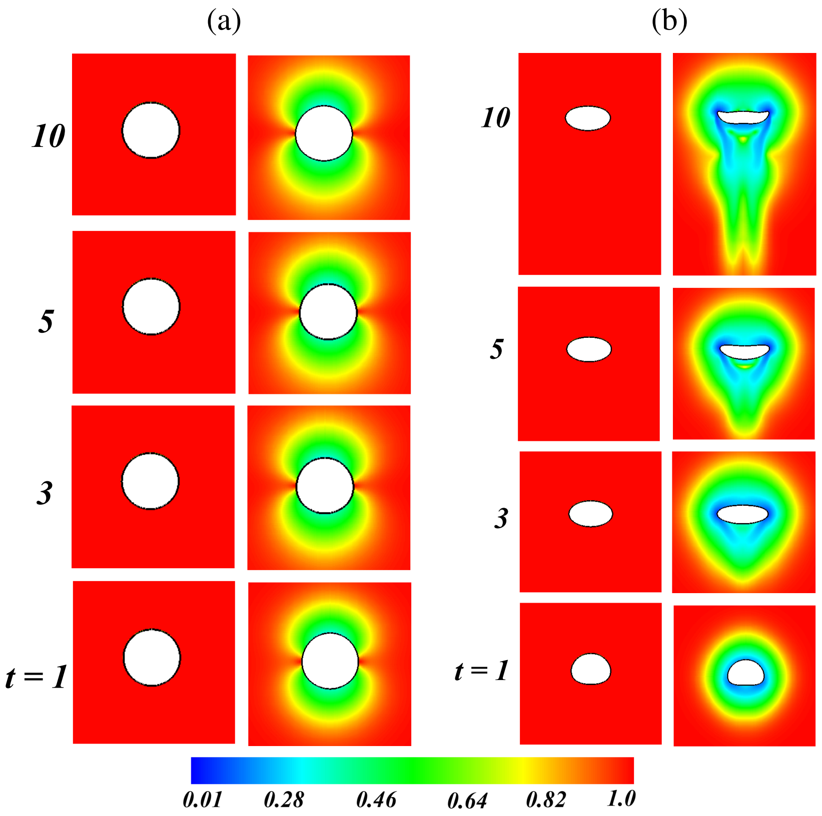

Figure 5.20: The spatio-temporal evolution of the shapes of the bubble for (a) $Ga = 1$ and (b) $Ga = 20$. The first and second columns in each panel represent the Newtonian ($n = 1$) and the shear-thinning ($n = 0.5$) fluids results. The background color contours represent the viscosity variations. The rest of the parameter values are the same as those used to generate Fig. 5.19.

Finally, the effect of the flow index n (a measure of the shear thinning tendency) on the rising bubble dynamics is investigated. Fig. 5.21(a) and (b), show a plot of the variation of the center of gravity and the aspect ratio of the bubble for four different values of n. It can be seen that the rise velocity (aspect ratio) of the bubble increases (decreases) with an increase in the shear thinning tendency of the surrounding fluid, i.e. by decreasing the value of n. In Fig. 5.22(a) and (b), variation of the terminal velocity (panel a) and aspect ratio (panel b) of the bubble when it reaches to a steady state are plotted versus n for different values of Eo. It can be seen that increasing n, which implies a decrease in the shear thinning tendency, decreases (increases) the terminal velocity (aspect ratio) of the bubble for all the Eötvös numbers considered. However, the effect is more prominent for lower Eo (i.e high interfacial tension).

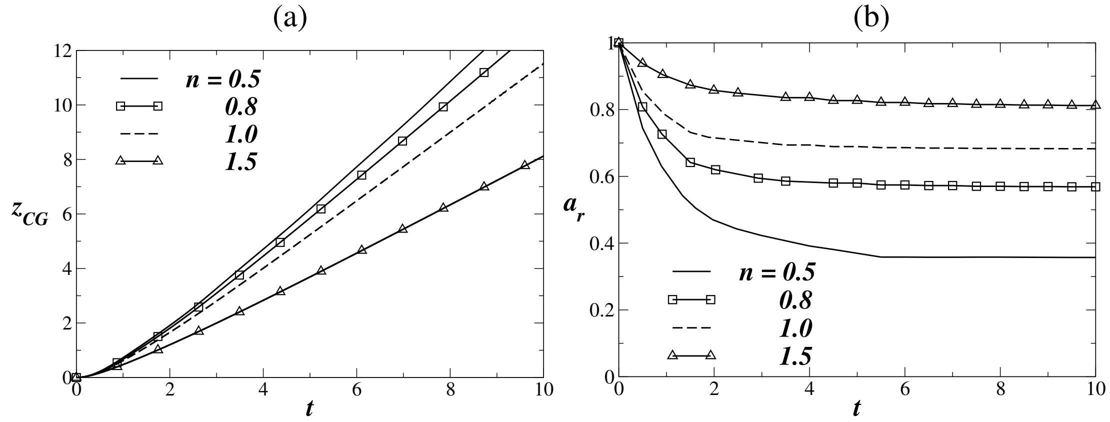

Figure 5.21: Variation of (a) center of gravity, and (b) aspect ratio of the bubble, with time for different values of n. The rest of the parameter values are $Ga = 10$, $Eo = 1$, $\lambda = 10$, $\mu_r = 10^{-2}$ and $\rho_r = 10^{-3}$.

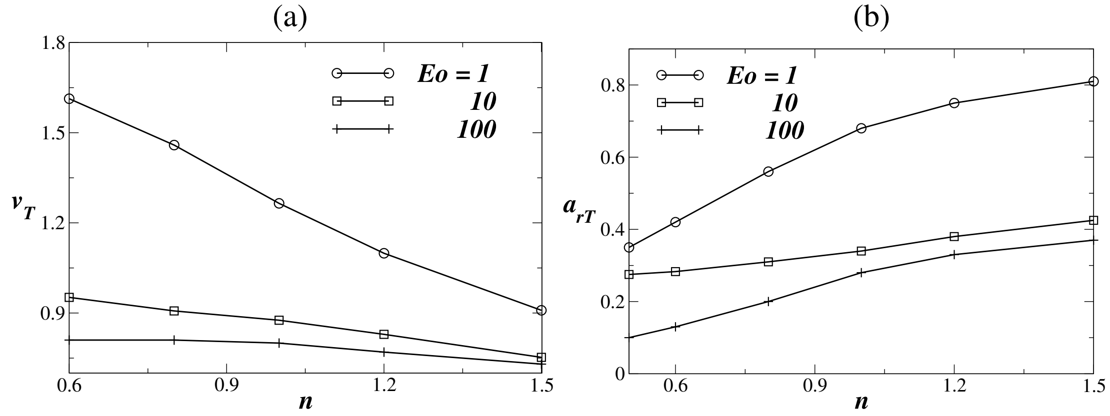

Figure 5.22: Variation of (a) terminal velocity and (b) aspect ratio of the bubbles at their terminal states, with n for different values of Eo. The rest of the parameter values are the same as those used to generate Fig. 5.21.

5.2.3 Concluding remarks

The dynamics of a rising air bubble in a non-Newtonian fluid (shear thinning) has been studied via numerical simulations in the axisymmetric regime. First a grid-convergence test has been performed for a typical set of parameters used in the present study. The validation of the non-Newtonian formulation is also conducted by comparing the results obtained from the present solver with those of Zhang *et al.* (2010).

A parametric study is conducted by varying shear thinning flow index 'n' for different Galilei and Eötvös numbers. The effect of these parameters is quantified in terms of their influence on the aspect ratio of the bubble, the position of the center of gravity and the bubble shape as these evolve over time. The flow patterns are investigated by plotting viscosity distribution and streamlines. Increasing the shear thinning tendency is found to increase the rise velocity, and reduce the deformations of the bubble. The deformation of the bubble is found to be more for higher *Ga* and low *Eo*. A comparison of the bubble behavior in shear thinning fluids with their behavior in Newtonian fluids is also made. It is worth exploring the dynamics of rising bubble in non-Newtonian fluids in the other regimes, i.e high *Ga* and moderate to high *Eo*, where the dynamics is three-dimensional, by performing three-dimensional simulations and experiments. This is the subject of discussion in the next section.

5.3 An air bubble rising in a Carreau-Yasuda shear-thinning liquid: three-dimensional effect

In this section, the dynamics of a rising bubble in a Carreau-Yasuda shear-thinning fluid in investigated via three-dimensional simulations and experiments using CMC solutions. It is found that for the parameter values considered in this section, a rising bubble in this fluid exhibits three-dimensional behaviour, i.e. path instabilities (zigzagging/spiralling motion) and topological changes. For the same set of parameters, a bubble maintains azimuthal symmetry and rises in a straight path while rising in a Newtonian surrounding fluid. The mechanism of this three-dimensional behaviour is also investigated by plotting the vorticity and viscosity contours, an approach similar to the one reported by earlier researchers for Newtonian fluids (Cano-Lozano *et al.*, 2016*a*; Tripathi *et al.*, 2015*a*; Zenit & Magnaudet, 2002). The experimental results obtained using CMC solutions qualitatively agree with those of the corresponding numerical simulations. Our work differs from Ohta and co-workers (Ohta *et al.*, 2012, 2009) as discussed below. A larger computational domain is used to remove the wall effect to get accurate bubble dynamics. The computational domain used by them does not eliminate the wall effect as seen in some of their results where the viscosity variation already reached upto the walls, indicating that wall effect must have been encountered in those situations. Also smaller height of their domain ($16R$) would not capture the oscillation dynamics as we observe that a typical bubble starts to oscillate only after reaching a certain height (i.e at $z \approx 20R$) for the set of parameter values considered in our study. An extensive parametric study is also conducted using the rheological constants obtained for real fluids. The viscosity model is the same as the one discussed in Section 5.2, and the detail of the numerical method used is discussed in Chapter 2. The governing equations are solved using the no-slip and the no-penetration boundary conditions at the walls and an open boundary condition at the top and bottom parts of the domain. Further, we checked that the size of the computational domain bigger than the one chosen in the present study has negligible effect on the flow dynamics.

5.3.1 Numerical results and discussion

In order to contrast the behaviour of bubble rise in shear-thinning and Newtonian fluids, we perform three-dimensional numerical simulations for two sets of dimensionless parameter values. The first set, $Ga = 30$ and $Eo = 1$, lies near the boundary of regions I (axisymmetric) and III (spiralling), whereas the second set, $Ga = 30$, $Eo = 25$, lies in region II (skirted) for

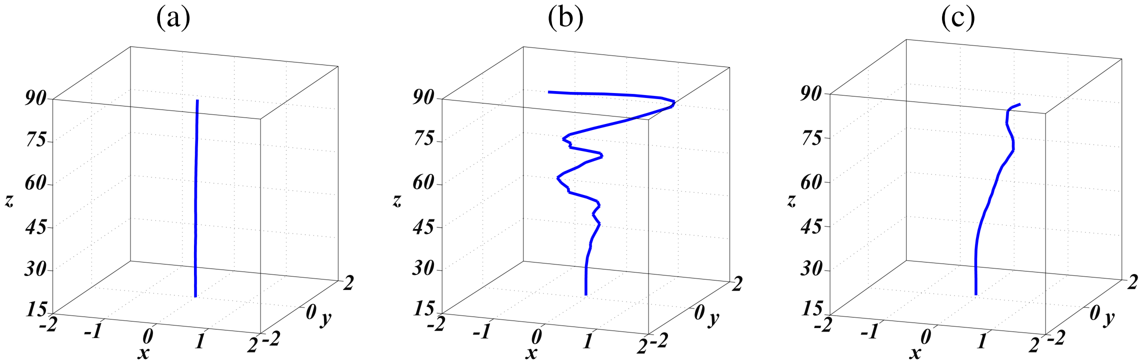

Figure 5.23: Trajectories of the air bubble rising in (a) Newtonian fluid ($\lambda = 0$, $n = 1$) having viscosity the same as that of the shear-thinning fluid at zero shear rate (Newtonian fluid '1'), (b) shear-thinning fluid ($\lambda = 6$, $n = 0.6$) and (c) Newtonian fluid ($\lambda = 0$, $n = 1$) having viscosity the same as that of the shear-thinning fluid at the dimensionless shear rate of unity (Newtonian fluid '2'). The rest of the parameters are $Ga = 30$ and $Eo = 1$.

a surrounding Newtonian fluid, as shown in Fig. 1.2. As suggested by Tripathi *et al.* (2015*a*), an air bubble while rising through a Newtonian fluid for these sets of parameters will maintain azimuthal symmetry.

For an air bubble rising in a shear-thinning fluid, one would expect a decrease in viscosity of the surrounding fluid in the vicinity of the bubble because of the increase in shear rate. Thus, for the first set of parameters, it can be expected that an air bubble in a shear-thinning fluid will start rising axisymmetrically (low shear rate) and later move to region III (high shear rate) due to the decrease in local viscosity of the surrounding fluid (and hence an increase in local Ga). Similarly, for the second set of parameters, an air bubble in a shear-thinning fluid is expected to go from region II (skirted) to regions IV and V (break-up). The two sets of parameters chosen illustrate three-dimensionality of the rising bubble in a shear-thinning fluid, namely the path instability (first set) and the three-dimensional topological change (second set).

First set: $Ga = 30$ **and** $Eo = 1$

The trajectory (i.e., the locus of centre of gravity) of the bubble rising in a Newtonian fluid with viscosity the same as that of the shear-thinning fluid ($\lambda = 6$, $n = 0.6$) at zero shear rate (hereafter, referred as Newtonian fluid '1') is shown in Fig. 5.23(a). Fig. 5.23(b) shows the trajectory for the corresponding shear-thinning fluid. It can be seen in Fig. 5.23(a) that, as expected, the bubble rises vertically along the axis of symmetry of the channel for the Newtonian fluid. In case of the shear-thinning fluid, the bubble rises in a vertical path along the axis of symmetry of the channel upto $z \approx 45$, but then undergoes a three-dimensional path. The direction of this wobbling motion is arbitrary as there is no wall effect (see Tripathi *et al.* (2015*a*) and references therein). A slight change in the condition can change the direction in which the bubble migrates in the lateral plane. This shows a clear effect of shear-thinning nature of the surrounding fluid on the bubble rise behaviour. A question that arises is: can we get similar dynamics as Fig. 5.23(b) by using a Newtonian fluid of viscosity equal to a value lower than the viscosity at zero shear rate. From Eq. (5.12), the dimensionless viscosity of the shear-thinning fluid is $\left[1 + (\lambda\Pi)^2\right]^{(n-1)/2}$. At the dimensionless shear rate of unity ($\Pi = 1$), the viscosity of the shear-thinning fluid is 0.486 for $\lambda = 6$ and $n = 0.6$ (the parameters considered in Fig. 5.23. Thus, when we considered a Newtonian fluid having a viscosity the same as that of the shear thinning fluid at the dimensionless shear rate of unity, we considered a viscosity which is an average value of total viscosity variation in case of shear-thinning fluid. Also, at the dimensionless shear rate of unity, it is expected that the viscosity is measured at the stress magnitudes which dominate the dynamics of the flow. To answer the above question, in Fig 5.23(c), we present the trajectory of an air bubble rising in a Newtonian fluid with viscosity the same as that of the shear-thinning fluid at the dimensionless shear rate of unity (hereafter, referred as Newtonian fluid '2'). In this case, the bubble just migrates away from the axis of symmetry of the channel. The trajectory is visibly different from that shown in Fig. 5.23(b). This reveals that the three-dimensional behaviour observed in Fig. 5.23(b) is due to the shear-thinning behaviour of the surrounding fluid and not simply due to an overall decrease in fluid viscosity of the Newtonian fluid.

The three-dimensional features are also reflected in the shapes of the rising bubble as shown in Fig. 5.24. In case of Newtonian fluid '1', the initially spherical bubble deforms into steady oblate shape (Fig. 5.24(a)). It can be seen that even at an early time ($t = 10$) the bubble has reached the terminal shape from its initially spherical shape. On the other hand, for the shear-thinning fluid (Fig. 5.24(b)), the bubble undergoes shape deformation even at later times and never reaches a steady state, and the bubble behaves like a bubble in region III of Fig. 1.2 (zigzagging/spiralling bubble). We now verify that this three-dimensional behaviour is indeed a consequence of shear thinning nature and not just due to reduction of viscosity of the Newtonian fluid. In Fig. 5.24(c), the evolution of bubble shapes rising in Newtonian fluid '2' is shown. In this case, the bubble deforms to an almost axisymmetric shape, which is different from Fig. 5.24 (b) for the shear-thinning fluid.

In order to understand the mechanism of these differences, we plot the evolutions of vorticity component in the z direction for the Newtonian fluid '1' and the corresponding shear-thinning fluid, which are shown in Fig. 5.25(a) and (b), respectively. This plot is generated using the same parameter values as those of Fig. 5.23. It can be seen that steady patches of

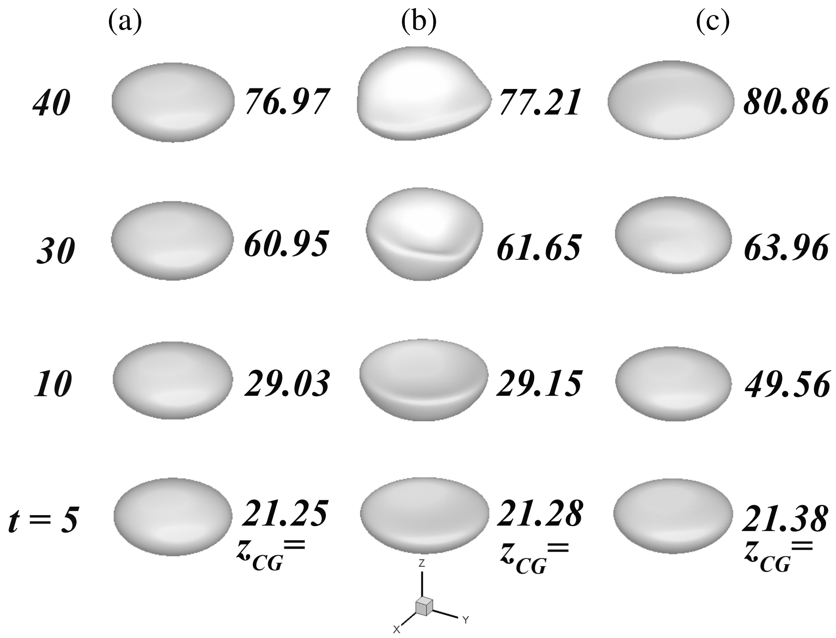

Figure 5.24: Evolution of the shape of the bubble rising in (a) Newtonian fluid ‘1’, (b) shear-thinning fluid (λ = 6, n = 0.6) and (c) Newtonian fluid ‘2’. The rest of the parameters are the same as those of Fig. 5.23. In panel (b), the viscosity of the shear thinning fluid decreases as we move up in the vertical direction.

z vorticity form surrounding the equator of the bubble rising in the Newtonian fluid (see Fig. 5.25(a)). A similar vorticity pattern is also observed (not shown) for the Newtonian fluid ‘2’. In case of shear-thinning surrounding fluid (see Fig. 5.25(b)), the z vorticity elongates to form a pair of counter-rotating two-threaded vortices in the wake region of the bubble at early times ($t \leq 10$). This is followed by shedding of vortices, which can be seen at $t \geq 20$. At $t \approx 20$ the bubble reaches $z \approx 45$ for the parameters considered in Fig. 5.23. Due to vortex shedding in the wake region, the bubble deforms asymmetrically, which in turn makes the largest area of the bubble oriented towards the direction of motion. This causes the vortex shedding to change the direction, and thereby changing the orientation of the bubble. This process continues and the bubble moves in a zigzagging/spiralling path. A physical explanation can also be derived from the vortex shedding pattern. The asymmetric vortex shedding causes the bubble to experience asymmetric drag and lift forces. The spiralling motion gets stabilized at a frequency which matches with the frequency of vortex shedding/change in lift and drag forces. From this result, we can conclude that a bubble in the oscillatory region (for non-Newtonian fluid in Fig. 5.25(b)) is associated with vortex shedding. However, it is difficult to comment on the dominant mechanism (vortex shedding or Crow instability (Crow, 1970)) at the onset of the oscillatory motion of the bubble.

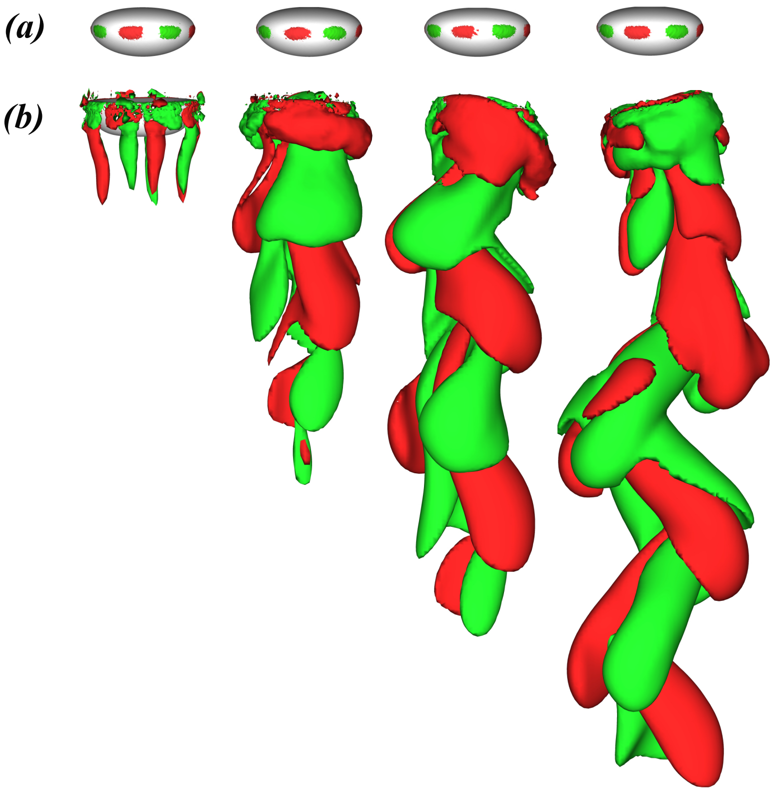

Figure 5.25: Evolution of iso-surfaces of the vorticity ($\omega_z = \pm 0.2$) component in the z direction. (a) Newtonian fluid ‘1’, (b) shear-thinning fluid ($\lambda = 6$, $n = 0.6$). From left to right: $t = 10$, 20, 25 and 30. The rest of the parameters are the same as those of Fig. 5.23. In panel (b), the viscosity of the shear thinning fluid decreases with increase in t (i.e., from left to right).

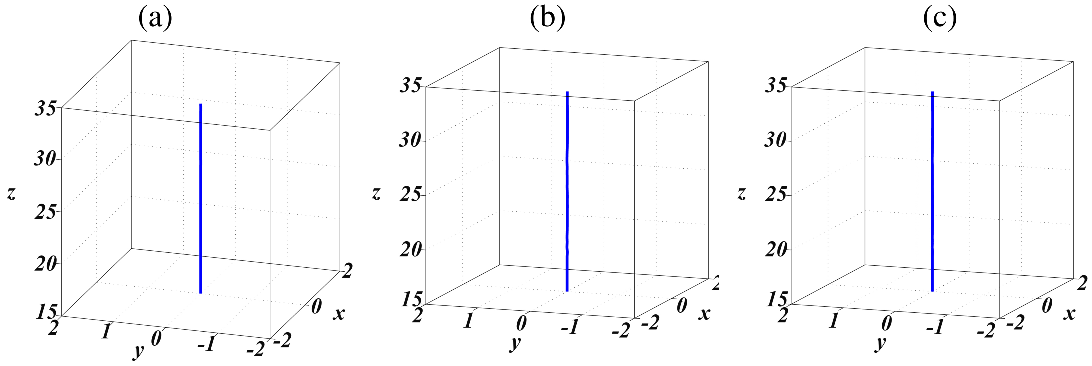

Figure 5.26: Trajectories of the bubble rising in (a) Newtonian fluid ‘1’, (b) shear-thinning fluid ($\lambda = 6$, $n = 0.6$) and (c) Newtonian fluid ‘2’. The rest of the parameters are $Ga = 30$ and $Eo = 25$.

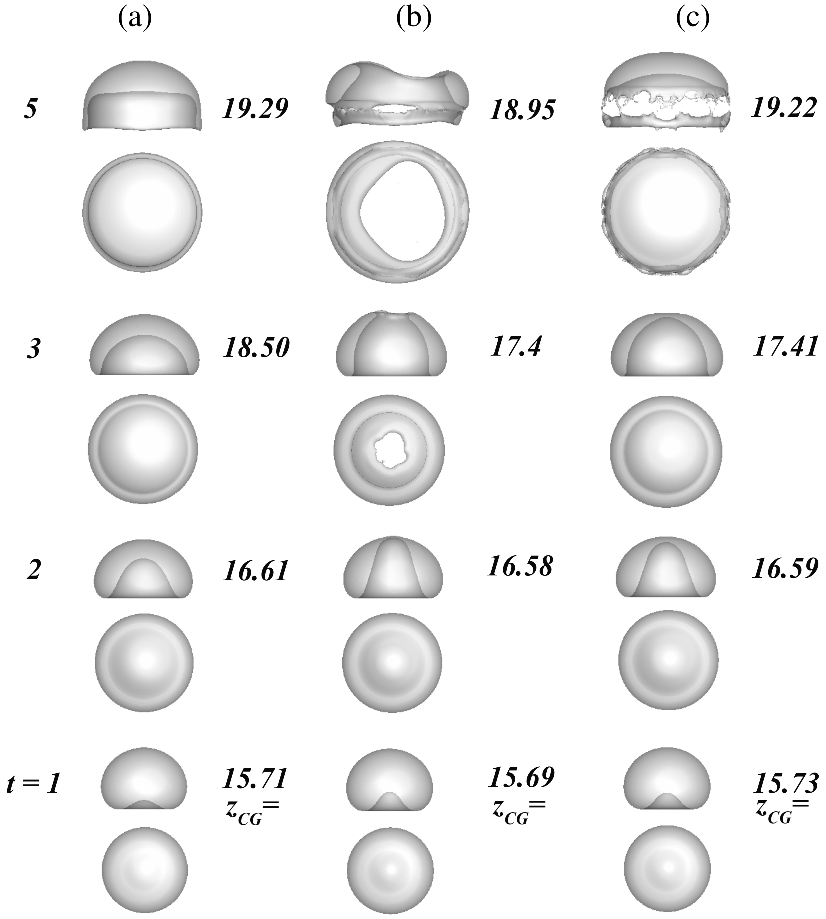

Figure 5.27: Evolutions of the shape of the bubble rising in (a) Newtonian fluid ‘1’, (b) shear-thinning fluid ($\lambda = 6$, $n = 0.6$), (c) Newtonian fluid ‘2’. The top and bottom panels at each time represent the front ($y - z$ plane) and top ($x - y$ plane) views, respectively. The rest of the parameters are the same as those of Fig. 5.26. The locations of center of gravity of the bubble are also given. In panel (b), the viscosity of the shear thinning fluid decreases as we move up in the vertical direction.

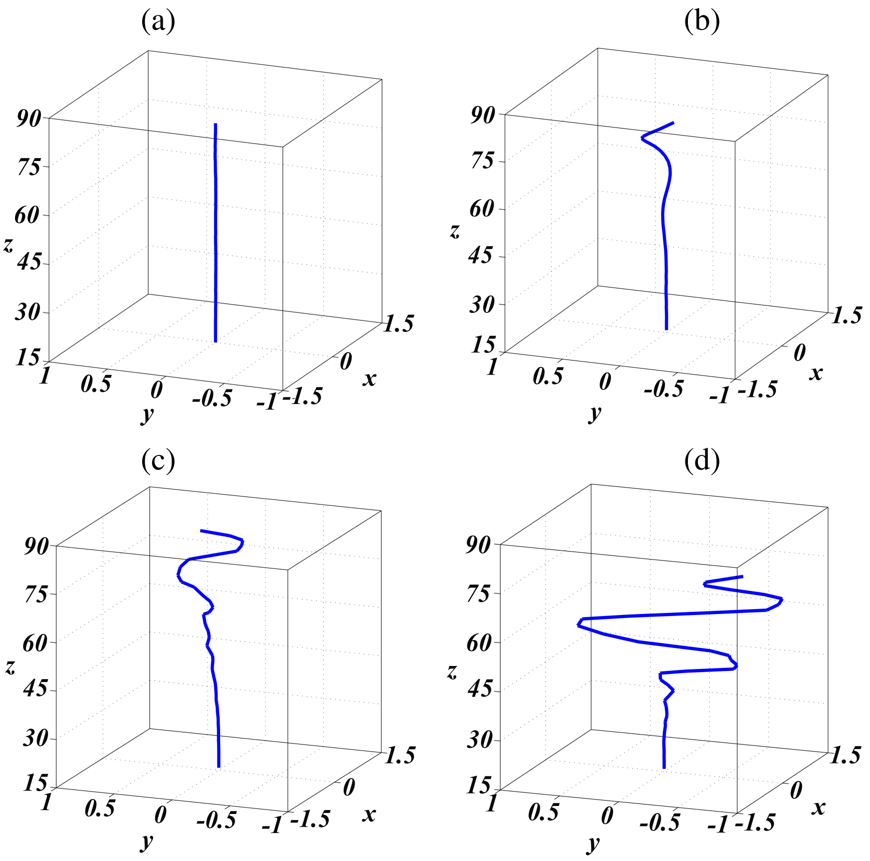

Figure 5.28: Trajectories of an air bubble rising in shear-thinning fluids with different values of the flow index, n: (a) $n = 1$ (Newtonian fluid), (b) $n = 0.8$, (c) $n = 0.6$ and (d) $n = 0.3$. The rest of the parameters are $\lambda = 6$, $Ga = 25$ and $Eo = 1$.

Second set: $Ga = 30$**,** $Eo = 25$

The above discussion focused on the path instability of the bubble using the first set of parameters. Next we investigate the topological change of a rising air bubble associated with the second set of parameters. Fig. 5.26 shows that a bubble moves along the axis of symmetry of the channel in the Newtonian (Fig. 5.26(a)) and shear-thinning fluids (Fig. 5.26(b)). The trajectory remains the same even when we change the viscosity of the Newtonian fluid to be equal to the viscosity of the shear-thinning fluid at a dimensionless shear rate of unity (Fig. 5.26(c)). Note that the comparison between the Newtonian and shear-thinning fluids is not straightforward because of the inherent lowering of the overall viscosity in case of the shear-thinning fluids. At the dimensionless shear rate of unity, it is expected that the viscosity is measured at the stress magnitudes which dominate the dynamics of the flow. For this set of parameters, the evolution of the shape of the bubble rising in Newtonian fluid '1' is shown in Fig. 5.27(a). Fig. 5.27(b) shows the evolution of the shape of the bubble for the corresponding shear-thinning fluid. The bubble rising in the Newtonian fluid (Fig. 5.27a) undergoes a change in shape to form a dimple

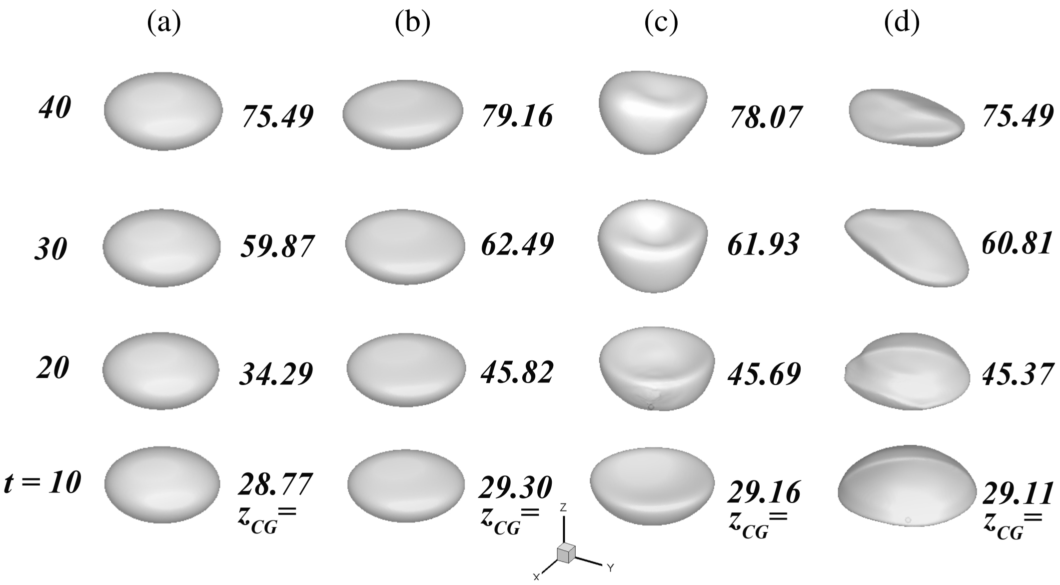

Figure 5.29: Evolutions of the shape of the bubble for different values of the shear-thinning flow index, n: (a) $n = 1$ (Newtonian fluid), (b) $n = 0.8$, (c) $n = 0.6$ and (d) $n = 0.3$. The rest of the parameters are same as those of Fig. **??**. The viscosity of the shear thinning fluid decreases with decrease in the value of n at a fixed time (i.e., from left to right at each time).

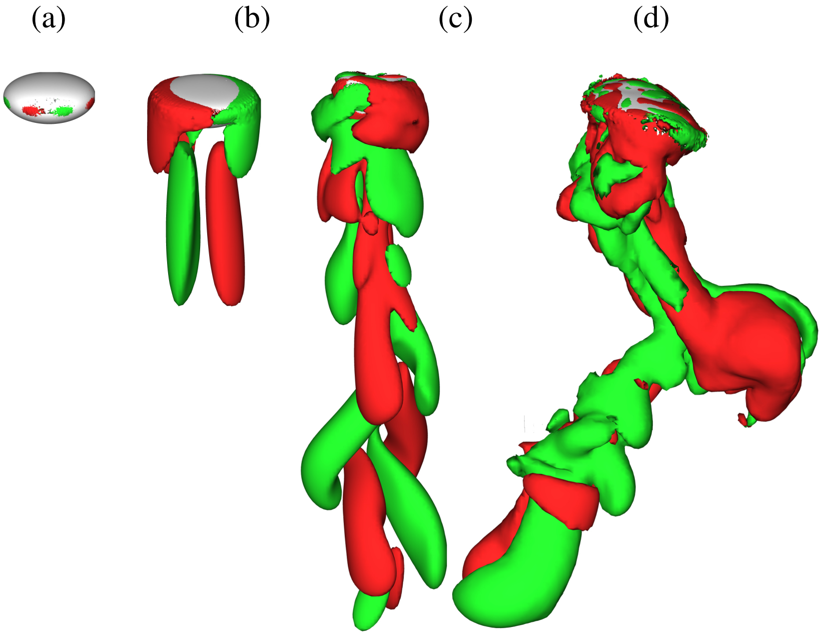

Figure 5.30: Iso-surfaces of the vorticity component in the z direction ($\omega_z = \pm 0.5$) at $t = 40$. (a) $n = 1$ (Newtonian fluid), (b) $n = 0.8$, (c) $n = 0.6$ and (d) $n = 0.3$. The rest of the parameters are the same as those of Fig. 5.28. The viscosity of the shear thinning fluid decreases from left to right.

(a) *x*-*z* plane

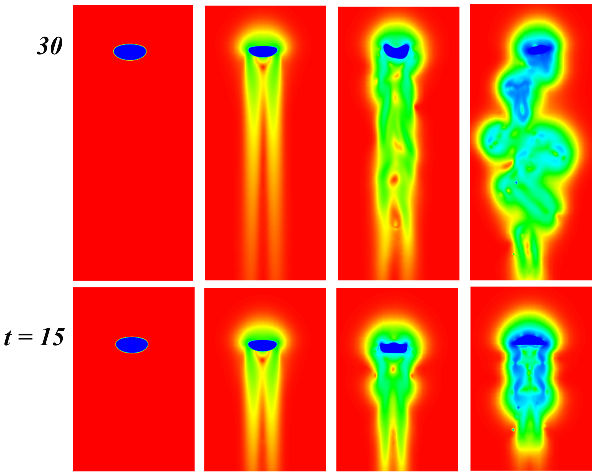

(b) *y*-*z* plane

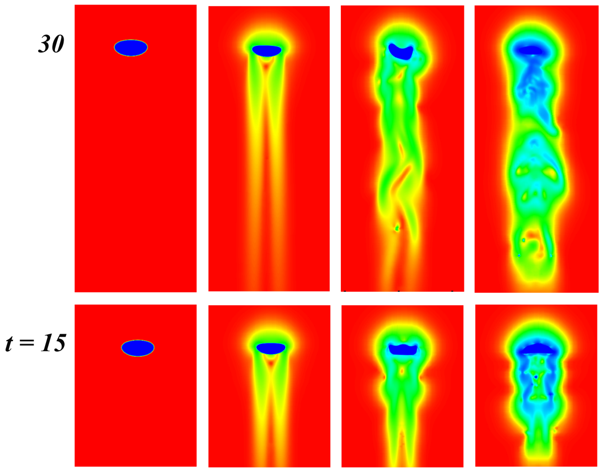

(c) *x*-*y* plane

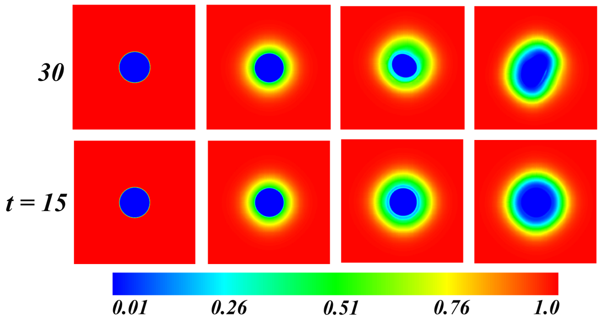

Figure 5.31: Viscosity contours in (a) *x*-*z*, (b) *y*-*z* and (c) *x*-*y* planes passing through the center of gravity of the bubble at $t = 15$ and $t = 30$ for different values of n (left to right: $n = 1$, 0.8, 0.6 and 0.3). The rest of the parameters are the same as those of Fig. 5.28.

at the early times (see bubble shape at $t = 2$), which further deforms to form a skirted bubble (see bubble shape at $t = 5$). In contrast, the bubble rising in the shear-thinning fluid (Fig. 5.27b) for the same Galilei and Eötvös numbers undergoes a central-type break up at $t = 3$, which further breaks from the bottom to release a ring-type structure (see $t = 5$ in Fig. 5.27(b)). Thus, we conclude that an air bubble in region II for a Newtonian fluid behaves as a bubble in the central breakup region (region V) when it rises through the shear-thinning fluid for this set of parameter values. The same bubble when rising in Newtonian fluid '2' (see Fig. 5.27(c)) undergoes a peripheral break-up (region IV in Fig. 1.2). The results discussed so far reveal that the three-dimensional behaviour of a rising bubble in a shear-thinning fluid is due to the gradual decrease in local fluid viscosity (and hence increase in local Ga) with shear. Using an effective viscosity for a Newtonian fluid does not lead to the same bubble rise dynamics. Thus, in the rest of this section, while presenting the Newtonian fluid results, we only show the results obtained for Newtonian fluid with viscosity the same as that at the zero shear rate of the corresponding shear-thinning fluid.

In order to gain further insight into the effect of shear thinning tendency, we have conducted a parametric study by varying the flow index, n and the inelastic time constant, λ. For generating the rest of the results in this section, we chose $Ga = 25$ and $Eo = 1$, which lies in region I for Newtonian fluids (see Fig. 1.2).

Effect of flow index, n

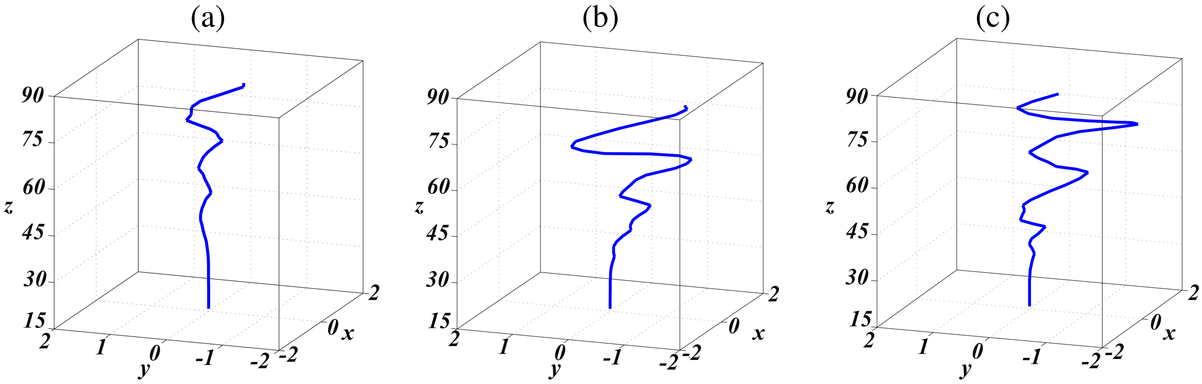

Figure 5.32: Trajectories of an air bubble rising in shear-thinning fluids with different values of λ: (a) $\lambda = 2$, (b) $\lambda = 8$ and (c) $\lambda = 10$. The rest of the parameters are $n = 0.6$, $Ga = 30$ and $Eo = 1$.

The trajectories of the rising bubble are shown in Fig. 5.28 for four different values of the flow index, n. Note that $n = 1$ (Fig. 5.28(a)) represents the Newtonian fluid case. It can be seen that for the Newtonian fluid, the bubble rises vertically along the axis of symmetry of the channel. For $n = 0.8$ (Fig. 5.28(b)), the trajectory of the bubble becomes slightly curved

(a) *x*-*z* plane

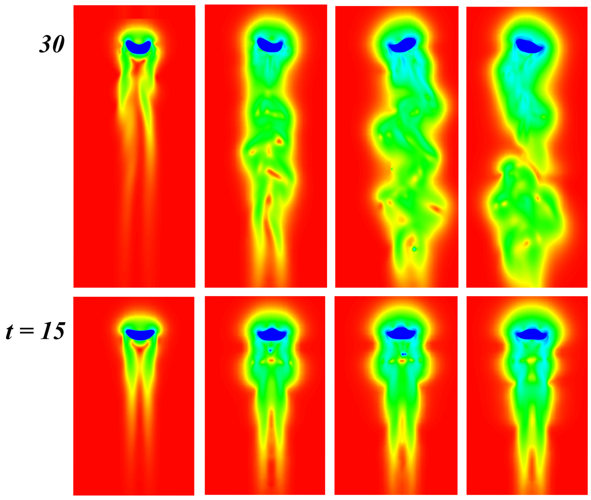

(b) *y*-*z* plane

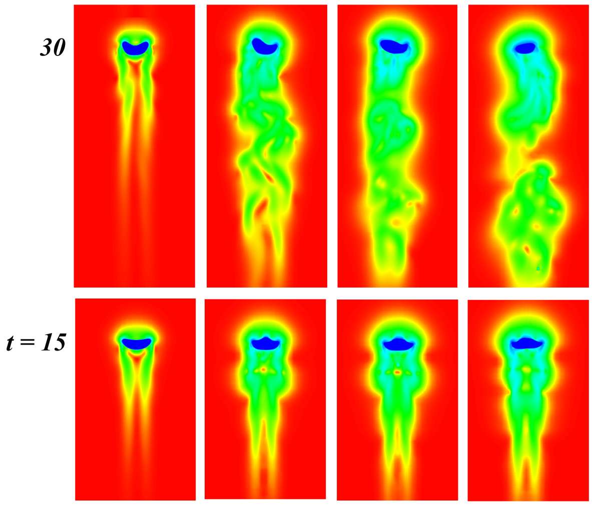

(c) *x*-*y* plane

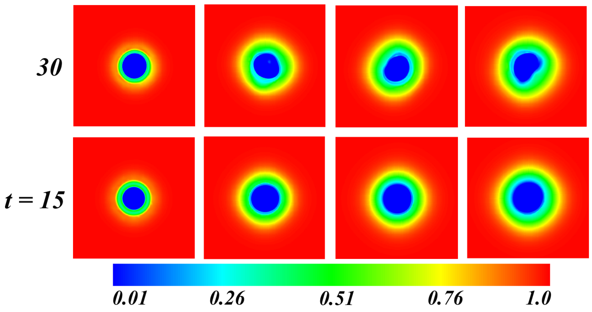

Figure 5.33: Viscosity contours in (a) *x*-*z*, (b) *y*-*z* and (c) *x*-*y* planes passing through the center of gravity of the bubble at $t = 15$ and $t = 30$ for different values of λ (left to right: $\lambda = 2$, 6, 8 and 10). The rest of the parameters are the same as those of Fig. 5.32.

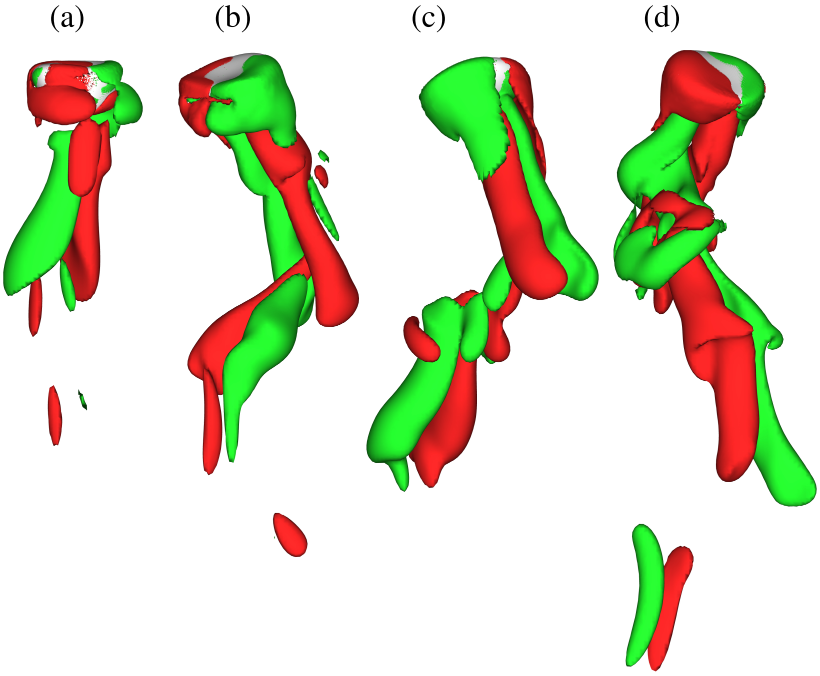

Figure 5.34: Iso-surfaces of the vorticity component in the z direction ($\omega_z = \pm 0.5$) at $t = 40$. From left to right: $\lambda = 2$, 6, 8 and 10. The rest of the parameters are the same as those of Fig. 5.32. The viscosity of the shear thinning fluid decreases from left to right.

near the upper part of the computational domain (at $t > 60$). Further decreasing the value of n, i.e increasing the shear-thinning tendency, promotes the zigzagging/spiralling motion of the air bubble. For $n = 0.3$ for this set of parameter values, it can be seen in Fig. 5.28(d) that the spiralling motion (three-dimensional) becomes vigorous. Close inspection of Fig. 5.28(b), (c) and (d) also reveals that the onset time of this zigzagging/spiralling motion decreases with the increase in the shear-thinning tendency (i.e decreasing the value of n); for $n = 0.6$ and 0.3 the oscillatory motion starts at $t \approx 50$ and $t \approx 35$, respectively.

In Fig. 5.29, the evolutions of shape of the bubble for the four values of n in Fig. 5.28 are plotted. It can be seen in Fig. 5.29(a) that the bubble attains a terminal oblate shape when it rises through a Newtonian fluid. The terminal shape of the bubble for $n = 0.8$ (Fig. 5.29(b)) is also more or less similar to that of the Newtonian case. However, for $n = 0.6$ (Fig. 5.29(c)), the bubble does not attain a terminal shape. This asymmetrical deformation of the bubble is increased for $n = 0.3$ (Fig. 5.29(d)) and the three-dimensional feature is more evident in the shapes of the bubble as well.

Fig. 5.30 shows iso-surfaces of z component of vorticity at $t = 40$ for the four values of n in Fig. 5.28. For $n = 1.0$ (Fig. 5.30 (a)), it is observed that the vorticity is confined to the interfacial region of the bubble. The size of vortical region increases for $n = 0.8$ (Fig. 5.30 (b)), with two distinguished counter-rotating patches of vorticity in the wake of the bubble, whose strength increases with increasing the shear-thinning tendency. For $n \leq 0.6$ (Fig. 5.30(c) and (d)), these vorticity patches interact to start the vortex shedding, when the bubble moves in a spiralling path.

In order to understand further the effect of shear-thinning tendency on the spiralling motion of the bubble, the cross-sectional views of viscosity contours in the x-z (Fig. 5.31(a)), y-z (Fig. 5.31(b)) and x-y (Fig. 5.31(c)) planes passing through the center of gravity of the bubble are plotted at two time instances ($t = 15$ and 30) for each view. Four values of flow index (the same as those used in Fig. 5.28) are considered for the surrounding fluid. The blue regions represent the bubble having dimensionless viscosity 0.01. In case of surrounding Newtonian fluid ($n = 1$), it can be seen in the left panels of Fig. 5.31(a), (b) and (c) that there is no viscosity variation in the surrounding fluid and the bubble reaches an oblate shape. As the bubble rises in the shear-thinning fluid, the shear rate near the bubble increases, which in turn decreases the viscosity of the surrounding fluid near the bubble. For $n = 0.8$, long tails of this less viscous region can also be seen in the second panel of Fig. 5.31(a) and (b). Close inspection of this figure also reveals that decreasing n (i.e. increasing shear-thinning tendency) increases the length of the tail of the less viscous fluid surrounding the bubble. For $n \leq 0.6$ (in the third and fourth panels of Fig. 5.31(a) and (b)), this tail of less viscous region becomes wavy, indicating the presence of an unsteady wake flow behind the bubble. This in turn promotes the spiralling/zigzagging motion of the bubble. The bubble for $n \leq 0.6$ is also non-circular in the top view, i.e x-y plane (see Fig. 5.31(c); two panels in the right).

Effect of λ

The effect of increasing the dimensionless inelastic time constant λ is discussed below. In Fig. 5.32, the trajectories of the bubble for $\lambda = 2$, 8 and 10 are plotted. The rest of the parameter values are the same as Fig. 5.23(b), where the trajectory of the bubble for $\lambda = 6$ is shown. It can be seen that increasing the value of λ increases the three-dimensional motion of the bubble. This can be visualised by comparing the extent of zigzagging/spiralling motion of the bubble. This effect is also associated with the increase in asymmetrical shape deformation of the bubble (not shown) with the increase in the value of λ. The viscosity contours in the x-z, y-z and x-y planes passing through the center of gravity of the bubble at $t = 15$ and $t = 30$ are plotted in Fig. 5.33(a), (b) and (c), respectively, for different values of λ. It can be seen that the viscosity contours in the wake region of the bubble also become unsteady; this unsteadiness increases with increasing λ. This promotes the vortex shedding in the wake region of the bubble, as shown in Fig. 5.34, which in turn increases the zigzagging/spiralling motion of the bubble.

In the next section, we present the experiment conducted to visualise the dynamics of a rising bubble in CMC solutions in deionised water, which can be modelled as Carreau-Yasuda shear-thinning fluids.

5.3.2 Experimental study

Experimental set-up and methodology

The details of the experimental set-up is discussed in Chapter 2. The objective of the present experiment is to study the behaviour of an air bubble rising in a non-Newtonian shear-thinning fluid. For this purpose, solutions of carboxymethyl cellulose (CMC) with deionised water, which exhibit shear-thinning nature, are used. The shear-thinning tendency of these solutions varies as a function of the concentration of CMC. The different concentrations of CMC solutions are prepared by thoroughly mixing a quantified amount of CMC powder in 100 *ml* of ultra pure Milli-pore water with a resistivity of 18.2MΩ. The values of viscosity of CMC solutions of different concentrations are measured using a rheometer (MCR 301 by Anton Paar) equipped with a cone-and-plate geometry (diameter: 40 mm, angle: 0.034 radian) at a controlled temperature of 303 K.

The variations of viscosity of five different CMC solutions as a function of shear rate are plotted in Fig. 5.35 in log-log scales. It can be seen that increasing the concentration of CMC increases the viscosity of the solutions at zero shear rate from $10^{-3} Pas$ (for pure water; data not shown) to $2.0 Pas$ (for solution of $0.8 g$ of CMC is $100 ml$ of water). The simplified Carreau-Yasuda rheological model (Eq (5.9)) is fitted for each set of data, which are shown by dashed lines. It can be seen that all the solutions exhibit shear thinning behaviour. The parameters associated with the Carreau-Yasuda rheological model for the five solutions are listed in Table 5.2. The rising bubble experiments are conducted for all these solutions; however, we found that as CMC concentration increases (> 0.1 g of CMC in 100 *ml* of water), the solution becomes darker, which makes the visualisation increasingly difficult. So we present here, the results for a typical solution of CMC (0.1 g of CMC in 100 *ml* of water). For the Newtonian fluid, a mixture of 70% glycerol and pure water, whose viscosity is 0.05 Pas, is used. The experiments are repeated to ensure consistency over multiple runs.

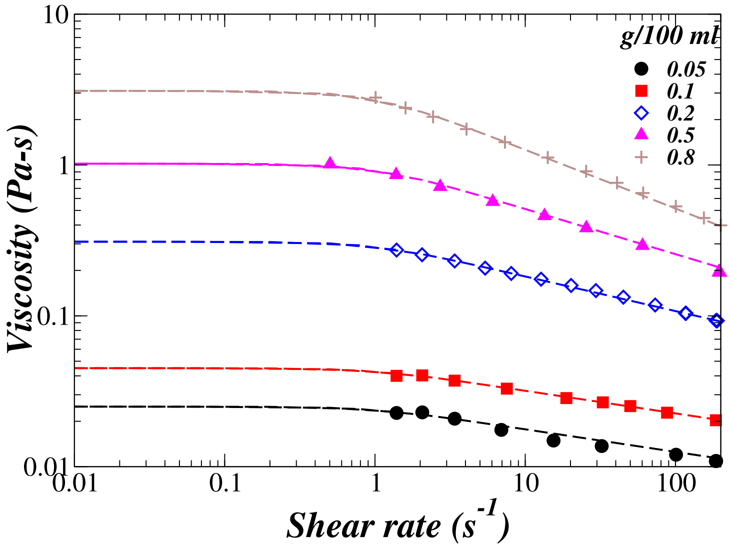

Figure 5.35: Variation of viscosity with shear rate for different concentrations of carboxymethyl cellulose (CMC) in water. The best fit curves (based on Eq. (5.9)) correspond to (λ = 0.3 s, n = 0.85, μ_0 = 0.02 Pas), (λ = 0.3 s, n = 0.85, μ_0 = 0.04 Pas), (λ = 0.3 s, n = 0.75, μ_0 = 0.25 Pas), (λ = 0.3 s, n = 0.68, μ_0 = 0.75 Pas) and (λ = 0.3 s, n = 0.6, μ_0 = 2.0 Pas) for solutions of 0.05 g, 0.1 g, 0.2 g, 0.5 g and 0.8 g of CMC in 100 ml of water.

Table 5.2: Parameters obtained by fitting Carreau-Yasuda model for the data of five different CMC solutions.

CMC (g/100 ml)	μ_0 (Pas)	λ (s)	n
0.05	0.02	0.3	0.85
0.1	0.04	0.3	0.85
0.2	0.25	0.3	0.75
0.5	0.75	0.3	0.68
0.8	2.0	0.3	0.6

Experimental results and comparison with numerical simulations

As discussed in Section 5.3.1, an air bubble in the boundary of regions I and III travels in a straight path in a Newtonian fluid, but undergoes zigzagging/spiralling motion in a shear-thinning fluid. In order to investigate this behaviour experimentally, we present the dynamics of a rising air bubble in solution of glycerol-water (Newtonian) and solution of 0.1g of CMC/100 ml of water in Figs. 5.36 and 5.37, respectively. The corresponding numerical simulation results are also plotted along with the shapes of the bubble obtained from our experiment. It can be seen in Fig. 5.36 that for Newtonian fluid, an air bubble of radius 4.6 mm moves along the axis of symmetry of the tank and becomes steady oblate shaped bubble at t > 10. The temporal evolution of bubble shapes obtained from the numerical simulation match well with those of the experiment.

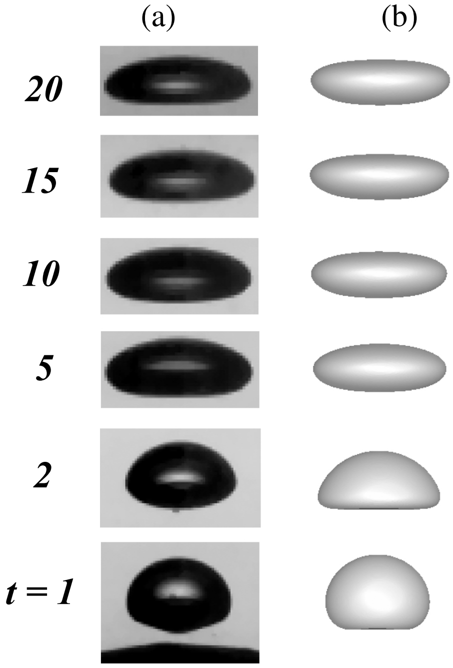

Figure 5.36: Temporal evolution of the shapes of the bubble rising in a Newtonian fluid ($\lambda = 1$ and $n = 1$) for $Ga = 24.4$ and $Eo = 2.84$ obtained from (a) experiment and (b) numerical simulation. The radius of this bubble is 4.6 *mm*.

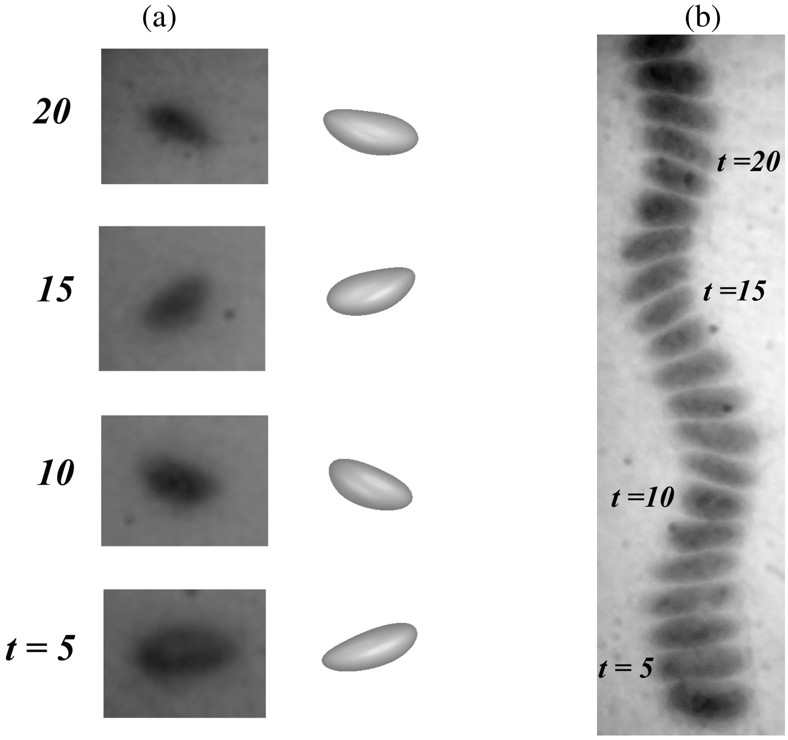

Figure 5.37: (a) Temporal evolution of the shape of the bubble obtained from experiment (left column) and numerical simulation (right column). (b) Experimentally obtained trajectory of the air bubble rising in a shear-thinning fluid (solution of 0.1 *g* of CMC in 100 *ml* of water). The values of *Ga* and *Eo* correspond to this fluid are $Ga = 24.4$ and $Eo = 2.84$, respectively. The radius of this bubble is 4.6 *mm*.

The temporal evolutions of shape and trajectory of the bubble (of radius 4.6 *mm*) in a shear-thinning fluid (0.1*g* of CMC in 100 *ml* of pure water) are shown in Fig. 5.37(a) and (b), respectively. It can be seen that the air bubble deforms into asymmetrical shapes and rises in a zigzagging path. As the CMC solution is translucent, the images obtained from the experiment are blurred. The corresponding numerical simulation results are shown in the right column of Fig. 5.37(a). The asymmetrical deformation of the bubble observed in the experiment can also be clearly seen in the numerical simulation. These experiments also confirm that for the parameter values considered, a bubble exhibits a zigzagging path in case of a shear-thinning fluid, whereas, for a Newtonian fluid, with the same set of parameter values, it rises in a straight path.

5.3.3 Concluding remarks

The dynamics of a rising air bubble in a shear-thinning non-Newtonian fluid (modelled using the Carreau-Yasuda model) has been studied by conducting direct numerical simulations and experiments. We focus on the parameter range in which the rising dynamics is three-dimensional in nature. In order to demonstrate the three-dimensional dynamics of a rising bubble in shear-thinning fluids, two sets of Ga and Eo are chosen, which lie in region I (axisymmetric) and region II (skirted) of the phase diagram obtained by Tripathi *et al.* (2015*a*) for a Newtonian fluid. For $Ga = 30$ and $Eo = 1$ (first set), it is observed that at early times the air bubble rises in a straight path and later undergoes a spiralling path. Asymmetrical shape deformation and vortex shedding are observed during the wobbling (zigzagging/spiralling) motion. The mechanism of this three-dimensional behaviour is investigated by inspecting the vertical vorticity component and viscosity. It is found that vortex shedding in the wake region, asymmetrical shape deformation and path instability are interconnected. For $Ga = 30$ and $Eo = 25$ (second set), the air bubble rising in a shear-thinning fluid undergoes peripheral break-up. In contrast, the bubble forms skirt while rising in a Newtonian fluid. We verify that the three-dimensional behaviours observed in this study are the consequence of shear-thinning nature of the surrounding medium, and not just due to the reduction of viscosity of the Newtonian fluid. The effects of the variation of flow index (n) and inelastic time constant (λ) are also investigated. It is found that increasing the shear-thinning tendency (decreasing the value of n) and increasing λ promote the three-dimensional behaviour. In our experiments, the shapes of the air bubble rising in deionised water and CMC solutions are recorded using a high-speed camera. The shapes and trajectories of the bubbles obtained from the experiments are qualitatively in good agreement with those obtained from the numerical simulations.

CHAPTER 6

Summary and potential future studies

6.1 Summary

The dynamics of a gas bubble rising in a liquid is observed in many natural phenomena, and also in industrial applications. Due to its practical relevance, this has been studied from many centuries and it continues to be a problem of great interest even today. The main objectives of the thesis are to investigate some novel problems on bubble rising in viscosity varying systems. In several situations one could observed viscosity stratified media. Two of them are considered in this work. (a) When viscosity stratification is inherently present in the surrounding medium (say for simplicity, viscosity of the outer fluid is increasing linearly with height). (b) When the outer fluid is a non-Newtonian fluid, wherein the surrounding fluid viscosity varies due to the shear caused by the motion of the bubble. Three-dimensional numerical simulations and experiments are performed to study these flows. The computational and experimental approaches used in this study are discussed in Chapter 2. The validation of the present numerical solver is also performed in the same chapter. In order to compare the bubble behaviour in a medium with varying viscosity with that observed in a constant viscosity medium (standard system), the dynamics of a rising bubble in a standard air-water system is also investigated.

First a standard system (air-water system) is considered. The dynamics of an air bubble rising in a Newtonian quiescent liquid is experimentally investigated in Chapter 3. A phase plot in the Galilei and Eötvös numbers plane, which separates distinct regimes in terms of bubble behaviour is generated. This is similar to the one numerically obtained by Tripathi *et al.* (2015*a*). Direct numerical simulations are also conducted and the behaviour of the bubble in these regimes is studied. The similarities and differences between the experimental and numerical results are discussed. The present work reveals that apart from Reynolds and Eötvös numbers, which were thought to be the only important governing parameters for rising bubbles in air-liquid systems, our results show that the actual density and viscosity ratios are also required to describe the bubble dynamics, especially in the parameter space close to the region boundaries in the phase-plot. To the best of our knowledge, none of the previous studies have shown an experimentally obtained phase plot for such a large range of Galilei and Eötvös numbers.

In chapter 4, the above study is extended to considered the interaction of two bubbles while rising side-by-side in a Newtonian fluid. Two spherical objects rising through a heavier fluid in the Stokes flow regime would maintain their spacing. In particular, if the two objects are initially in the same horizontal plane, they would rise in straight vertical paths and the line separating them would be horizontal and of constant length. In this chapter, we ask a fundamental question, i.e. how two identical inertial bubbles rising under gravity would respond to each other. Three-dimensional numerical simulations are conducted to study this problem. This study reveals the destabilizing nature of the interaction between the wakes of the bubbles, which causes them to rise in an oscillatory path. Such three dimensionality sets in earlier in time than for a single bubble and also at a lower inertia. The interaction leads to a mirror symmetry in the trajectories of the two bubbles, which persists for some time even in the high inertia regime where each path is chaotic. The effect of the inertia and initial separation on the mirror symmetry of the path, the vortex shedding pattern and the attraction/repulsion between the bubbles are examined. The bubble rise has been interestingly observed to be symmetrical about the plane perpendicular to the separation vector for all separation distances considered in the present study.

Next in Chapter 5, the rise dynamics of an air bubble in viscosity varying media is considered. It can be seen in Chapter 1 that in spite of the large number of studies carried out on bubbles and drops, very few studies have examined the influence of viscosity stratification on bubble rise dynamics. In Section 5.1, first an inherently viscosity-stratified surrounding fluid is considered. By conducting time-dependent axisymmetric simulations, a library of bubble shapes in the Galilei and the Eötvös numbers plane is presented, which demonstrates some counter-intuitive phenomena for certain range of parameters due to the presence of viscosity stratification in the surrounding fluid. It is found that in a linearly increasing viscosity medium, for certain values of parameters, bubble undergoes large deformation by forming an elongated skirt, while the skirt tends to physically separate the wake region from the rest of the surrounding fluid. This peculiar dynamics is attributed to the migration of less viscous fluid that is carried in the wake of the bubble as it rises, and thereby creating an increasingly larger viscosity contrast between the fluid occupied in the wake region and the surrounding fluid, unlike that observed in a constant viscosity medium. We also found that for lower values of Eo and Ga, although the bubble moves slowly in case of the linearly increasing viscosity medium, the shapes look very similar to those observed in a constant viscosity medium. In future, it will be interesting to investigate this phenomenon in three-dimensions and by conducting experiments.

Then the dynamics of an air bubble inside a shear thinning/thickening fluid is studied in both axisymmetric and three-dimensional regimes. The non-Newtonian fluid is modelled using the Carreau-Yasuda model (Zhang *et al.*, 2010). In the axisymmetric regime (see Section 5.2), we focus on a bubble in the low Ga and low Eo region. A parametric study is conducted by varying the shear-thinning/thickening tendency of the surrounding fluid for different Galilei and Eötvös numbers. As compared to a Newtonian fluid, it is found that increasing the shear thinning tendency increases the rise velocity, and reduces the deformations of the bubble. The deformation of the bubble is enhanced for higher Ga and low Eo. This work also reveals the importance of studying the rising bubble in the other regimes, i.e high Ga and moderate to high Eo, where the dynamics is three-dimensional. This constitute the subject of discussion in the next section.

The dynamics of a rising bubble in a Carreau-Yasuda shear-thinning fluid is studied in Section 5.3 via three-dimensional simulations and experiments using CMC (carboxymethyl cellulose) solutions. For the parameter values considered, an air bubble exhibits three-dimensional behaviour, i.e. path instabilities (zigzagging/spiralling motion) and topological changes while rising in shear-thinning fluids (CMC solutions). For the same set of parameters, a bubble maintains azimuthal symmetry and rises in a straight path while rising in a Newtonian surrounding fluid. The mechanism of this three-dimensional behaviour is investigated by plotting the vorticity and viscosity contours. For $Ga = 30$ and $Eo = 1$ (first set), it is observed that at early times the air bubble rises in a straight path and later undergoes a spiralling path. Asymmetrical shape deformation and vortex shedding are observed during the wobbling (zigzagging/spiralling) motion. The mechanism of this three-dimensional behaviour is investigated by inspecting the vertical vorticity component and viscosity. It is found that vortex shedding in the wake region, asymmetrical shape deformation and path instability are interconnected. For $Ga = 30$ and $Eo = 25$ (second set), an air bubble rising in a shear-thinning fluid undergoes peripheral breakup. In contrast, the bubble forms skirt while rising in a Newtonian fluid. We verify that the three-dimensional behaviours observed in this study are the consequence of shear-thinning nature of the surrounding medium, and not just due to the reduction of viscosity of the Newtonian fluid. The effects of the variation of flow index (n) and inelastic time constant (λ) are also investigated. It is found that increasing the shear-thinning tendency (decreasing the value of n) and increasing λ promote the three-dimensional behaviour. In our experiments, the shapes of an air bubble rising in deionised water and CMC solutions are recorded using a high-speed camera. The shapes and trajectories of the bubbles obtained from the experiments are qualitatively in good agreement with those obtained from the numerical simulations.

6.2 Future scope

The present study **arises** further questions and new areas to be investigated in future. This includes

- What happens in case of drops falling in an gaseous medium or in another liquid media?
- What happens when we change the initial condition by changing the initial shape of bubbles/drops from spherical to complex shapes, such as oblate, prolate and even more complex shapes which are seen in experiments?
- How the presence of temperature gradient (Marangoni convection) influences the dynamics of bubbles?
- What happens when the bubble rises in fluids with other rheologies, such as viscoelastic, viscopleastic, thixotropic nature?

As discussed in the Chapter 1, a blob of fluid of density ρ_i moving in a surrounding medium of density ρ_o is called a bubble if $\rho_r(\equiv \rho_i/\rho_o) < 1$ or a drop if $\rho_r > 1$. In gas-liquid systems, bubbles in general behave differently from drops and the mechanism behind the differences were investigated by Tripathi *et al.* (2014). It is well known that as a result of path instability, an initially spherical air bubble rising in a liquid ($\rho_r << 1$) can either zigzag or spiral for high inertia and high surface tension (Cano-Lozano *et al.*, 2016*a*; Saffman, 1956; Tripathi *et al.*, 2015*a*). It undergoes an unsteady shape deformation resulting in vortex shedding behind the bubble during this wobbling motion. In contrast, a solid sphere or an initially spherical liquid drop in air ($\rho_r >> 1$) falls in a straight path (Vries, 2001). For a falling leaf or flat/cylindrical solid objects (i.e. non-spherical) in gas/liquid, oscillatory motion is observed due to the associated aerodynamics/hydrodynamics. A question that arises then is, can we observe path and/or shape instabilities by making the initial drop shape nonspherical in an air-liquid system. It would be interesting to study if a similar phenomenon occurs for a nonspherical liquid drop falling in air.

In liquid-liquid systems (with $\rho_r \leq 2.2$), by releasing spherical drops of organic liquids, Edge & Grant (1971) experimentally found that a small liquid drop falls in a straight path, but a bigger drop falls in a zig-zag path (i.e., wobbling motion) in water under the action of gravity. They observed a thread-like wake for small drops, but vortex sheet for large drops falling in zigzag paths. They also observed shape oscillations (oblate-prolate deformation) in case of zigzagging drops. Later, considering liquid-liquid systems (for $\rho_r \approx 1$), Koh & Leal (1989, 1990) investigated the dynamics of an initially nonspherical bubble rising in a quiescent liquid of slightly higher density by conducting numerical simulations and experiments at low Reynolds numbers ($Re < 0.01$). They found that a bubble with a small degree of nonsphericity, comes back to a spherical shape, whereas for a bubble with a large degree of nonsphericity, the deformation continues to increase with time.

Another PhD student Meenu Agrawal is extending the present work to investigate the effect of nonspherical shape liquid droplets falling in air or another lighter liquid. She is also planning to conduct Particle Image Velocimetry (PIV) to understand the flow dynamics experimentally. I have recently collaborated with Meenu Agrawal in one of her PhD work. We have attempted to answer the following questions: (i) Can one observe oscillatory motion in case of a falling liquid drop in air ($\rho_r >> 1$) by changing its initial shape to a nonspherical one? (ii) For situation (i), where inertia becomes important, what effect does it have on the droplet dynamics? (iii) The presence of inertia may result in vortex shedding. What is the role of vortex shedding in this case and how different is it from that observed in case of a rising bubble? To answer these questions, three-dimensional numerical simulations are conducted to investigate the hydrodynamics of an initially nonspherical liquid droplet falling in air ($\rho_r \approx 1000$), and the effects of initial deformation (degree of obliquity) and inertia are investigated. See our article Agrawal *et al.*, PRE, 2017 for more detail.

The knowledge of the present study is also very useful in investigating raindrops. However, one has to include many complex phenomena, such as phase change, coalescence and break-up in to the model. These phenomena affect the shape and size distributions of raindrops, which in turn influence the modelling of rainfall. As these phenomena depend on local conditions, in order to make an accurate prediction, one has to study raindrops and associated dynamics for a given atmospheric condition.

In all the situations discussed above, the presence of temperature provides another dimension to the study. Marangoni stresses due to the variation in surface tension by virtue of the presence of temperature and concentration gradients at the interface separating two immiscible fluids play a vital role in many technological applications. A characteristic problem of this nature is the thermocapillary migration of drops and bubbles. The current work can be extended to include the Marangoni convection due to temperature/surfactant gradients. Another PhD student in our group, Mounika Balla is working on these aspects.

A variety of situations can also be considered by varying the rheological properties of the surrounding medium. In the present thesis, only a shear-thinning fluid is considered. It will be interesting to investigate the dynamics of an air bubble rising in other class of non-Newtonian fluids, such as viscoplastic, viscoelastic and thixotropic fluids.

Bibliography

Allen, H. S. 1900 Xxxi. the motion of a sphere in a viscous fluid. *The London, Edinburgh, and Dublin Philosophical Magazine and Journal of Science* **50**, 323–338.

Astarita, G. & Apuzzo, G. 1965 Motion of gas bubbles in non-newtonian liquids. *AIChE J.* **11** (5), 815820.

Balasubramaniam, R. 1998 Thermocapillary and buoyant bubble motion with variable viscosity. *Int. J. Multiphase Flow* **24** (4), 679–683.

Balasubramaniam, R. & Subramaniam, R. S. 1996 Thermocapillary bubble migrationthermal boundary layers for large marangoni numbers. *Int. J. Multiphase Flow* **22** (3), 593–612.

Balasubramaniam, R. & Subramanian, R. S. 2000 The migration of a drop in a uniform temperature gradient at large marangoni numbers. *Phys. Fluids* **12** (4), 733–743.

Baltussen, M., Kuipers, J. & Deen, N. 2014 A critical comparison of surface tension models for the volume of fluid method. *Chem. Eng. Sci.* **109**, 65–74.

Beal, C. *et al.* 1946 The viscosity of air, water, natural gas, crude oil and its associated gases at oil field temperatures and pressures. *Transactions of the AIME* **165** (01), 94–115.

Bhaga, D. & Weber, M. E. 1981 Bubbles in viscous liquids: shapes, wakes and velocities. *J. Fluid Mech.* **105**, 61–85.

Bird, R. B., Armstrong, R. C. & Hassager, O. 1987 *Dynamics of Polymeric Liquids*. 2nd edition: John Wiley and Sons.

Bonhomme, R., Magnaudet, J., Duval, F. & Piar, B. 2012 Inertial dynamics of air bubbles crossing a horizontal fluid–fluid interface. *J. Fluid Mech.* **707**, 405–443.

Bonometti, T. & Magnaudet, J. 2006 Transition from spherical cap to toroidal bubbles. *Phys. Fluids* **18**, 1–12.

Bonometti, T. & Magnaudet, J. 2007 An interface-capturing method for incompressible two-phase flows. validation and application to bubble dynamics. *Int. J. Multiphase Flow* **33**, 109–133.

Bonometti, T., Magnaudet, J. & Gardin, P. 2007 On the dispersion of solid particles in a liquid agitated by a bubble swarm. *Metallurgical and Materials Transactions B* **38**, 739–750.

Brackbill, J., Kothe, D. B. & Zemach, C. 1992 A continuum method for modeling surface tension. *J. Comput. Phys.* **100**, 335–354.

Bunner, B. & Tryggvason, G. 1999 Direct numerical simulations of three-dimensional bubbly flows. *Phys. Fluids* **11**, 1967–1969.

Cano-Lozano, J., Bohorquez, P. & Mart´inez-Bazán, C. 2013 Wake instability of a fixed axisymmetric bubble of realistic shape. *Int. J. Multiphase Flow* **51**, 11–21.

Cano-Lozano, J. C., Mart´inez-Bazán, C., Magnaudet, J. & Tchoufag, J. 2016*a* Paths and wakes of deformable nearly spheroidal rising bubbles close to the transition to path instability. *Phys. Rev. Fluids* **1**, 053604.

Cano-Lozano, J. C., Martinez-Bazan, C., Magnaudet, J. & Tchoufag, J. 2016*b* Paths and wakes of deformable nearly spheroidal rising bubbles close to the transition to path instability **1** (5), 053604.

Chen, R. H., Tian, W. X., Su, G. H., Qiu, S. Z., Y.Ishiwatari & Oka, Y. 2011 Numerical investigation on coalescence of bubble pairs rising in a stagnant liquid. *Chem. Eng. Sci.* **66**, 5055–5063.

Chhabra, R. 2006 *Bubbles, drops, and particles in non-Newtonian fluids*. CRC press.

Chhabra, R. S. 1993 *Bubbles, drops and particles in non-Newtonian fluids*. Boca Raton: CRC Press.

Clift, R., Grace, J. & Weber, M. 1978 *Bubbles, Drops and Particles*. New York: Dover Publications, Inc.

Collins, R. 1965 Structure and behaviours of wakes behind two-dimensional air bubbles in water. *Chem. Eng. Sci.* **20**, 851–853.

Crespo, A., Migoya, E. & Manuel, F. 1998 Thermocapillary migration of bubbles at large reynolds numbers. *Int. J. Multiphase Flow* **24** (4), 685–692.

Crow, S. C. 1970 Stability theory for a pair of trailing vortices. *AIAA J.* **8**, 2172–2179.

Dijkhuizen, W., van. Sint Annaland, M. & Kuipers, J. 2010 Numerical and experimental investigation of the lift force on single bubbles. *Chem. Eng. Sci.* **65**, 1274–1287.

Dimakopoulos, Y., Pavlidis, M. & Tsamopoulos, J. 2013 Steady bubble rise in HerschelBulkley fluids and comparison of predictions via the augmented lagrangian method with those via the papanastasiou model. *J. Non-Newtonian Fluid Mech.* **200**, 34–51.

Duineveld, P. 1998 Bouncing and coalescence of bubble pair rising at high reynolds number in pure water or aqueous surfactant solutions. *Appl. Sci. Res.* **58**, 409–439.

Duineveld, P. C. 1995 The rise velocity and shape of bubbles in pure water at high reynolds number. *J. Fluid Mech.* **292**, 325–332.

Edge, R. M. & Grant, C. D. 1971 The terminal velocity and frequency of oscillation of drops in pure systems. *Chem. Eng. Sci.* **26**, 1001–1012.

Frigaard, I. A. & Nouar, C. 2005 On the usage of viscosity regularisation methods for visco-plastic fluid flow computation. *J. Non-Newtonian Fluid Mech.* **127**, 1–26.

Gal-Or, B., Klinzing, G. E. & Tavlarides, L. L. 1969 Bubble and drop phenomena. *Ind. Eng. Chem.* **61** (2), 21–34.

Ghannam, M. T. & Esmail, M. N. 1997 Rheological properties of carboxymethyl cellulose. *Journal of applied polymer science* **64** (2), 289–301.

Govindarajan, R. & Sahu, K. C. 2014 Instabilities in viscosity-stratified flows. *Ann. Rev. Fluid Mech.* **46**, 331–353.

Haberman, W. L. & Morton, R. K. 1953 An experimental investigation of the drag and shape of air bubbles rising in various liquids. *Tech. Rep.*. DTIC Document.

Hadamard, J. 1911 Mouvement permanent lent dune sphere liquide et visqueuse dans un liquide visqueux. *CR Acad. Sci* **152**, 1735–1738.

Hallez, Y. & Legendre, D. 2011 Interaction between two spherical bubbles rising in a viscous liquid. *Journal of Fluid Mechanics* **673**, 406–431.

Hassager, O. 1979 Negative wake behind bubbles in non-newtonian liquids. *Nature* **279**, 402–403.

Hua, J., Stene, J. F. & Lin, P. 2008 Numerical simulation of 3D bubbles rising in viscous liquids using a front tracking method. *J. Comput. Phys.* **227**, 3358–3382.

Islam, M. T., Ganesan, P. & J., C. 2015 A pair of bubbles rising dynamics in a xanthan gum solution: a cfd study. *RSC Adv.* **5**, 7819–7831.

Kemiha, M., Olmos, E., Fei, W., Poncin, S. & Li, H. Z. 1991 Passage of a gas bubble through a liquid-liquid interface. *Ind. Eng. Chem. Res.* **46**, 6099–6104.

Kilonzo, P. M. & Margaritis, A. 2004 The effects of non-newtonian fer- mentation broth viscosity and small bubble segregation on oxygen mass transfer in gas-lift bioreactors: A critical review. *Biochem. Eng. J.* **17**, 27–40.

Kishore, N., Chhabra, R. P. & Eswaran, V. 2007 Drag on a single fluid sphere translating in power-law liquids at moderate Reynolds numbers. *Chem. Eng. Sci.* **62**, 2422–2434.

Koh, C. J. & Leal, L. G. 1989 The stability of drop shapes for translation at zero reynolds number through a quiescent fluid. *Phys. Fluids A* **1(8)**, 1309–1313.

Koh, C. J. & Leal, L. G. 1990 An experimental investigation on the stability of viscous drops translating through a quiescent fluid. *Phys. Fluids A* **2(12)**, 2103–2109.

Kok, J. B. W. 1993*a* Dynamics of a pair of gas bubbles moving through liquid. part i. theory. *Eur. J. Mech. B/Fluids* **12**, 515–540.

KOK, J. B. W. 1993*b* Dynamics of a pair of gas bubbles moving through liquid. part ii. experiment. *Eur. J. Mech. B/Fluids* **12**, 541–560.

KULKARNI, A. A. & JOSHI, J. B. 2005 Bubble formation and bubble rise velocity in gas-liquid system: A review. *Ind. Eng. Chem. Res.* **44**, 5874–5931.

LANDEL, J. R., COSSU, C. & CAULFIELD, C. P. 2008 Spherical cap bubbles with a toroidal bubbly wake. *Phys. Fluids* **20**, 122201.

LEAL, L. G. 1992 *Laminar Flow and Convective Transport Processes*. Stoneham, MA: Butterworth and Heinemann.

LEGENDRE, D., MAGNAUDET, J. & MOUGIN, G. 2003 Hydrodynamic interactions between two spherical bubbles rising side by side in a viscous liquid. *J. Fluid Mech.* **497**, 133–166.

LUNDE, K. & PERKINS, R. J. 1997 Observations on wakes behind spheroidal bubbles and particles. *Tech. Rep.*. FEDSM97-3530, ASME-FED Summer Meeting, Vancouver, Canada.

MAGNAUDET, J. & MOUGIN, G. 2007 Wake instability of a fixed spheroidal bubble. *J. Fluid Mech.* **572**, 311–337.

MANGA, M. & STONE, H. A. 1995 Low reynolds number motion of bubbles, drops and rigid spheres through fluid–fluid interfaces. *J. Fluid Mech.* **287**, 279–298.

MERRITT, R. M., MORTON, D. S. & SUBRAMANIAN, R. S. 1993 Flow structures in bubble migration under the combined action of buoyancy and thermocapillarity. *J. Colloid Interf. Sci.* **155** (1), 200–209.

MOUGIN, G. & MAGNAUDET, J. 2002 Path instability of a rising bubble. *Phys. Rev. Lett.* **88**, 014502.

OHTA, M., AKAMA, Y., YOSHIDA, Y. & SUSSMAN, M. 2014 Influence of the viscosity ratio on drop dynamics and breakup for a drop rising in an immiscible low-viscosity liquid. *J. Fluid Mech.* **752**, 383–409.

OHTA, M., IMURA, T., OSHIDA, Y. & SUSSMAN, M. 2005*a* A computational study of the effect of initial bubble conditions on the motion of a gas bubble rising in viscous liquids. *Int. J. Multiphase Flow* **31**, 223–237.

OHTA, M., IWASAKI, E., OBATA, E. & YOSHIDA, Y. 2003 A numerical study of the motion of a spherical drop rising in shear-thinning fluid systems. *J. Non-Newtonian Fluid Mech.* **116**, 95–111.

OHTA, M., IWASAKI, E., OBATA, E. & YOSHIDA, Y. 2005*b* Dynamic processes in a deformed drop rising through shear-thinning fluids. *J. Non-Newtonian Fluid Mech.* **132**, 100–107.

OHTA, M., KIMURA, S., FURUKAWA, T., YOSHIDA, Y. & SUSSMAN, M. 2012 Numerical simulations of a bubble rising through a shear-thickening fluid. *Journal of Chemical Engineering of Japan* **45** (9), 713–720.

OHTA, M. & SUSSMAN, M. 2012 The buoyancy-driven motion of a single skirted bubble or drop rising through a viscous liquid. *Phys. Fluids* **24**, 112101.

OHTA, M., YOSHIDA, Y. & SUSSMAN, M. 2009 A computational study of the dynamic motion of a bubble rising in carreau model fluids. *Fluid dynamics research* **42** (2), 025501.

POPINET, S. 2003 Gerris: a tree-based adaptive solver for the incompressible euler equations in complex geometries. *J. Comput. Phys.* **190**, 572–600.

POPINET, S. 2009 An accurate adaptive solver for surface-tension-driven interfacial flows. *J. Comput. Phys.* **228**, 5838–5866.

PROSPERETTI, A. 2004 Bubbles. *Phys. Fluids* **16 (6)**, 1852–1865.

RYBZYNSKI, W. 1911 ber die fortschreitende bewegung einer flssigen kugel in einem zhen medium. *Bull. Acad. Sci.* .

SAFFMAN, P. G. 1956 On the rise of small air bubbles in water. *J. Fluid Mech.* **1**, 249–275.

SANADA, T., SATO, A., SHIROTA, M. & WATANABLE, M. 2009 Motion and coalescence of a pair of bubbles rising side by side. *Chem. Eng. Sci.* **64**, 2659–2671.

SANADA, T., SUGIHARA, K., SHIROTA, M. & WATANABE, M. 2008 Motion and drag of a single bubble in super-purified water. *Fluid Dyn. Res.* **40**, 534–545.

SHAH, Y. T., KELKAR, B. G., GODBOLE, S. P. & DECKWER, W. D. 1982 Design parameters estimation for bubble column reactors. *AICHE J.* **28**, 353–379.

SHU, S. & YANG, N. 2013 Direct numerical simulation of bubble dynamics using phase-field model and lattice boltzmann method. *Ind. Eng. Chem. Res.* **52**, 11391–11403.

SUBRAMANIAN, R. S. 1981 Slow migration of a gas bubble in a thermal gradient. *AIChE J.* **27** (4), 646654.

SUBRAMANIAN, R. S. 1983 Thermocapillary migration of bubbles and droplets. *Adv. Space Res.* **3** (5), 145–153.

SUBRAMANIAN, R. S. 1992 *Transport Processes in Drops, Bubbles and Particles*. London: Hemisphere.

SUBRAMANIAN, R. S., BALASUBRAMANIAM, R. & WOZNIAK, G. 2002 Fluid mechanics of bubbles and drops. In *Physics of Fluids in Microgravity* (ed. R. Monti), pp. 149–177. London: Taylor and Francis.

SUSSMAN, M. & PUCKETT, E. G. 2000 A coupled level set and volume-of-fluid method for computing 3D and axisymmetric incompressible two-phase flows. *J. Comput. Phys.* **162**, 301–337.

SUSSMAN, M. & SMEREKA, P. 1997 Axisymmetric free boundary problems. *J. Fluid Mech.* **341**, 269–294.

TOMIYAMA, A., CELATA, G., HOSOKAWA, S. & YOSHIDA, S. 2002 Terminal velocity of single bubbles in surface tension force dominant regime. *Int. J. Multiphase Flow* **28**, 1497–1519.

TRIPATHI, M. K., SAHU, K. C. & GOVINDARAJAN, R. 2014 Why a falling drop does not in general behave like a rising bubble. *Sci. Rep.* **4**, 4771.

TRIPATHI, M. K., SAHU, K. C. & GOVINDARAJAN, R. 2015*a* Dynamics of an initially spherical bubble rising in quiescent liquid. *Nat. Commun.* **6**, 6268.

TRIPATHI, M. K., SAHU, K. C., KARAPETSAS, G. & MATAR, O. K. 2015*b* Bubble rise dynamics in a viscoplastic material. *J. Non-Newtonian Fluid Mech.* **222**, 217–226.

TRIPATHI, M. K., SAHU, K. C., KARAPETSAS, G., SEFIANE, K. & MATAR, O. K. 2015*c* Non-isothermal bubble rise: non-monotonic dependence of surface tension on temperature. *J. Fluid Mech.* **763**, 82–108.

TSAMOPOULOS, J., DIMAKOPOULOS, Y., CHATZIDAI, N., KARAPETSAS, G. & PAVLIDIS, M. 2008*a* Steady bubble rise and deformation in newtonian and viscoplastic fluids and conditions for bubble entrapment. *J. Fluid Mech.* **601**, 123–164.

TSAMOPOULOS, J., DIMAKOPOULOS, Y., CHATZIDAI, N., KARAPETSAS, G. & PAVLIDIS, M. 2008*b* Steady bubble rise and deformation in newtonian and viscoplastic fluids and conditions for bubble entrapment. *J. Fluid Mech.* **601**, 123–164.

URBAIN, G., BOTTINGA, Y. & RICHET, P. 1982 Viscosity of liquid silica, silicates and alumino-silicates. *Geochimica et Cosmochimica Acta* **46** (6), 1061–1072.

VELDHUIS, C., A., B. & VAN WIJNGAARDEN, L. 2008 Shape oscillations on bubbles rising in clean and in tap water. *Phys. Fluids* **20**, 040705.

VELEZ-CORDERO, J. R., DIEGO, S. AMD YUE, P., FENG, J. J. & ZENITA, R. 2011 Hydrodynamic interaction between a pair of bubbles ascending in shear-thinning inelastic fluids. *J. Non-Newtonian Fluid Mech.* **166**, 118–132.

VRIES, A. W. G. 2001 Path and wake of a rising bubble. *Tech. Rep.*. University of Twente, Netherlands (ISBN 90 365 15262).

WALTERS, J. K. & DAVIDSON, J. F. 1963 The initial motion of a gas bubble formed in an inviscid liquid. Part 2. The three-dimensional bubble and the toroidal bubble. *J. Fluid Mech.* **17**, 321–336.

YOUNG, N. O., GOLDSTEIN, J. S. & BLOCK, M. J. 1959 The motion of bubbles in a vertical temperature gradient. *J. Fluid Mech.* **6**, 350–356.

ZENIT, R. & MAGNAUDET, J. 2002 Path instability of a rising bubble. *Phys. Rev. Lett.* **88(1)**, 014502.

ZHANG, L., SUBRAMANIAN, R. S. & BALASUBRAMANIAM, R. 2001 Motion of a drop in a vertical temperature gradient at small marangoni number the critical role of inertia. *J. Fluid Mech.* **448**, 197–211.

Zhang, L., Yang, C. & Mao, L.-S. 2010 Numerical simulation of a bubble rising in a shear-thinning fluids. *J. Non-Newtonian Fluid Mech.* **165**, 555–567.